UNIVERSITÀ DEGLI STUDI FIRENZE

DOTTORATO DI RICERCA IN INGEGNERIA INDUSTRIALE
(*Indirizzo in SCIENZE ED INGEGNERIA DEI MATERIALI*)

CICLO XXIX

COORDINATORE Prof. De Lucia Maurizio

Soft ferrite magnetic nanoparticles: a new strategy to improve the performance of high frequency electronic devices

Settore Scientifico Disciplinare ING-IND/22

Dottorando
Dott. Petrecca Michele

Tutori
Prof. Caneschi Andrea

Dott. López-Ortega Alberto

Coordinatore
Prof. De Lucia Maurizio

Anni 2013/2016

© Università degli Studi di Firenze – Faculty of Engineering Via di Santa Marta, 3, 50139 Firenze, Italy

Tutti i diritti riservati. Nessuna parte del testo può essere riprodotta o trasmessa in qualsiasi forma o con qualsiasi mezzo, elettronico o meccanico, incluso le fotocopie, la trasmissione fac-simile, la registrazione, il riadattamento o l'uso di qualsiasi sistema di immagazzinamento e recupero di informazioni, senza il permesso scritto dell' editore .

All rights reserved. No part of the publication may be reproduced in any form by print, photoprint, microfilm, electronic or any other means without written permission from the publisher.

Table of contents

Chapter 1 **1**

Introduction **1**

Chapter 2 **17**

Magnetism and magnetic materials **17**

2.1 Introduction to magnetism 17

2.2 Diamagnetic materials 21

2.3 Paramagnetic materials 22

2.4 Ordered magnetic materials 24

2.4.1 Ferromagnetic materials 25

2.4.2 Antiferromagnetic and Ferrimagnetic materials 26

2.4.3 Hysteresis in ordered magnetic materials. 28

2.5 Magnetic domains 30

2.6 Magnetic properties of nanoparticles 34

2.6.1 Single domain magnetic nanoparticles 34

2.6.2 Superparamagnetism 37

2.6.3 Surface effects 39

2.6.4 The role of magnetic interactions 40

2.7 Soft magnetic materials 42

2.7.1 AC energy losses for magnetic materials. 44

2.7.2 AC electronic circuit 47

References 53

Chapter 3 **59**

Synthesis and characterization of ferrite nanoparticles **59**

3.1 Synthetic approaches to magnetic nanoparticles 59

3.2 Chemical synthesis of nanoparticles 61

3.2.1 Microemulsion synthesis 61

3.2.2 Hydrothermal synthesis 61

3.2.3 Polyol synthesis 62

3.2.4 Thermal decomposition synthesis 63

3.2.5 Co-precipitation synthesis 63

3.3 Spinel ferrites 65

3.4 Synthesis of doped iron oxide ferrite nanoparticles 70

3.4.1 Experimental procedure 71

3.4.2 Characterization of the chemical, structural and physical properties 82

3.5 Evaluation of the soft behaviour of the doped ferrite nanoparticles. 90

3.5.1 Evaluation of magnetic permeability. 90

3.6 The set-up for core loss determination 96

Chapter 4 **105**

From nanopowders to a high density product. **105**

4.1 Toroid die fabrication. 106

4.2 Optimization of the heating treatment 110

4.2.1 Improvement of the oven. 112

4.2.2 Optimization of the heating procedures. 115

4.2.3 The sintering process. 119

4.3 Moving towards industrial applications 136

Chapter 5 **141**

Conclusions and perspectives **141**

Chapter 6 **147**

Experimental Techniques **147**

6.1 Electron Microscopy Techniques. 147

6.2 X-Ray based techniques. 153

6.3 Physical Properties Measuring System (PPMS). 162

6.4 High Pressure-Field Assisted Sintering Technique (HP-FAST) 165

6.5 Dilatometer 168

Chapter 1

Introduction

The research on materials with improved and finely controlled properties has experienced a great development triggered by the huge demand of new generation high-technology devices, which has characterized the last years. In particular, the miniaturization requirement inherent to the high-tech components pushed the scientific community to achieve a progressively deeper ability in designing, synthesizing and manipulating structures at the nanoscale. Such momentum in research led to the discovery of unexpected optical, electrical, catalytic, mechanical, biological and magnetic properties, which arise from the nanostructural nature of these materials, such as size, shape or arrangements of different nano-sized materials. However, the fabrication, characterization and final application of nanomaterials remain open challenges and considerable efforts are required to explore technological procedures for innovative nanostructured materials application.

As the material size reduces to a comparable size respect to some characteristic length scale (e.g., electron mean free path, domain wall width, diffusion length, superconducting coherence length, etc.) *finite-size effects* occur strongly modifying the related physical or chemical properties with respect to the bulk counterparts and often novel phenomena are observed [1].

A relevant example of a *finite-size effect* is the dramatic increase in the fraction of the total number of atoms located at the surface, whose behaviour is strongly affected by alterations in coordination number, symmetry of the local environment and matrix interaction, [1],[2] which leads to various and complex modifications of materials properties (*surface effects)*.

Nanomaterials can be classified according to their "microscopic" dimensionality (*D*): [3]

- *Quasi-zero-dimensional* (*0D*): nanoparticles, clusters and quantum dots with none of their three dimensions larger than 100 nm (three dimensions at the nanoscale).
- *One-dimensional* (*1D*): nanowires and nanotubes with two dimensions at the nanoscale.
- *Two-dimensional* (*2D*): thin films and multilayers with only one dimension at the nanoscale.
- *Three-dimensional* (*3D*): mesoporous structures and 3D arrays of nanoparticles.

The great interest in nano-systems research can be understood both in terms of fundamental knowledge of materials properties and considering the large variety of applications in medicine and pharmacology, data storage, refrigeration, electronics, optics, ceramics and insulators industry, mechanics, sensors, catalysis, polymers industry, energy storage and production, as schematically reported in Table 1.1. [4]

Table 1.1 : Schematic classification of main applications for nanoparticles.

Area of interest	**Application Examples**
Biological	Diagnosis (contrast agents for magnetic resonance) [5]–[7] Medical therapy (drug delivery, hyperthermia) [8]–[10]
Chemical	Catalysis (fuel cells, photocatalytic devices and production of chemicals) [11]–[13]
Electronic	High performance delicate electronics [14] High performance digital displays [15], [16]
Energetic	High performance batteries (longer-lasting and higher energy density) [17] High-efficiency fuel and solar cells [18], [19]
Magnetic	High density storage media [20] Highly sensitive bio-sensing [21] Permanent magnets [22]
Mechanical	Mechanical devices with improved wear and tear resistance, lightness and strength, anti-corrosion abilities [14], [23]
Optical	Anti-reflection coatings [24] Light based sensors [25]

This PhD thesis work is focused on magnetic nanoparticles, i.e. quasi-zero-dimensional objects, looking for strategies to transfer the unique magnetic properties conferred to these materials by their nanostructure to electronic components with common sizes, which are generally realized by “bulk” materials. Magnetic nanoparticles usually include transition metals (iron, cobalt, manganese and nickel) and/or rare-earth elements (samarium, lanthanum, niobium, etc.) to give rise to several kinds of compounds that can be classified as metals, metallic alloys, oxides, ceramic (nitrides, borides, etc.) or organometallic compounds. [26] Most of these compounds are crystalline,

although also some amorphous phases can exhibit peculiar magnetic behaviours.

As mentioned before, the fundamental motivation for investigating magnetic nanoparticles is the considerable modification in the magnetic behaviour occurring as the particle size becomes comparable to the characteristic length governing the physical properties of the system, which is in this case the domain wall width. For particles with size lower than this length, the bulk-like magnetic domain structure is no longer favourable for energy balance considerations and the so called “single domain” regime, with the related superparamagnetic behaviour, arises. Even though the direct consequences of finite-size effects, such as superparamagnetism, are the features which better identifies the nature of nanoscopic systems and are now well known by the theory, [27]–[29] other factors, such as chemical composition, crystalline structure, particle shape and morphology, concur to determine the magnetic properties of the nanoparticles. In principle, by changing one or more of these parameters it is possible to control, to a certain extent, the magnetic characteristics of the nanomaterial.

During the last decade the range of application of magnetic nanoparticles has remarkably increased thanks to the combination of the size-dependent properties with the possibility of tuning them through the control of synthetic parameters. In particular, magnetic nanoparticles are currently used as magnetic seals in motors, [30] magnetic inks, [31] magnetic recording media, [20] magnetic separation, [32] magnetic resonance contrast media (MRI), [7] highly sensitive bio-sensing assays, [21] drug delivery, [33] and magnetic hyperthermia, to cite just the most relevant applications. [10] Moreover, magnetic nanoparticles have shown promising properties, which can be exploited in the research area of electronic inductors and transformers.

Before entering into the details of the potential use of nanostructured magnetic materials for electronic devices, let us briefly recall some general concepts regarding this topic. Magnetic materials are commonly divided into two classes: hard and soft, depending on their high/low coercivity and remanence, respectively. In practice, hard magnetic materials are often identified with “permanent magnets”, because, once magnetically saturated, they are hardly demagnetized without a large magnetic field applied, while soft magnetic materials, being easily demagnetized, exhibit relevant magnetic properties (large magnetization) only when a magnetic field is applied. Both kinds of materials play a fundamental role in several electrical and electronic systems used in applications such as electrical power generation and transmission, electric motors, reception of radio signals and microwaves, relays, solenoids, magnetic shielding and electromagnets. As a consequence of the possible applications presented above, the market related to magnetic materials has strongly increased in the last decades and prevision presented in the study *Magnetic Materials Market by Type* conducted by MarketsandMarkets [34] forecasts both for hard and soft materials a further increment. The market size of magnetic materials was estimated to be $55.52 Billion in 2014 and is projected to reach $96.00 Billion by 2020, with a compounded annual growth rate (CAGR) between 2015 and 2020 of 9.6%. The market associated to soft magnetic materials and their applications is also in continuous expansion. According to the iRAP report *Soft Magnetic Materials – Technologies, Materials, Devices, New Developments, Industry Structure and Global Markets*, the 2014 global market for soft magnetic materials stood at about $45.4 Billion, and it is estimated to reach $66.6 Billion by 2019 (Figure 1.1). The CAGR is expected to be 7.9 percent from 2014 to 2019. [35]

Figure 1.1 : Global market demand for soft magnetic materials and related devices (Billions of US dollars).

Indeed, soft magnetic materials found a large use in the industry for the fabrication of electronic devices as inductors (i.e. components that store energy in the form of a magnetic field) and transformers (i.e. components which transfer electrical energy between two or more circuits, through electromagnetic induction). These types of devices are composed by soft magnetic cores inserted in electric circuits, working both in direct current (DC) or alternating current (AC). [36] They have the capability to convert electric energy in magnetic energy and contrary. Thus, the effective use of these electronic devices is strongly related to the efficiency of the conversion process and to the control of these phenomena, reducing as much as possible the dissipation of energy as heat (power losses). Therefore a key point for the applicability of soft magnetic materials in electronic devices is the power losses associated to the energy conversion process and large research efforts are devoted to find new solution for their reduction. [37] The power losses arise from different contributions, related to the constituent materials and to the preparation of the final device. As an example the relative weight of the

different contributions to the power losses in electronic devices is shown in Figure 1.2 as a function of frequency. [38]

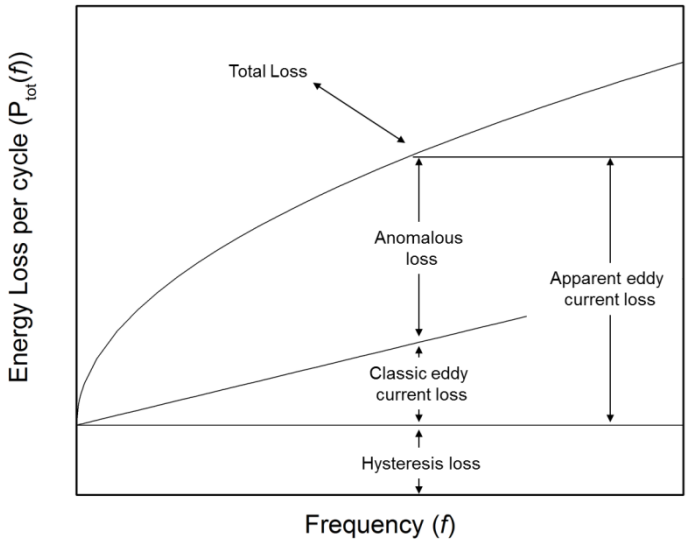

Figure 1.2 : Relative weight of the different contributions to total power losses as a function of frequency.

Currently, soft materials used for the fabrication of inductors and transformers present an optimum of operability in the range of 1-2 MHz. However, in the last years, customer demand shifted the industrial interest towards the realization of devices operating at higher frequency, up to 4 MHz. This requirement is pushing the need of finding novel materials capable to work at high frequency more efficiently than those currently employed. Nowadays, inductors and transformers are made by micrometric powders based on spinel ferrite, doped with manganese and zinc. This type of material is optimized for operating in the range 1-2 MHz and for higher frequency exhibits extraordinary increased power losses. On the other side, materials used for higher frequency application, in the range of GHz, such as micrometric spinel ferrite doped with

nickel and zinc, also exhibits high power losses, mostly due to lower relative permeability. Thus, the development of a new type of soft magnetic material, suitable for the fabrication of higher frequency operating inductors and transformers, is still an open challenge for the research in material science.

This Thesis moves within this contest, as it explores the design and development of nanostructured materials for high frequency soft electronic devices. In fact, material nano-structuration could allow a significant decrease of hysteresis losses, due to a decrease in coercive field and remanence, while keeping saturation magnetization unaltered with respect to corresponding massive materials. Moreover, since eddy current losses scale with the square of particles' radius, [39] a consistent decrease of eddy current losses should be also expected when the nano scale is attained. We focused on traditional ferrite-based magnetic materials doped with transition metal ions (manganese, zinc, nickel), paying particular attention on one hand to the synthesis of high crystalline magnetic nanoparticles with size below 10 nm and, on the other hand, on the translation and preservation of the nanostructure properties into bulk-like final products. In particular two main goals were pursued with this work:

(a) The development of a facile, cheap, eco-friendly synthetic strategy, suitable for industrial scale up, to prepare high crystalline spinel ferrite nanoparticles.

(b) The optimization of technological procedures to prepare bulk-like density, toroidal shaped, sintered products, both with micrometric and nanometric structures and with magnetic properties suitable for application in high frequency electronic devices.

The thesis is structured in the following sections:

Chapter 2. A brief summary of the theory of magnetism and of the fundamental properties of magnetic materials is presented, with particular attention to nanostructured systems and physical properties of soft magnetic devices.

Chapter 3. A brief overview on synthetic strategies for the preparation of *0D* materials is presented. In particular, we focused on bottom-up wet chemical approach. Then, the synthesis of high crystalline spinel ferrite nanoparticles and the optimization of all the parameters to satisfy all the requirements for the scale-up to industrial production are discussed. The characterization of the chemical, structural and physical properties of the nanoparticles is also presented. The Chapter ends with the fine-tuning of the measuring systems for relative permeability and core losses evaluation and the results obtained on the synthesized nanopowders. These results demonstrated the strictly relation between relative density of the samples, permeability and core losses.

Chapter 4. Basing on the results exposed in Chapter 3, the attention was thus focused on the technological optimization of compaction and sintering processes, with the aim of preparing high density final products. In this Chapter we present the two strategies adopted to realize this goal: classically sintering approach and High Pressure Field Assisted Sintering. The obtained results are presented and discussed in terms of the potential application of these materials in the field of soft magnetic devices.

Chapter 5. The final section briefly summarizes the main conclusions inferred from the experimental work presented above

and presents the perspectives for the application of these materials for the realization of soft magnetic cores for high frequency electronic inductors and transformers.

Chapter 6. The main experimental techniques used during this PhD thesis are presented and operative procedures are discussed.

References

[1] G. Cao and Y. Wang, *Nanostructures and Nanomaterials: Synthesis, Properties, and Applications*, Second Ed. SingaporeSingapore: World Scientific Publishing Co. Pte. Ltd., 2011.

[2] E. Roduner, "Size matters: why nanomaterials are different," *Chem. Soc. Rev.*, vol. 35, no. 7, p. 583, Jul. 2006.

[3] N. Taniguchi, "On the basic concept of nanotechnology," in *Proceedings of the International Conference on Production Engineering*, Tokyo: Japan Society of Precision Engineering, 1974, pp. 18–23.

[4] K. J. Klabunde, *Nanoscale Materials in Chemistry*, vol. 3. New York, USA: John Wiley & Sons, Inc., 2001.

[5] V. A. Sinani, D. S. Koktysh, B.-G. Yun, R. L. Matts, T. C. Pappas, M. Motamedi, S. N. Thomas, and N. A. Kotov, "Collagen Coating Promotes Biocompatibility of Semiconductor Nanoparticles in Stratified LBL Films," *Nano Lett.*, vol. 3, no. 9, pp. 1177–1182, Sep. 2003.

[6] Y. Zhang, N. Kohler, and M. Zhang, "Surface modification of superparamagnetic magnetite nanoparticles and their intracellular uptake," *Biomaterials*, vol. 23, no. 7, pp. 1553–1561, Apr. 2002.

[7] T.-J. Yoon, H. Lee, H. Shao, and R. Weissleder, "Highly magnetic core-shell nanoparticles with a unique magnetization mechanism.," *Angew. Chem. Int. Ed. Engl.*, vol. 50, no. 20, pp. 4663–6, May 2011.

[8] J. Gao, H. Gu, and B. Xu, "Multifunctional Magnetic Nanoparticles: Design, Synthesis, and Biomedical Applications," *Acc. Chem. Res.*, vol. 42, no. 8, pp. 1097–1107, Aug. 2009.

[9] A. Solanki, J. D. Kim, and K.-B. Lee, "Nanotechnology for regenerative medicine: nanomaterials for stem cell imaging," *Nanomedicine*, vol. 3,

no. 4, pp. 567–578, Aug. 2008.

[10] O. Salata, “Applications of nanoparticles in biology and medicine,” *J. Nanobiotechnology*, vol. 2, no. 1, p. 3, Apr. 2004.

[11] H. L. Xin, J. A. Mundy, Z. Liu, R. Cabezas, R. Hovden, L. F. Kourkoutis, J. Zhang, N. P. Subramanian, R. Makharia, F. T. Wagner, and D. A. Muller, “Atomic-Resolution Spectroscopic Imaging of Ensembles of Nanocatalyst Particles Across the Life of a Fuel Cell,” *Nano Lett.*, vol. 12, no. 1, pp. 490–497, Jan. 2012.

[12] Z. Liu, Y. Qi, and C. Lu, “High efficient ultraviolet photocatalytic activity of BiFeO3 nanoparticles synthesized by a chemical coprecipitation process,” *J. Mater. Sci. Mater. Electron.*, vol. 21, no. 4, pp. 380–384, Apr. 2010.

[13] A. Murugadoss, P. Goswami, A. Paul, and A. Chattopadhyay, “‘Green’ chitosan bound silver nanoparticles for selective C–C bond formation via in situ iodination of phenols,” *J. Mol. Catal. A Chem.*, vol. 304, no. 1–2, pp. 153–158, May 2009.

[14] F. R. Marciano, L. F. Bonetti, R. S. Pessoa, J. S. Marcuzzo, M. Massi, L. V. Santos, and V. J. Trava-Airoldi, “The improvement of DLC film lifetime using silver nanoparticles for use on space devices,” *Diam. Relat. Mater.*, vol. 17, no. 7–10, pp. 1674–1679, Jul. 2008.

[15] J. H. Fendler, “Chemical Self-assembly for Electronic Applications,” *Chem. Mater.*, vol. 13, no. 10, pp. 3196–3210, Oct. 2001.

[16] J. E. Millstone, D. F. J. Kavulak, C. H. Woo, T. W. Holcombe, E. J. Westling, A. L. Briseno, M. F. Toney, and J. M. J. Fréchet, “Synthesis, Properties, and Electronic Applications of Size-Controlled Poly(3-hexylthiophene) Nanoparticles,” *Langmuir*, vol. 26, no. 16, pp. 13056–13061, Aug. 2010.

[17] C. D. Wessells, R. A. Huggins, and Y. Cui, “Copper hexacyanoferrate battery electrodes with long cycle life and high power.,” *Nat. Commun.*, vol. 2, p. 550, Jan. 2011.

[18] B. Bogdanović, M. Felderhoff, S. Kaskel, A. Pommerin, K. Schlichte, and F. Schüth, “Improved Hydrogen Storage Properties of Ti-Doped Sodium Alanate Using Titanium Nanoparticles as Doping Agents,” *Adv. Mater.*, vol. 15, no. 12, pp. 1012–1015, Jun. 2003.

[19] X. Chen, B. Jia, J. K. Saha, B. Cai, N. Stokes, Q. Qiao, Y. Wang, Z. Shi, and M. Gu, “Broadband Enhancement in Thin-Film Amorphous Silicon Solar Cells Enabled by Nucleated Silver Nanoparticles,” *Nano Lett.*, vol. 12, no. 5, pp. 2187–2192, May 2012.

[20] G. Reiss and A. Hütten, “Magnetic nanoparticles: Applications beyond data storage,” *Nat. Mater.*, vol. 4, no. 10, pp. 725–726, Oct. 2005.

[21] H. Lee, T.-J. Yoon, and R. Weissleder, “Ultrasensitive Detection of Bacteria Using Core-Shell Nanoparticles and an NMR-Filter System,” *Angew. Chemie Int. Ed.*, vol. 48, no. 31, pp. 5657–5660, Jul. 2009.

[22] G. C. Papaefthymiou, “Nanoparticle magnetism,” *Nano Today*, vol. 4, no. 5, pp. 438–447, Oct. 2009.

[23] L. Shi, D. S. Shang, Y. S. Chen, J. Wang, J. R. Sun, and B. G. Shen, “Improved resistance switching in ZnO-based devices decorated with Ag nanoparticles,” *J. Phys. D. Appl. Phys.*, vol. 44, no. 45, p. 455305, Nov. 2011.

[24] K. C. Krogman, T. Druffel, and M. K. Sunkara, “Anti-reflective optical coatings incorporating nanoparticles,” *Nanotechnology*, vol. 16, no. 7, pp. S338–S343, Jul. 2005.

[25] J. N. Anker, W. P. Hall, O. Lyandres, N. C. Shah, J. Zhao, and R. P. Van

Duyne, “Biosensing with plasmonic nanosensors,” *Nat. Mater.*, vol. 7, no. 6, pp. 442–453, Jun. 2008.

[26] A.-H. Lu, E. L. Salabas, and F. Schüth, “Magnetic nanoparticles: synthesis, protection, functionalization, and application.,” *Angew. Chem. Int. Ed. Engl.*, vol. 46, no. 8, pp. 1222–44, Jan. 2007.

[27] D. L. Leslie-Pelecky and R. D. Rieke, “Magnetic Properties of Nanostructured Materials,” *Chem. Mater.*, vol. 8, no. 8, pp. 1770–1783, Jan. 1996.

[28] C. P. Bean and J. D. Livingston, “Superparamagnetism,” *J. Appl. Phys.*, vol. 30, no. 4, p. S120, 1959.

[29] M. Knobel, W. C. Nunes, L. M. Socolovsky, E. De Biasi, J. M. Vargas, and J. C. Denardin, “Superparamagnetism and Other Magnetic Features in Granular Materials: A Review on Ideal and Real Systems,” *J. Nanosci. Nanotechnol.*, vol. 8, no. 6, pp. 2836–2857, Apr. 2008.

[30] M. Zahn, “Magnetic Fluid and Nanoparticle Applications to Nanotechnology,” *J. Nanoparticle Res.*, vol. 3, no. 1, pp. 73–78, 2001.

[31] W. Voit, W. Voit, L. Belova, W. Zapka, and K. V. Rao, “Application of inkjet technology for the deposition of magnetic nanoparticles to form micron-scale structures,” *IEE Proc. - Sci. Meas. Technol.*, vol. 150, no. 5, pp. 252–256, Sep. 2003.

[32] I. S. Lee, N. Lee, J. Park, B. H. Kim, Y.-W. Yi, T. Kim, T. K. Kim, I. H. Lee, S. R. Paik, and T. Hyeon, “Ni/NiO Core/Shell Nanoparticles for Selective Binding and Magnetic Separation of Histidine-Tagged Proteins,” *J. Am. Chem. Soc.*, vol. 128, no. 33, pp. 10658–10659, Aug. 2006.

[33] M. Arruebo, R. Fernández-Pacheco, M. R. Ibarra, and J. Santamaría, “Magnetic nanoparticles for drug delivery,” *Nano Today*, vol. 2, no. 3,

pp. 22–32, Jun. 2007.

[34] “http://www.marketsandmarkets.com/Market-Reports/magnetic-materials-397.html.” .

[35] “http://www.magneticsmagazine.com/main/news/global-market-for-soft-magnetic-materials-estimated-to-reach-66-6-billion-by-2019/.” .

[36] “https://irapinnoresearch.wordpress.com/2015/03/26/report-summary-soft-magnetic-materials/.” .

[37] J. M. D. Coey, *Magnetism and Magnetic Materials*. 2010.

[38] B. D. Cullity and C. D. Graham, *Introduction to Magnetic Materials*, Second Ed. Wiley-IEEE Press, 2011.

[39] A. Skumiel, M. Kaczmarek-Klinowska, M. Timko, M. Molcan, and M. Rajnak, “Evaluation of power heat losses in multidomain iron particles under the influence of AC magnetic field in RF range,” *Int. J. Thermophys.*, vol. 34, no. 4, pp. 655–666, 2013.

Chapter 2

Magnetism and magnetic materials

2.1 Introduction to magnetism

In this Chapter, we will briefly remind the fundamental laws for the comprehension of the physical properties of magnetic materials. Materials are made of atoms and, thus, by electrons and nuclei. In a semi-classical picture, the magnetic moment associated to a single atom is due to the "current" produced by its electrons motion, both around their own axes (spin) and around the nucleus (orbital moment). When a material undergoes an external magnetic field (*H*), its magnetic response, described through the magnetic induction (*B*), is mainly due to the total electron moments, being the contribution ascribed to nucleus (proton and neutron spins) negligible. The relationship between *B* and *H* depends on the material and in the International System of units, (SI), is expressed as:

$$B = \mu_0 (H + M) \qquad 2.1$$

where μ_0 is the *vacuum permeability* ($\mu_0 = 4\pi \cdot 10^{-7}$ H/m in S.I and $\mu_0 = 1$ dimensionless in c.g.s. units) and *M* the magnetization of the material, defined as the total magnetic moment (*m*) of the material per unit of volume (*V*).

$$M = \frac{m}{V} \qquad 2.2$$

Magnetic materials are commonly classified in terms of their magnetic susceptibility (χ) or magnetic permeability (μ), which describe the magnetization degree of a material exposed to an external magnetic field.

The volume susceptibility is then defined as the ratio between magnetization and applied magnetic field:

$$\chi = \frac{M}{H} \qquad 2.3$$

In SI units, χ is an adimensional quantity. Similarly, the magnetic permeability μ of a material is defined as the ratio between magnetic induction B and the applied magnetic field H:

$$\mu = \frac{B}{H} \qquad 2.4$$

and is thus related to the magnetic susceptibility by the equation:

$$\mu = \mu_0(1 + \chi) \qquad 2.5$$

As mentioned before, the main element to describe the magnetism of materials is the electron magnetic moment, which comprises two components:

1. *orbital moment* ($\boldsymbol{l_e}$-), related to electron spatial movement around the atomic nucleus.
2. *spin moment* ($\boldsymbol{s_e}$-), related to the revolution of the electron around its own axis.

The atomic magnetic moment is the vector sum of the moments of all its electrons and, in accordance with Pauli exclusion principle, two cases are envisaged:

(I) All the atomic orbitals are complete and the magnetic moments of the electrons cancel one each other so that the atom has no net magnetic moment.

(II) The cancellation of electronic moments is only partial and the atoms have a net magnetic moment, i.e. orbitals in the external electronic shells are not complete.

The second class includes all the proper "magnetic materials", while the materials belonging to the first one are called "diamagnetic". Although each atom has a net magnetic moment, in the absence of an external field, not interacting magnetic moments are randomly oriented and the net magnetic moment of the material is zero.

On the other hand, in the case of interacting atomic moments a net magnetization can be observed. Indeed, neighbouring magnetic moments undergo to a force *(exchange force)*, which depends on the relative orientation of the electron spins. In particular, the *exchange interaction energy*, E_{ex}, between two atoms *i* and *j* can be written as follows:

$$E_{ex} = -2J_{ex}\boldsymbol{S_i}\boldsymbol{S_j} = -2J\boldsymbol{S_i}\boldsymbol{S_j}\cos\varphi \qquad 2.6$$

where J_{ex} is the *exchange integral* and *S* the atomic spin. If J_{ex} is positive, E_{ex} is minimized when the spins are parallel ($\cos\varphi = 1$); if J_{ex} is negative, E_{ex} has minimum when the spins are antiparallel ($\cos\varphi = -1$). Therefore, the sign and value of J_{ex}, which depends on the nature and arrangement of the interacting atoms, gives rise to different ordered magnetic materials, as reported in Table 2.1: [1]

Table 2.1 : Different magnetic materials and spin orientation in crystal lattice.

Paramagnetism (PM): no magnetic order of spins: the material shows magnetic behaviour only when exposed to an external magnetic field	**Ferromagnetic (FM)**: parallel ordered spins: a local spontaneous magnetization can be present also in the absence of an external magnetic field
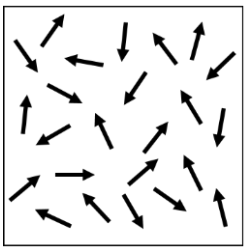	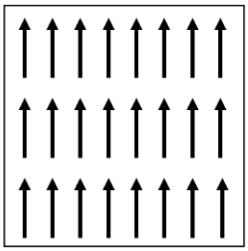
Ferrimagnetic (FiM): anti-parallel, uncompensated spins alignment: the material shows macroscopic properties similar to FM materials.	**Antiferromagnetic (AM)**: anti-parallel spin order: in the absence of an external magnetic field, the local net magnetization is null.
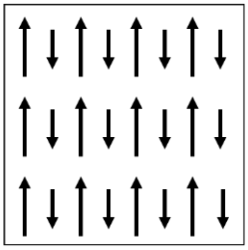	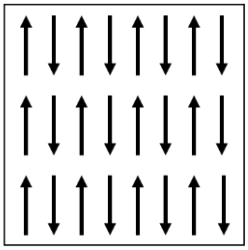

In the next sections, we will describe the properties of different magnetic materials.

2.2 Diamagnetic materials

Diamagnetism is a properties observed in all the materials when they are exposed to an external field. The change in the orbital motion of the electrons produces a field opposing to the external one. According to the *Lenz's law*:

$$\varepsilon = -\frac{\delta \Phi}{\delta t} \qquad 2.7$$

(ε, induced voltage and Φ, magnetic flux), an external magnetic field generates an extra current in the atoms by electromagnetic induction which, in turn, induces a field with opposite sign and linearly proportional to the applied field. Thus, the magnetic susceptibility of diamagnetic materials is negative. Moreover, because of the nature of the diamagnetic effect, χ is independent of the magnetic field and temperature (Figure 2.1). However, diamagnetism is such a weak phenomenon that it can be revealed only in atoms with filled electronic shells. In all the other materials, diamagnetism is overshadowed by the much stronger interactions between the atomic magnetic moments and the applied field.

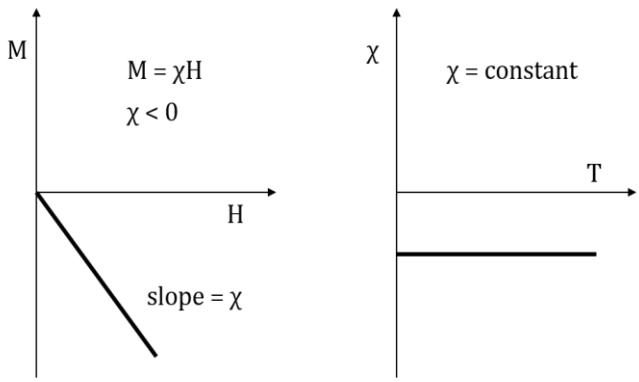

Figure 2.1 **:** Field dependence of the magnetization (left) and temperature dependence of the magnetic susceptibility (right) in diamagnetic materials.

2.3 Paramagnetic materials

Contrary to the diamagnetic ones, paramagnetic (PM) materials have unpaired electrons and, thus, present a net atomic magnetic moment. However, the weak exchange interaction among neighbours is not enough to contrast the thermal energy which causes a random alignment. Therefore, the material has no net magnetic moment until a magnetic field is applied. Indeed, under an external field, the atomic moments start to align resulting in a macroscopic magnetization of the material. For small applied fields, only a fraction of atomic moments is deflected along the field direction, providing a magnetization which increases linearly with the applied field. A further increase of the applied field results in a deviation from the linear behaviour until saturation is reached when all atomic moments are aligned with the field. The *M* vs *H* behaviour is described by the Brillouin function:

$$B_J(x) = \frac{2J+1}{2J}\coth\left(\frac{2J+1}{2J}x\right) - \frac{1}{2J}\coth\left(\frac{1}{2J}x\right) \qquad 2.8$$

where $x = mH/k_BT$, k_B being the Boltzmann's constant and *J* is the total angular momentum quantum number and can assume positive integer or half integer values. In the classical limit ($J \to \infty$) the Brillouin function reduces to the Langevin function:

$$L(x) = \coth(x) - \frac{1}{x} \qquad 2.9$$

Moreover, as described by Curie's Law (Equation 2.10), the alignment degree decreases as temperature increases because of the misalignment of the moments produced by the enhancement of thermal energy.

$$\chi = \frac{C}{T} \qquad 2.10$$

According to Equation *2.10* χ is inversely proportional to the temperature, through the Curie constant, *C*, which depends on the specific material. Assuming that the orbital moment, is quenched, C is given by:

$$C = \frac{N_A\, g^2 \mu_B^2 S(S+1)}{3k_B} \qquad 2.11$$

where N_A is the Avogadro number, *g* the Landé factor, μ_B the Bohr magneton and *S* the total atomic spin.

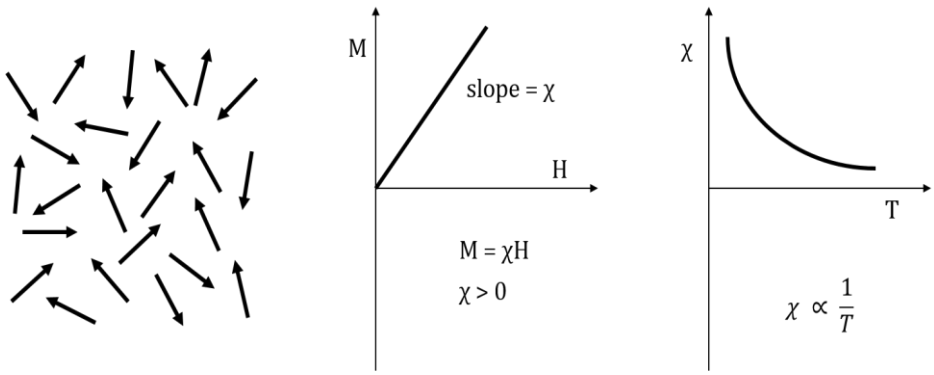

Figure 2.2 **:** From the left: spin orientation with no magnetic field applied, low field dependence of the magnetization and temperature dependence of the magnetic susceptibility in paramagnetic materials.

2.4 Ordered magnetic materials

Diamagnetic and paramagnetic materials show a magnetic behaviour only in the presence of an applied field. However, there exists a critical temperature below which some materials exhibit a magnetic ordered structure. Like paramagnets, ferromagnetic (FM), ferrimagnetic (FiM) and antiferromagnetic (AFM) materials have unpaired electrons and the magnetic moments, as described in Table 2.1, can be aligned in a parallel (J_{ex} is positive) or antiparallel (J_{ex} is negative) way. The magnetic configuration of an ordered magnetic material depends on the competition among the various contributions to the total magnetic energy. Here we briefly summarize the most important contributions for bulk materials [1], [2]:

- *Exchange interaction energy* (E_{ex})*:* introduced in Equation 2.6, it has a quantum mechanical origin and is responsible for spin alignment in ordered structures, promoting, as already mentioned, the ferromagnetic or antiferromagnetic coupling between neighbouring atoms. This kind of interaction comes from the overlap between atomic or molecular orbitals and is related to the exchange energy between electrons. The exchange interaction can be roughly divided in two main classes: the direct exchange, when the orbitals of atoms carrying the magnetic moment directly overlap, and super exchange, when the interaction between two magnetic centers is mediated by a diamagnetic atom.
- *Magnetic dipole interaction energy*: this contribution arises from the dipole-dipole interactions between two magnetic moments and is also called dipolar coupling. This interaction is proportional to the module of the involved magnetic moments and is inversely proportional to the cube of the distance between them. Despite dipolar energy is weak

compared to the exchange energy, in those materials where no stronger interactions are present, it can induce magnetic order at very low temperature.

- *Magnetostatic energy*: it originates from the interaction of a magnetic body with the field it creates by itself, or possibly with an external magnetic field. In other words for a magnetic body, even in the absence of an external magnetic field, magnetostatic energy is generated within the body itself by the internal magnetic field created by its magnetization.
- *Magnetocrystalline anisotropy energy:* is a well-known experimental fact that some crystals can be more easily magnetized along certain directions, called easy axes of magnetization, than in others. This is an intrinsic property of the material related to crystal symmetry and to the atom arrangement in the crystal lattice. The origin of this contribution arises from the fact that orbital wave function reflects the symmetry of the lattice and this influences the spins through spin-orbit coupling.

2.4.1 Ferromagnetic materials

Since the atomic moments of FM materials are parallelly ordered (J_{ex} is positive), they are characterized by the presence of a net magnetic moment, at the local level (see Section 2.5), even without an applied field. This spontaneous magnetization is maximum at 0 K (M_0), where all the atomic moments are perfectly aligned. As the temperature increases, the thermal energy introduces some disorder in the alignment, which makes the magnetization to decrease until a critical temperature, called *Curie temperature* (T_C), where the thermal energy overcomes the exchange one and

the material assumes a PM behaviour (Figure 2.3). Therefore, T_C depends on the strength of the exchange interaction between the atomic magnetic moments and it is typical of each considered material. The temperature dependence of susceptibility is expressed by the *Curie-Weiss law*:

$$\chi = \frac{C}{T - \theta} \qquad 2.12$$

where Θ is the temperature at which the susceptibility diverges, which corresponds to T_C for the FM material.

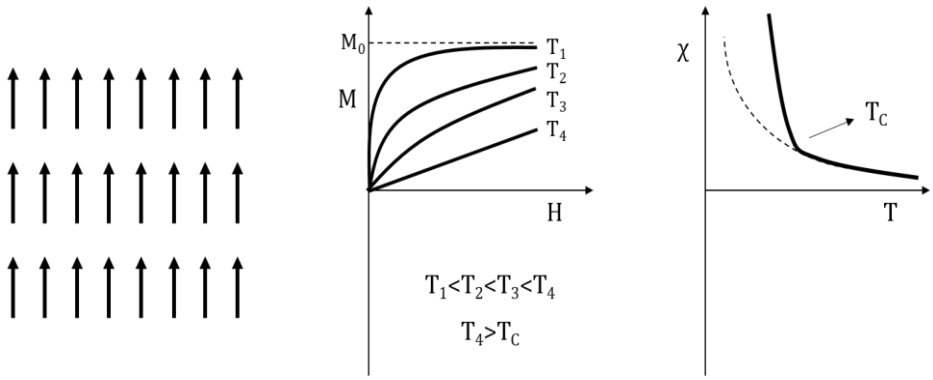

Figure 2.3 **:** From the left: relative spin orientation when no magnetic field is applied (at T = 0 K); field dependence of first magnetization at different temperatures; temperature dependence of magnetic susceptibility of FM materials.

2.4.2 Antiferromagnetic and Ferrimagnetic materials

Contrary to FM materials, FiM and AFM ones present negative values of J_{ex}, leading to an antiparallel alignment of neighbouring atomic magnetic moments. Such materials can be schematized through the combination of two antiparallel aligned magnetic sub-lattices, inside of which magnetic moments are parallel-aligned. While in AFM materials the magnetic sub-lattices

compensate each other nullifying the total magnetization, in FiM systems they have different amplitude, resulting in a net magnetization. Therefore, FiM materials can be considered as FM ones where the net magnetization corresponds to the difference between the values of the two sub-lattices. Consequently, FiM materials can be treated as FM ones and their behaviour can be described by the *Curie-Weiss law* (Equation 2.12), with a characteristic ordering temperature (T_C) above which the material becomes PM. Similarly, AFM materials are characterized by an ordering temperature, called *Néel temperature* (T_N), above which they start to behave like PM. Indeed, above T_N, AFM materials follow the *Curie-Weiss law* (Equation 2.12), where Θ has a negative value. In Figure 2.5, the dependence of the susceptibility on temperature is summarized for the different classes of magnetic materials.

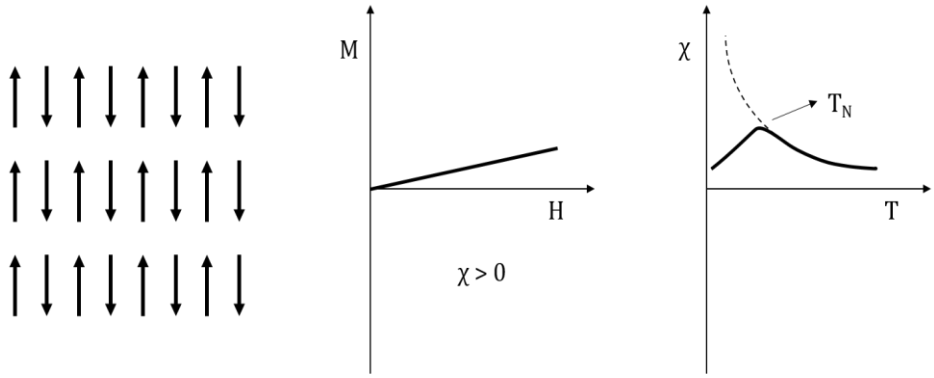

Figure 2.4 **:** From the left: relative spin orientation when no magnetic field is applied (at T = 0 K), field dependence of magnetization and temperature dependence of magnetic susceptibility in antiferromagnetic materials.

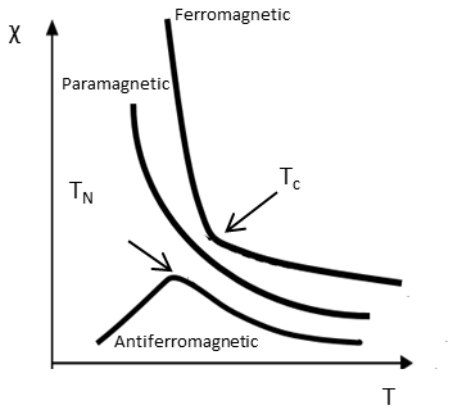

Figure 2.5 : Schematic representation of magnetic susceptibility as a function of temperature for PM, FM an AFM materials.

2.4.3 Hysteresis in ordered magnetic materials.

The response of an ordered magnetic material to an external magnetic field depends on its specific magnetic structure. Ferromagnetic materials present a hysteretic response of their magnetization to an applied field. When a magnetic field is applied the magnetization increases till the field becomes sufficiently high to align all the magnetic moments along its direction. The magnetization under this condition is called saturation magnetization (M_S). Once the field is removed, the magnetic moment does not become zero but goes to a finite value, known as remanent magnetization (M_R). To obtain zero magnetization an additional negative magnetic field is needed, named coercivity (H_C) (Figure 2.6). As described before, when the temperature of the material overcomes T_C the thermal energy is higher than the exchange interaction between neighbouring atoms and the spins can rotate independently and randomly, and the ferromagnetic solid becomes

paramagnetic, losing M_R and H_C. Similarly, FiM materials exhibit magnetic hysteresis, with non-zero M_S, M_R and H_C below the ordering temperature.

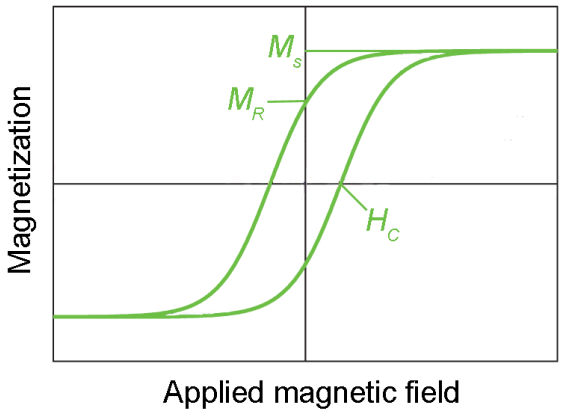

Figure 2.6 **:** Magnetization as a function of the applied magnetic field for a ferro- or ferrimagnetic material; M_S, M_R and H_C indicates the saturation magnetization, remanence and coercivity, respectively.

FM and FiM materials can be further classified as soft or hard magnets. Hard magnets, which are used to realize permanent magnets, require a large magnetic field to be demagnetized and generally at room temperature have a large remanence and coercivity (H_C > 1000 Oe) and a relatively small saturation magnetization. Conversely, soft magnets are easily magnetized and demagnetized, they have a small coercive field, large saturation magnetization and a small remanent magnetization. Soft and hard magnets, or their combinations, cover a wide range of different applications for satisfying multiple requirements of industrial devices. The hysteretic response originates from the magnetic domain structure described in the next paragraph (Section 2.5).

2.5 Magnetic domains

When we described the alignment in magnetic ordered materials, we stressed the “local” nature of this phenomenon (Table 2.1). Indeed, even though the exchange and magneto-crystalline energies tend to align all the spins in the easy axis direction, the resulting macroscopic magnetization gives rise to a polarization on the material surface, which originates an additional contribution to the total energy, i.e. the magnetostatic energy. The spin configuration which minimizes this energy term implies the formation of magnetic domains (Figure 2.7), which are uniformly magnetized regions with different shape and size. The orientations of the spins in different domains are different, so that the net magnetization is zero in the absence of an external magnetic field, thus reducing the internal field generated (*demagnetizing field* (H_d).

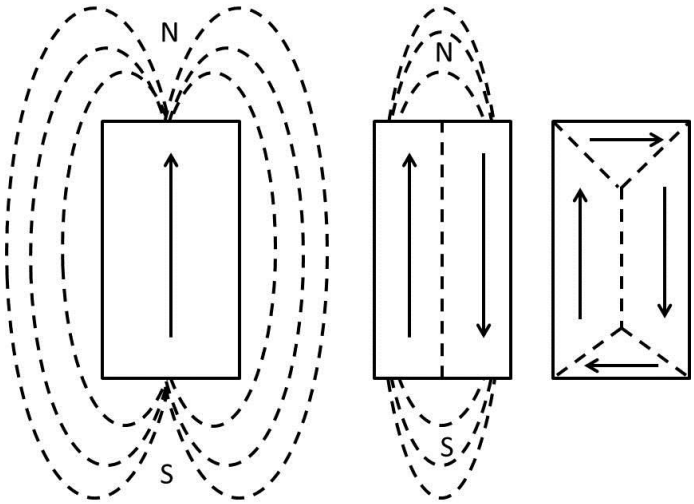

Figure 2.7 : Reduction of the demagnetizing field due by domain formation.

Two adjacent domains are separated by domain walls (Bloch walls) that are transition regions characterized by a gradual rotation of the spins from a domain to the other. The formation of domain walls adds another energy contribution. The schematic representation of a 180° domain wall in a FM material, reported in Figure 2.8, illustrates this contribution: each magnetic moment within the wall is not exactly parallel to the next one, so that the exchange energy is higher inside the domain wall than in the domain. In addition, the dipole moments of the atoms within the wall are not pointing along the easy direction of magnetization, thus they also increase the magnetocrystalline energy.

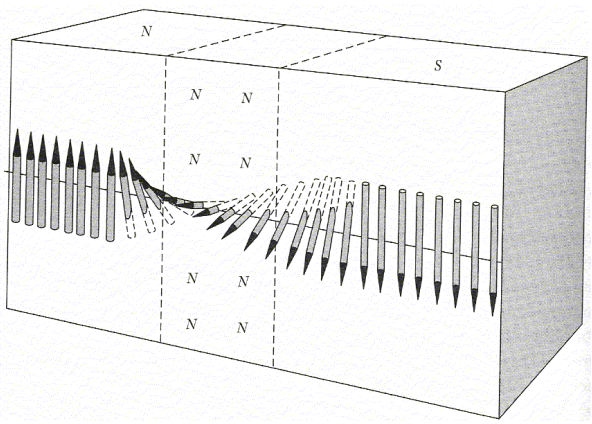

Figure 2.8 : Schematic representation of a 180° domain wall.

The energy contribution per units of area associated to the formation of domain wall is called *domain wall energy*, E_w and depends on the material magnetocrystalline anisotropy and on the strength of the exchange interaction between neighbouring atoms:

$$E_w = 2\sqrt{KA} \qquad 2.13$$

where K is the anisotropy energy constant and A is the exchange energy density.

The thickness of the walls (δ) will also vary in relation to these parameters as described by the following equation:

$$\delta = \pi \sqrt{\frac{A}{K}} \qquad 2.14$$

Therefore, a strong magnetocrystalline anisotropy favours narrow walls, whereas a strong exchange interaction favours wide walls. Accordingly, a global minimum energy of the system can be achieved by the balance between exchange, magnetostatic and magnetocrystalline energies, resulting in a specific number, size and shape of domains that will depend on the composition, crystallographic structure, size and shape of the material.

The presence of domains strongly determines the magnetic behaviour of FM and FiM, materials. In fact, while in the absence of an applied field, the domains are arranged to reduce the magnetostatic energy and therefore the material net magnetization, when an external field is applied, the domain with magnetization parallel to the field direction starts to grow by wall motion, as shown in Figure 2.9.

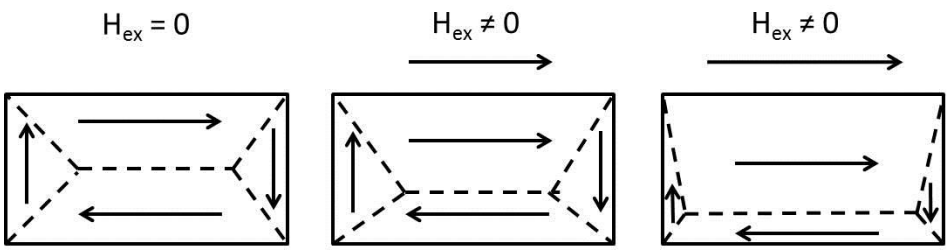

Figure 2.9 : Schematic representation of the domain wall motion as an external field is applied.

Once only one domain remains and all magnetic moments are aligned with the applied field, the maximum value of magnetization is reached and a further increase of the external field does not lead to a magnetization enhancement (magnetization saturation)

2.6 Magnetic properties of nanoparticles

Matter behaves differently when its size is reduced to the nanoscale. In general, structure-sensitive properties are affected by *finite-size effects* once the size of the material is comparable to their characteristic length scale. In particular, the domain wall thickness, which falls in the nanometric range, is one of the characteristic lengths affecting material magnetic behaviour. Moreover, the enhancement of surface to volume ratio, characteristic of nanostructured materials, increases the relevance of some specific effects, such as surface anisotropy, atomic disorder, spin frustration and core-surface extra exchange anisotropy [3]–[5], which are generally negligible for bulk material.

2.6.1 Single domain magnetic nanoparticles

The formation of magnetic domains in bulk materials occurs to reduce the magnetostatic energy of the system. However, when the size of the material becomes smaller than the domain wall thickness, the energy gained from the formation of a multi domain structure is higher than the energy spent for the wall formation. A single domain spin configuration is then preferred. Considering a spherical particle, the critical diameter (d_{sd}), below which single domain structure occurs is given by the following equation: [6]–[8]

$$d_{sd} = \frac{18E_w}{\mu_0 M_S^2} \qquad 2.15$$

In most common magnetic material d_{sd} is in the range of 20-800 nm, depending on its saturation magnetization, anisotropy and exchange energy. [6]

Table 2.2 **:** Critical single domain diameter for some materials of interest

Magnetic material	d_{sd} **(nm)**
Co	70
Fe	14
Ni	55
Fe_3O_4	128
$CoFe_2O_4$	128
$MnFe_2O_4$	50

One consequence of the single domain configuration is that changes in the material magnetization cannot longer occur through domain wall motion but require the coherent rotation of all the spins, resulting in an enhancement in the coercivity of the system. [9] Since the atomic moment interaction is kept unchanged during the reorientation, the magnetic properties can then be described by a total magnetic moment (μ) obtained by the vectorial sum of the single atomic spins, which can be defined as:

$$\mu = M_S V \qquad 2.16$$

where V is the average nanoparticles volume.

The Stoner and Wohlfarth model [10] describes the energy related to the magnetization reversal in terms of the material anisotropy. The model assumes a coherent rotation of all the spin in a particle and the presence of

uniaxial anisotropy (a single easy axis of magnetization) thus the energy density of the system can be written as:

$$E_B = KVsin^2(\theta) + HM_S cos(\phi - \theta) \qquad 2.17$$

where Θ is the angle between M and the magnetization easy axis, and ϕ the angle between H and the magnetization easy axis (Figure 2.10). The first term ($KVsin^2(\Theta)$) refers to the magnetic anisotropy and the second one ($HMcos(\phi-\Theta)$) is the Zeeman energy corresponding to the torque energy on the particle moment by the external field. As illustrated in Figure 2.10, when $H=0$ the Zeeman term is zero and there exist two equilibrium states for $\Theta=0$ and $\Theta=\pi$. The energy barrier separating these two states is equal to KV. This is the magnetic anisotropy energy of the system, [11] and corresponds to the energy necessary for the reverse of magnetization to occur.

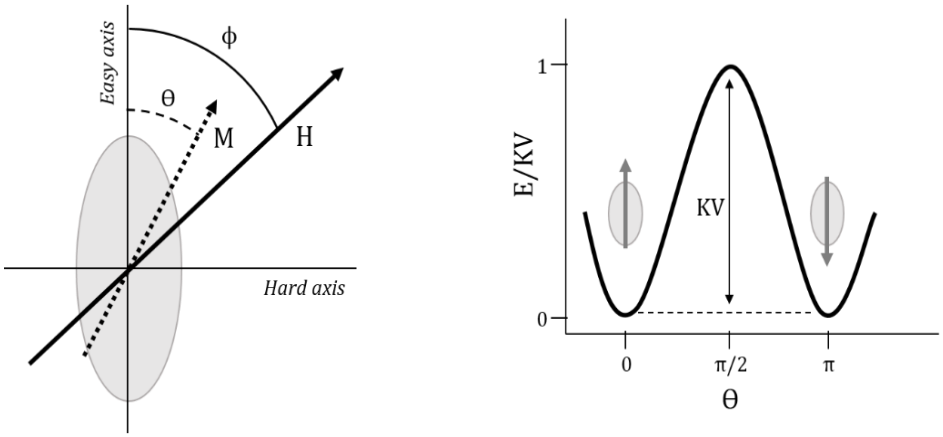

Figure 2.10 : Stoner and Wohlfarth model: definition of the axis system (*left*) and angular dependence of the energy for a zero external field (*right*).

On the other hand, for a fixed temperature, the presence of an applied field will modify the particle energy through the Zeeman term, making the minimum corresponding to the parallel orientation with respect to the

external field, progressively more stable till, when $H_a \geq 2K/M_S$ only a single minimum will be present. H_0 is called *anisotropy field*.

2.6.2 Superparamagnetism

As described above, the energy barrier of a single domain particle with uniaxial anisotropy is *KV.* As the volume decreases, it becomes increasingly smaller. Eventually, for particle of few nanometers, the term *KV* becomes sufficiently small that, even in the absence of an external field, the thermal energy (k_BT, where k_B is the Boltzmann's constant) is sufficient to induce magnetization fluctuations in all directions, included its reverse from one direction of the easy axis to the other. In these conditions, the system behaves like a paramagnet, where the atomic spins are replaced by the single particle magnetic moment, whose value is much higher, because it corresponds to the sum of 10^2-10^5 spins (superparamagnetic regime). [9], [11], [12] The temperature at which the system reaches the superparamagnetic state depends, for a given time window, on the particle volume and anisotropy.

The magnetic behaviour of single domain particles is strongly time dependent and the observed magnetic state of the system depends on the characteristic measuring time of the used experimental technique, τ_m. Indeed, for a given temperature, it is possible to introduce a *relaxation time*, (τ), which describes the time required by the magnetic moment to reverse its orientation:

$$\tau = \tau_0 \exp\left(\frac{KV}{k_B T}\right)_B \qquad 2.18$$

where τ_0 is a time constant characteristic of the material and usually is of the order of 10^{-9}-10^{-12} s for non-interacting FM and FiM nanoparticles. Thus, it can

be defined a temperature, called *blocking temperature* (T_B), at which the relaxation time equals the measuring one ($\tau = \tau_m$):

$$T_B = \frac{KV}{k_B ln\left(\frac{\tau_m}{\tau_0}\right)} \qquad 2.19$$

Consequently, being T_B dependent on the time scale of the measurements, two conditions occur:

- $\tau_m > \tau$: the system reaches the thermodynamic equilibrium in the experimental time window and a superparamagnetic behaviour is observed;
- $\tau_m < \tau$: quasi-static properties, similar to bulk materials, are obtained and particles are in the *blocked regime*.

Therefore, a nanoparticle's assembly at a given temperature can be both in superparamagnetic or blocked regime depending on the measuring technique. For typical DC magnetization measurement as those often used in this work, τ_m is ca. 100 s and, assuming $\tau_0 = 10^9$, the above equation becomes:

$$T_B = \frac{KV}{25k_B} \qquad 2.20$$

It should be reminded that, these relations are obtained for monodisperse, non-interacting, single domain nanoparticles. In fact, being T_B proportional to the volume of the particles, the presence of a size distribution implies also a distribution of T_B values. Besides, inter-particle interactions, which will be discussed later, can increase T_B due to extra energy terms introduced by the dipolar and/or exchange interactions.

2.6.3 Surface effects

In the previous paragraphs, it has been reported how *finite-size effects* affect the magnetic properties of nanoparticles; however, the reduction of particles size to the nanoscale leads to further modification of the material magnetic behaviour due to the increased ratio between surface and volume. In fact, in particles of few nanometers, the number of atoms on the surface is no longer negligible with respect to the inner atoms and *surface effects* become relevant. Surface atoms suffer from the break in the coordination sphere resulting in a lack of symmetry, which leads to deviation from the parallel or antiparallel alignment. This phenomenon, often denoted as "surface spin disorder" can be described evoking spin canting, frustration and spin-glass behaviour. [3], [11] In particular, *spin canting* arises from the fact that a change in the surface atom coordination can modify the ligand field, so that a local change in the direction of the magnetization easy axis can occur, canting the superficial spin with respect to the inner ones. [13], [14] Magnetic *frustration* arises from the reduced numbers of magnetic neighbours at the particle surface or around defects in the interior. [15]–[17] As a result of spin canting and frustration, a deficiency of long-range magnetic ordering can occur, leading to the so-called *spin-glass-like* behaviour. [18], [19]

In this picture, the previous model where all the spins undergo to the coherent reversal of the magnetization is too rough and the system can be described as composed of two phases: a crystalline core governed by the previous discussed model, and a disordered surface layer with a more complex behaviour, whose main effect can be summed up as an additional contribution to the total anisotropy of the system (surface anisotropy), [3], [11], [20]. Due to the increasing weight of the surface anisotropy contribution upon size reduction, the increase in H_C is strongly related to the particle size. [21]

Moreover, the presence of the surface disorder affects also the saturation magnetization of the material, resulting both in a reduction or enhancement of M_S. Interestingly, also AFM nanoparticles present novel properties which are drastically different from the bulk ones due to surface and finite-size effects. Particularly, below T_N the presence of the surface magnetism can lead to FM-like behaviour, with finite M_S and large H_C. Other effects such as changes in T_N can also take place. [22]–[24]

2.6.4 The role of magnetic interactions

The magnetic moment of a FM or FiM nanoparticle can interact with the magnetic moment of neighbouring ones either by direct exchange, if the particle are in close contact one to each other, or through the space. The latter, known as *dipole-dipole interaction*, is a long-range anisotropic interaction whose strength depends on the distance between the nanoparticles and on the degree of the mutual alignment. In particular, dipole-dipole interactions modify the particle energy barrier, KV, which, within the limit of weak interactions, becomes:

$$E_a = V(K + H_{int}M) \qquad 2.21$$

where H_{int} represents the *mean interaction field*. [25] Extensive experimental and theoretical works agree that the interaction among magnetic particles plays a fundamental role in the magnetic behaviour of nanoparticle systems. [26]–[31] The results, however, are often contradictory. For example, either an increase or a decrease of T_B with the strength of dipolar interaction, i.e. increasing particle concentration or decreasing interparticle distance, have been foreseen and experimentally reported [25], [27]–[29], [31]. Dipole-dipole interactions can also affect the shape of the hysteresis loop: when the particles

are randomly oriented, the reduction of the inter-particle distance can decrease the coercivity [32], [33][34] In contrast, when the particles are not randomly oriented the coercivity can increase or decrease, depending on the type of arrangement. [35], [36]

If nanoparticles are so close to be almost in touch, *exchange interactions* between surface atoms can also be envisaged because of the overlap of their wave functions, inducing a modification of the energy barrier of the system. Again, being this interaction related to surface atoms it is appreciable only in nanostructured materials when the surface-to-volume ratio is large. However, in most of the single-phase magnetic nanoparticles synthesized via wet chemistry, exchange inter-particle effects are avoided due to organic molecules covering the particles. Conversely, these effects can become relevant for nanostructure synthesized via wet chemistry methodology without the use of organic surfactants.

2.7 Soft magnetic materials

As described above, magnetic materials can be classified in two main classes, according to their magnetic properties:

a) *Hard* magnetic materials, which are characterized by high H_C values (few thousand of Oe).
b) *Soft* magnetic materials, which are characterized by low H_C values (hundreds of Oe).

Considering the aim of this work in the following we will focus on soft magnetic materials only. A good soft magnetic material exhibits minimal hysteresis, low magnetostriction, and high saturation magnetization and permeability values. Permeability is often reported as relative permeability, (μ_r) with respect to vacuum.

$$B = \mu_0 \, \mu_r \, H \qquad 2.22$$

$$\mu_r = \frac{\mu}{\mu_0} \qquad 2.23$$

The relative permeability is a pure number. Soft materials may be used for DC (direct current) or AC (alternating current) applications. In the latter case, a short overview of most common metal and oxides magnetic material, and the corresponding applications at different working frequency is provided in Table 2.3. [37] Metals are employed in the kHz range, but insulating ferrites are needed to concentrate flux and generate electromotive forces (*emf*) in the radio-frequency and microwave ranges, in order to avoid eddy-current losses (see further section).

Table 2.3 : Description of common magnetic material and their application depending on AC field frequency.

Frequency	**Magnetic materials**	**Applications**
<1 Hz (Static)	Fe-Co (permendur); Ni-Fe (permalloy);	Electromagnets, relays
1Hz – 1kHz (Low frequency)	Si steel; permalloy; magnetic glasses	Transformers, motors, generators
100Hz – 100kHz (Audio-frequency)	Permalloy; magnetic glasses; Fe-Si-Al powder (sendust); Mn-Zn Ferrite	Inductors, transformers for switched mode power supplies
100kHz – 1GHz (Radio-frequency)	Mn-Zn Ferrite; Ni-Zn Ferrite	Inductors, antenna rods
>1GHz (Microwaves)	Yttrium Iron Garnet (YIG); Li-Ferrite	Microwave isolators, circulators, phase shifters, filters

Energy losses, i.e. the energy lost in the AC magnetization cycle of a magnetic material, are critical in any application. Traditionally three main sources were identified in soft metallic materials operating at low frequency:

- Hysteresis Losses (P_{hy})
- Eddy current Losses (P_{ed})
- Anomalous Losses (P_{an})

The total losses are the sum of these three contributions:

$$\mathbf{P}_{tot} = \mathbf{P}_{hy} + \mathbf{P}_{ed} + \mathbf{P}_{an} \qquad 2.24$$

2.7.1 AC energy losses for magnetic materials.

As described above energy losses arise from different contributions and in this paragraph we will briefly describe each one of them. Hysteresis losses are associated to the magnetic irreversibility characteristic of FM and FiM materials and are proportional to the area of the *M (H')* loop. In other words, when a magnetic specimen is driven through one complete hysteresis cycle, the total work done on the specimen, who appears as heat, is the hysteresis loss. Indeed, when a uniformly magnetized sample is considered, the energy increment per unit volume, i.e. the variation of the work on the system (δW) is proportional to the applied field H and to the flux B variation:

$$\delta W = H \bullet \delta B \qquad 2.25$$

Actually, since the external applied field is perturbed by the demagnetizing field, H_d, generated by the magnetic material itself, it is more appropriate to consider in place of H, an H' field, $H' = H + H_d$. Moreover, considering the relation between H, B and M (Equation 2.1), the expression which describes the work done on a material by the application of an external field becomes:

$$\delta W' = \mu_0 H' \bullet \delta M \qquad 2.26$$

where M is the magnetization of the material. Thus, if the M(H) curve of the material is not reversible, the energy that will be expended to cycle the field is equal to the hysteresis loop's area, (Figure 2.11).

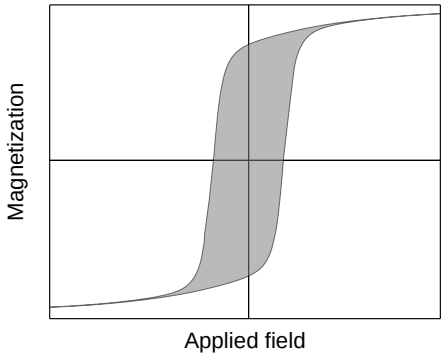

Figure 2.11 : The grey zone represents the work associated to a hysteresis loop produced by an external field.

When the external field is generated by an alternating current, we should consider the number of single cycle per unit of time performed by the material in response to the AC field. Thus, the hysteresis losses occurring for an AC field of frequency f are proportional to the hysteresis losses of a single loop multiplied by the frequency:

$$P_{hy} = f\,\mu_0 \int_{loop} H' dM \qquad 2.27$$

Hysteresis losses can be decreased working on the soft characteristic of the material. For example, if the field frequency is kept constant, they can be modulated by tuning the parameters which determines the hysteresis area determination (saturation magnetization, coercivity and squareness).

The second contribution in the sum of Equation 2.24 is the eddy current losses. They are always present when a conducting material undergoes to an alternating field. The induced currents dissipate their energy as heat (Joule

effect). Considering a sheet of thickness t and resistivity ρ cycled to a maximum induction B_{max}, the losses P_{ed} are given by:

$$P_{ed} = \frac{(\pi\, t\, f\, B_{max})^2}{6\rho} \qquad 2.28$$

Usually, eddy current losses can be decreased using lamination or high resistive materials. One of the most used class of material is transition metal oxides, because of the low electrical conductivity, compared to metallic materials. In the case of spherical magnetic grains eddy current losses are described by an equation similar to Equation 2.28, where t is replaced by the average diameter (d), so that $P_{ed} \propto d^2$. This means that eddy current contribution is almost negligible for small, nanometric particles while it becomes progressively more and more relevant for size above the single domain critical diameter. [38]

Anomalous losses, which, as stated above, comprise all the extra contributions to losses, are generally comparable in magnitude with eddy current ones and arise from extra eddy current losses due to domain wall motion, non-uniform magnetization and sample inhomogeneity.

Despite the complexity of the problem, Pry and Bean model provides an expression to evaluate the anomalous losses, in the simplified case of an electrical conductive sheet with a structure of n uniformly spaced domains with separation d, with a thickness cross section τ, which expand and contract in an AC field applied parallel to the walls:

$$P_{an} = \frac{(4\, f\, B_{max})^2 d\tau}{\pi\rho} \sum_{n\ odd} \frac{1}{n^3} \coth\left(\frac{n\pi d}{\tau}\right) \qquad 2.29$$

Anomalous losses are reduced by increasing the number of domains, which corresponds to decrease the distance a wall must travel during the magnetization process. Similarly to eddy current losses, anomalous losses are negligible for materials with size in the nanometer range.

2.7.2 AC electronic circuit

Energy losses associated with an AC field arise from all the contributions described before, but a precise evaluation of each contribution using the standard magnetometric techniques discussed in Chapter 6 is not possible. However, an evaluation of the total power losses can be realized using non-commercial techniques. The simplest way to measure core losses requires the assembling of an inductor. An inductor is an ideal circuital component able to store magnetic energy. In practice, the typical inductor consists in a magnetic core wound up with conductive wire loops or coils. The current flowing in the coils produces an electric field which induces a magnetic field in the core. Inductors are produced with different shapes, but most of them are based on a toroidal geometry (Figure 2.12) because it allows the uniformity of flux *B* in the core, avoiding, thanks to its shape, demagnetization effect.

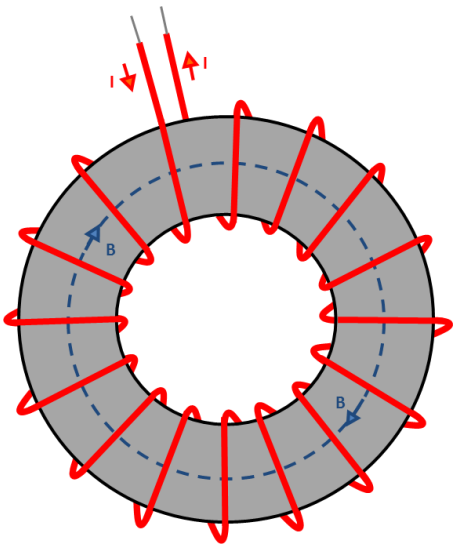

Figure 2.12 : Scheme of a toroidal shape inductor with wire coils. A current, *I*, produces a uniform flux *B* in the core.

In order to describe the electromagnetic properties of inductors, a brief overview on the physical laws related to electric circuits is needed. When a magnetic toroid is exposed to an electric field generated by wire coils, a magnetic induction *B* is produced in the material. If a DC current is used, the magnetic flux will be proportional to the generating current *I*, which is determined only by the resistance *R* of the wires. When the same electric field is generated by an AC current with angular frequency *ω*, other properties of the system, which are described by complex quantities, must be considered. One is the impedance, i.e. the measure of the opposition of the circuit to the flow of current, allows to extend the DC concept of resistance to AC circuit, including information about both magnitude and phase. Two additional properties are the induction of voltages in conductors induced by a variation in the magnetic fields (change of current) which is described by the inductance (*L,* expressed in Henry, *H*); the electrostatic storage of charge induced by a different potential between conductors, which is described by capacitance(*C,* expressed in Farad, *F*). The sum of these two opposing effects is referred as reactance (*X*) and represents the imaginary part of complex impedance (*Z*), whereas resistance (*R,* expressed in Ohm, Ω) represents its real part, as:

$$Z = R + jX \qquad 2.30$$

To better understand the meaning of these three basic components and the correlation between *R* and *X* in ideal systems, separate circuits for each one of them is now analysed. The impedance, Z_R, of an ideal resistor, i.e. passive electrical component used to increment electric resistance in circuits and thus to decrease the current passage (amplitude), is purely real and does not produce any change in the phase of voltage and current, independently of frequency:

$$Z_R = R \qquad 2.31$$

On the other hand, ideal inductors and capacitors, i.e. electrical component used to temporarily store electrical or magnetic energy of the electromotive field, referred as Z_L and Z_C, are purely imaginary and are linearly or inversely proportional, respectively, to the frequency ω:

$$Z_L = j\omega L \qquad Z_C = \frac{1}{j\omega C} = \frac{-j}{\omega C} \qquad 2.32$$

The frequency dependence of the three ideal components of the impedance is shown in Figure 2.13.

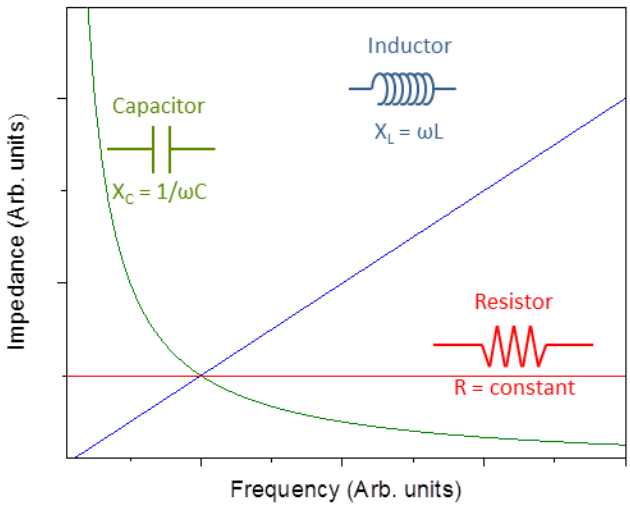

Figure 2.13 : Behaviours of inductors, capacitors and resistors as a function of frequency.

However, a device which owns only one of these features exists only for ideal system. In fact, in principle, every real device presents both real and imaginary components, one of which, sometimes, can be neglected depending on the specific applications, and, particularly of the operating frequency. Focusing the attention on inductors, for instance, they are made by magnetic core and wound up with wire coils. Thus, a resistance due to the wires used for the

loops should be considered together with the inductance. Moreover, for ideal system the resistance associated to the inductor should be constant with frequency. However, considering the presence of hysteresis in the magnetic core, the generated eddy currents and the wire skin effect, i.e. the increase of the conductors resistance at high frequency due to densification of the AC current flow near the surface, determine energy losses which can be suitably described by an increase of the real part *R* of impedance with the frequency.[39] Furthermore, another contribution to the energy losses in inductors is related to the accumulation of charge between the wire loops, leading to behaviour as capacitors. Thus, a real inductor could be schematized as shown in Figure 2.14, with the *R* and *L* contributions in series and *C* in parallel.

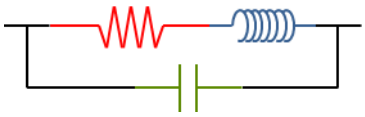

Figure 2.14 : Real inductor schematization with resistive, capacitive and inductive contributions.

The total impedance of the circuital element of Figure 2.14 is thus:

$$Z = (Z_R + Z_L)/Z_C = \frac{R + j\omega[L(1-\omega^2 LC) - CR^2]}{(1-\omega^2 LC)^2 + \omega^2 C^2 R^2} \qquad 2.33$$

For frequencies in the range 100 kHz - 2 MHz, the inductance contribute dominates, but both capacitance and resistance are present. On increasing frequency, the capacitance contribution becomes more relevant. The evolution of the imaginary part of the impedance as a function of frequency is shown in Figure 2.15. For low frequencies (red zone) the system has a pure inductive behaviour; increasing ω the capacitive contribution becomes more and more relevant (blue zone), until a certain frequency (*resonance frequency)*

where Z_L and Z_C are equal and the imaginary part is zero. On further increasing the frequency, the system has a pure capacitance behaviour (green zone). The frequency of resonance is a specific property of each circuit.

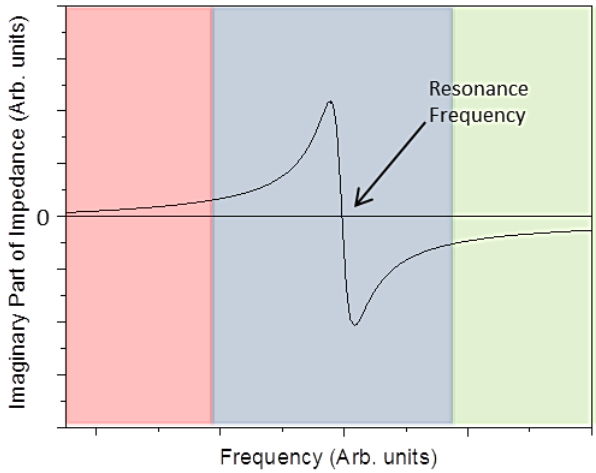

Figure 2.15 : Imaginary part of impedance as a function of frequency.

As described before, the resistance *R* should be constant with frequency, but the sides effects determine an increase in the resistance value. Moreover, at the resonance frequency Z_L=Z_C and therefore $\omega^2 LC=1$ the imaginary component in Equation 2.32 vanishes; thus, the impedance at the resonance becomes:

$$Z_{\omega R} = \frac{R}{\omega^2 C^2 R^2} \qquad 2.34$$

Thus, plotting the real part of impedance as a function of frequency (Figure 2.16), it is possible to visualize the increment of the resistance and the formation of a sharp peak in correspondence of the resonance frequency, where the contribution of the imaginary part goes to zero.

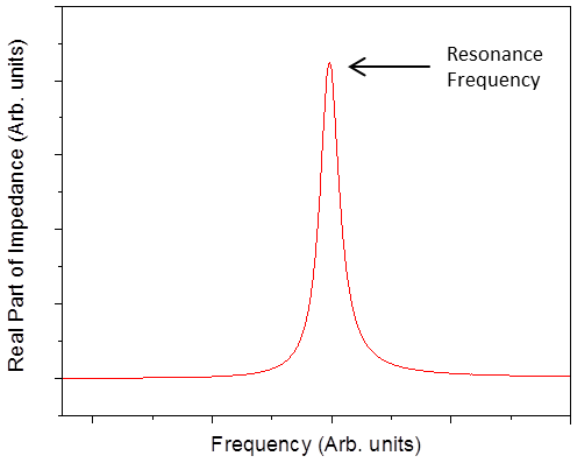

Figure 2.16 : Real part of impedance as a function of the frequency.

References

[1] B. D. Cullity and C. D. Graham, *Introduction to Magnetic Materials*, Second Ed. Wiley-IEEE Press, 2011.

[2] S. Chikazumi, *Physics of Ferromagnetism*. Oxford University Press, 2009.

[3] X. Batlle and A. Labarta, “Finite-size effects in fine particles: magnetic and transport properties,” *J. Phys. D. Appl. Phys.*, vol. 35, no. 6, pp. R15–R42, Mar. 2002.

[4] G. C. Papaefthymiou, “Nanoparticle magnetism,” *Nano Today*, vol. 4, no. 5, pp. 438–447, Oct. 2009.

[5] D. Peddis, C. Cannas, A. Musinu, and G. Piccaluga, “Magnetism in Nanoparticles: Beyond the Effect of Particle Size,” *Chem. - A Eur. J.*, vol. 15, no. 32, pp. 7822–7829, Aug. 2009.

[6] J. L. Dormann, D. Fiorani, and E. Tronc, “Magnetic Relaxation in Fine-Particle Systems,” in *Advances in Chemical Physics, Volume 98*, John Wiley & Sons, Inc., 2007.

[7] J. Frenkel and J. Doefman, “Spontaneous and Induced Magnetisation in Ferromagnetic Bodies.,” *Nature*, vol. 126, no. 3173, pp. 274–275, Aug. 1930.

[8] C. Kittel, “Theory of the Structure of Ferromagnetic Domains in Films and Small Particles,” *Phys. Rev.*, vol. 70, no. 11–12, pp. 965–971, Dec. 1946.

[9] D. L. Leslie-Pelecky and R. D. Rieke, “Magnetic Properties of Nanostructured Materials,” *Chem. Mater.*, vol. 8, no. 8, pp. 1770–1783, Jan. 1996.

[10] E. C. Stoner and E. P. Wohlfarth, “A Mechanism of Magnetic Hysteresis in Heterogeneous Alloys,” *Philos. Trans. R. Soc. A Math. Phys. Eng. Sci.*,

vol. 240, no. 826, pp. 599–642, May 1948.

[11] M. Knobel, W. C. Nunes, L. M. Socolovsky, E. De Biasi, J. M. Vargas, and J. C. Denardin, “Superparamagnetism and Other Magnetic Features in Granular Materials: A Review on Ideal and Real Systems,” *J. Nanosci. Nanotechnol.*, vol. 8, no. 6, pp. 2836–2857, Apr. 2008.

[12] C. P. Bean and J. D. Livingston, “Superparamagnetism,” *J. Appl. Phys.*, vol. 30, no. 4, p. S120, 1959.

[13] D. Li, Z. Han, J. G. Zheng, X. L. Wang, D. Y. Geng, J. Li, and Z. D. Zhang, “Spin canting and spin-flop transition in antiferromagnetic Cr[sub 2]O[sub 3] nanocrystals,” *J. Appl. Phys.*, vol. 106, no. 5, p. 53913, Sep. 2009.

[14] X. Batlle, X. Obradors, M. Medarde, J. Rodríguez-Carvajal, M. Pernet, and M. Vallet-Regí, “Surface spin canting in BaFe12O19 fine particles,” *J. Magn. Magn. Mater.*, vol. 124, no. 1–2, pp. 228–238, Jun. 1993.

[15] C. J. Serna, F. Bødker, S. Mørup, M. P. Morales, F. Sandiumenge, and S. Veintemillas-Verdaguer, “Spin frustration in maghemite nanoparticles,” *Solid State Commun.*, vol. 118, no. 9, pp. 437–440, May 2001.

[16] E. Winkler, R. D. Zysler, M. V. Mansilla, and D. Fiorani, “Surface anisotropy effects in NiO nanoparticles,” *Phys. Rev. B*, vol. 72, no. 13, p. 132409, Oct. 2005.

[17] R. H. Kodama, S. A. Makhlouf, and A. E. Berkowitz, “Finite Size Effects in Antiferromagnetic NiO Nanoparticles,” *Phys. Rev. Lett.*, vol. 79, no. 7, pp. 1393–1396, Aug. 1997.

[18] R. H. Kodama, A. E. Berkowitz, E. J. McNiff, Jr., and S. Foner, “Surface Spin Disorder in NiFe 2 O 4 Nanoparticles,” *Phys. Rev. Lett.*, vol. 77, no. 2, pp. 394–397, Jul. 1996.

[19] B. Martínez, X. Obradors, L. Balcells, A. Rouanet, and C. Monty, “Low Temperature Surface Spin-Glass Transition in γ- Fe2O3 Nanoparticles,” *Phys. Rev. Lett.*, vol. 80, no. 1, pp. 181–184, Jan. 1998.

[20] H. Kachkachi, M. Noguès, E. Tronc, and D. A. Garanin, “Finite-size versus surface effects in nanoparticles,” *J. Magn. Magn. Mater.*, vol. 221, no. 1–2, pp. 158–163, Nov. 2000.

[21] D. A. Dimitrov and G. M. Wysin, “Effects of surface anisotropy on hysteresis in fine magnetic particles,” *Phys. Rev. B*, vol. 50, no. 5, pp. 3077–3084, Aug. 1994.

[22] R. N. Bhowmik and R. Ranganathan, “Enhancement of surface magnetization in antiferromagnetic nanoparticles,” *Solid State Commun.*, vol. 141, no. 7, pp. 365–368, Feb. 2007.

[23] M. Ghosh, K. Biswas, A. Sundaresan, and C. N. R. Rao, “MnO and NiO nanoparticles: synthesis and magnetic properties,” *J. Mater. Chem.*, vol. 16, no. 1, pp. 106–111, Dec. 2006.

[24] J. M. Wesselinowa, “Size and anisotropy effects on magnetic properties of antiferromagnetic nanoparticles,” *J. Magn. Magn. Mater.*, vol. 322, no. 2, pp. 234–237, Jan. 2010.

[25] S. Shtrikman and E. P. Wohlfarth, “The theory of the Vogel-Fulcher law of spin glasses,” *Phys. Lett. A*, vol. 85, no. 8–9, pp. 467–470, Oct. 1981.

[26] M. Knobel, W. C. Nunes, A. L. Brandl, J. M. Vargas, L. M. Socolovsky, and D. Zanchet, “Interaction effects in magnetic granular systems,” *Phys. B Condens. Matter*, vol. 354, no. 1–4, pp. 80–87, Dec. 2004.

[27] J. . Dormann, D. Fiorani, and E. Tronc, “On the models for interparticle interactions in nanoparticle assemblies: comparison with experimental results,” *J. Magn. Magn. Mater.*, vol. 202, no. 1, pp. 251–267, Jun.

1999.

[28] J. L. Dormann, L. Bessais, and D. Fiorani, “A dynamic study of small interacting particles: superparamagnetic model and spin-glass laws,” *J. Phys. C Solid State Phys.*, vol. 21, no. 10, pp. 2015–2034, Apr. 1988.

[29] W. Luo, S. R. Nagel, T. F. Rosenbaum, and R. E. Rosensweig, “Dipole interactions with random anisotropy in a frozen ferrofluid,” *Phys. Rev. Lett.*, vol. 67, no. 19, pp. 2721–2724, Nov. 1991.

[30] M. Sasaki, P. E. Jönsson, H. Takayama, and P. Nordblad, “Comment on ‘Memory Effects in an Interacting Magnetic Nanoparticle System,’” *Phys. Rev. Lett.*, vol. 93, no. 13, p. 139701, Sep. 2004.

[31] S. Mørup and E. Tronc, “Superparamagnetic relaxation of weakly interacting particles,” *Phys. Rev. Lett.*, vol. 72, no. 20, pp. 3278–3281, May 1994.

[32] D. Kechrakos and K. N. Trohidou, “Magnetic properties of dipolar interacting single-domain particles,” *Phys. Rev. B*, vol. 58, no. 18, pp. 12169–12177, Nov. 1998.

[33] K. Trohidou and M. Vasilakaki, “Magnetic Behaviour of Core/Shell Nanoparticle Assemblies: Interparticle Interactions Effects,” *K. Trohidou, M. Vasilakaki. 2010. Magn. Behav. Core/Shell Nanoparticle Assem. Interparticle Interact. Eff. Acta Phys. Pol. A 117 374-378.*, vol. 2, no. 117, pp. 374–378, Feb. 2010.

[34] S. Gangopadhyay, G. C. Hadjipanayis, C. M. Sorensen, and K. J. Klabunde, “Effect of particle size and surface chemistry on the interactions among fine metallic particles,” *IEEE Trans. Magn.*, vol. 29, no. 6, pp. 2619–2621, 1993.

[35] A. Lyberatos and E. P. Wohlfarth, “A monte carlo simulation of the

dependence of the coercive force of a fine particle assembly on the volume packing factor," *J. Magn. Magn. Mater.*, vol. 59, no. 1–2, pp. L1–L4, May 1986.

[36] D. Kechrakos, K. N. Trohidou, and M. Vasilakaki, "Magnetic properties of dense nanoparticle arrays with core/shell morphology," *J. Magn. Magn. Mater.*, vol. 316, no. 2, pp. e291–e294, Sep. 2007.

[37] J. M. D. Coey, *Magnetism and Magnetic Materials*. 2010.

[38] A. Skumiel, M. Kaczmarek-Klinowska, M. Timko, M. Molcan, and M. Rajnak, "Evaluation of power heat losses in multidomain iron particles under the influence of AC magnetic field in RF range," *Int. J. Thermophys.*, vol. 34, no. 4, pp. 655–666, 2013.

[39] G. Poggi, *Esperimenti di elettricità e magnetismo*, vol. 63. .

Chapter 3

Synthesis and characterization of ferrite nanoparticles

3.1 Synthetic approaches to magnetic nanoparticles

Magnetic nanoparticles can be exploited for a large range of application, from medical therapy to electronic devices. [1] Accordingly, in the last decades, a large number of different synthetic approaches were developed to obtain nanoparticles with controlled size, composition and shapes. Considering their dimension which falls between that of discrete molecules and of bulk materials, nanoparticles can be obtained by two different methodologies:

1. the *top-down* approach:
   starting from bulk materials it is possible to decrease the particle size and obtain nanostructures by milling, repeated quenching or lithography. The advantage of this technique lies in the possibility to produce a large amount of nanostructured material with a very cheap approach. On the other hand, top-down approach suffers from some drawback; for example, in the case of ball milling it is difficult to obtain

a fine control on size and shape, significant amount of impurities coming from the milling medium often occur in the final nanomaterials and the crystallinity of the powder is often low. Conversely, lithographic techniques although very useful to prepare controlled high density nanostructures over large surfaces areas, are often slow, expensive, and cannot be employed for the large scale industrial production of powders.

2. the *bottom-up* approach:
   with this approach nanostructure are obtained by assembling the constituent atoms or molecules. It is a chemical approach which offers the unique advantage of providing an extremely fine control on size, composition and shape by simply varying the nature of the precursors or the various parameters involved in the selected synthetic strategies. Despite of these advantages, often the production of large amount of nanomaterials by chemical synthesis may be problematic due to the difficult in the scalability of the process and/or the cost of most of the chemical techniques.

The fundamental requirement of a fine control of size and composition combined to the necessity of producing large amount of nanomaterials at an economically sustainable and competitive cost, which characterize our research, makes the *bottom-up* approach the most suitable one. Therefore, in the following, a brief overview of the most common wet chemical synthetic strategies and techniques developed to date, is provided.[1]–[5]

3.2 Chemical synthesis of nanoparticles

3.2.1 Microemulsion synthesis

Microemulsions are thermodynamically stable isotropic, two phases mixtures composed by water and an organic solvent, in different proportion, stabilized by surfactants. When the aqueous phase is the majority one they are termed Oil in Water (O/W) emulsion; while in the opposite case they are called Water in Oil (W/O). W/O microemulsions can be used to synthesize nanoparticles using the water micelles as nanoreactors and carrying out the reaction in the confined volume of the aqueous media. The reaction is achieved by mixing two different W/O microemulsions, each one containing the reactants, as for example transition metal salts and a base or a reducing agent. As the micelles collide and coalesce, the reactants mix and the nanoparticles formation takes place [6][7]. Composition can be easily tuned by changing the metal transition precursors; size and shape can be adjusted by varying water to oil ratio, the type of surfactant and its nature and temperature [8]. Despite the technique provides high quality nanostructures with good crystallinity and narrow size distribution, the final nanoparticle yield is very low and the process can hardly be scaled up due to inherent production costs and residual waste disposal.

3.2.2 Hydrothermal synthesis

The preparation of much larger amount of nanomaterial can be obtained by the hydrothermal synthetic approach. This process exploits high temperature reaction to produce nanoparticles with high crystallinity degree and fine controlled sizes through heating a solution of metal salt precursors in an

autoclave, reaching high pressure, over the solvents boiling points. In these conditions, metal hydroxides, formed as intermediate, evolve in metal oxide nanoparticles [9]. Usually, the solvent used in hydrothermal synthesis is water, but other hydrophilic solvents, as for example ethylene glycol, can be used as well to increase the reaction temperature; in this case, the reaction is called solvothermal synthesis [10]. In both cases, transition metal salts concentrations, solvent, temperature and reaction time can be tuned to obtain the desired structure [11]. However, since this technique is characterized by slow reaction kinetics, the reaction time is usually long, leading to high polydispersity of the resulting nanosystem.

3.2.3 Polyol synthesis

An alternative approach to synthesize nanoparticles with high crystallinity is the polyol strategy. In this method, the use of polyols (e.g. polyethylene glycol) as solvent offers the possibility of both dissolving inorganic salt and carrying out the reaction at high temperature, thanks to higher boiling points. [12] Furthermore, polyols may act also as reducing agents and as stabilizers, in order to control particle growth and prevent interparticle aggregation. In details, the metal salts precursors are dissolved in a polyol solvent and the reaction mixture is heated to the desired temperature (up to the boiling point of the polyol). During the heating process the metal precursors create an intermediate complex forming the nuclei, which then evolve in the crystal nanostructure. Precursor concentration, reaction time and temperature can be properly adjusted to tune final particle size and shape. [13]

3.2.4 Thermal decomposition synthesis

Extremely good control on the particles size, shape and composition can be obtained by thermal decomposition of metalorganic precursors (e.g. metal-acetylacetonate, metal-carbonyl, and others) in high boiling organic solvents. The synthesis takes place in the presence of surfactants (e.g., oleic acid and oleylamine) that act both as stabilizing agents for the obtained nanoparticles and as reagent for the formation of reaction intermediates in the synthetic process. Thermal decomposition of metal-organic precursors as metal-carbonyl starts from the metal in the zero-valent oxidation state and leads to the formation of metal nanoparticles that, after oxidation, transform into high quality monodisperse metal oxides. [14] On the other hand, decomposition of precursors with cationic metal complexes, as metal-acetylacetonate, directly leads to metal oxides nanoparticles. [15] In both cases, the precursor concentration, the metal-to-surfactant ratio, the type of surfactant and solvent play a relevant role for the size and shape tuning. Moreover, the reaction temperature and time, the heating rate and the aging period may also be used to precisely control the size, morphology and crystal phase. [16], [17]

3.2.5 Co-precipitation synthesis

Co-precipitation is a facile and easy scalable method to synthesize magnetic nanoparticles. Starting from aqueous solutions of inorganic salts, precipitation and crystallization of nanoparticles occurs by addition of a base or of a reducing agent. Usually, in order to preserve the precursor oxidation state, reaction is carried out under inert atmosphere. Temperature can be varied

from room temperature to water boiling point. [18] Size, shape and composition of the nanoparticles are tuned by varying the precursors (e.g. chlorides, nitrates, sulphates), [15] the precursors concentrations, [19] the type of base, [20] the reaction temperature, [21] the pH values and ionic strength of the aqueous media [22], [23] and eventually through the presence of surfactants. However, nanoparticles synthesized by co-precipitation are characterized by high polydispersity and poor crystallinity. Thus, subsequent annealing processes are necessary in order to achieve satisfying magnetic properties.

3.3 Spinel ferrites

As described in the Introduction, the target material chosen in this Thesis is Manganese, Zinc doped ferrite ($Mn_{1-x}Zn_xFe_2O_4$). This material, indeed, exhibits low eddy current loss, good thermal and chemical stability, high magnetic permeability and low coercivity. [24] Thanks to these properties it is largely used as micrometer-sized grains, for the production of inductors and transformers, used in many electronic devices. As described before, the reduction of the material to the nanoscale can improve the magnetic and then the electronic properties. $Mn_{1-x}Zn_xFe_2O_4$ has a cubic spinel structure; this is a typical crystallographic structure common with some ceramic compounds with general formula AB_2O_4, where A and B are transition metals cation in a divalent and trivalent oxidation state, respectively. The spinel structure belongs to cubic space group $Fd\overline{3}m$ and can be described according to the atomic arrangement shown in Figure 3.1, where the trivalent and the divalent ions occupy 16 of 32 octahedral (*Oh*) and 8 of 64 tetrahedral (*Td*) crystallographic cavities generated by 32 oxygen atoms, which form a face-centred cubic (*fcc*) lattice.

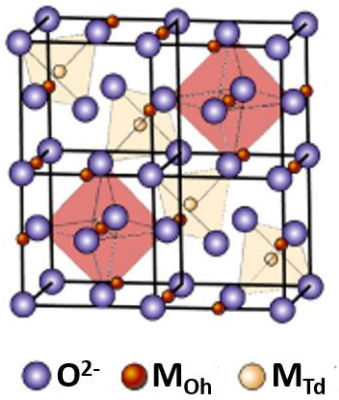

Figure 3.1 : Unit cell of a cubic spinel structure.

Actually, in many cases a different distribution of A and B ions among tetrahedral and octahedral cavities are observed. The general formula for a spinel must then be written as: $(A_{1-i}B_i)_T[A_iB_{2-i}]_OO_4$, where the () and [] brackets denote the tetrahedral, *Td*, and octahedral, *Oh*, sites respectively and *i* is the inversion parameter, which can vary from 0 to 1. Accordingly, depending on the metal ion distribution, spinel structures are classified as [24]:

- *normal spinel*: all the trivalent ions (B) occupy *Oh* sites while all the divalent ions (A) are placed in the *Td* cavities; $(A^{2+})[B_2^{3+}]O_4$
- *inverse spinel*: trivalent ions (B) occupy 1/4 of *Td* sites and 1/8 of the *Oh* ones while divalent ions (A) are placed in the remaining *Oh* cavities; $(B^{3+})[A^{2+}B^{3+}]O_4$
- *partially inverted spinel*: both trivalent (B) and divalent (A) ions occupy *Oh* and *Td* sites; $(A_{1-i}B_i)[A_iB_{2-i}]O_4$

An useful model to predict the spinel structure inversion degree is by referring to the Crystal Field Stabilisation Energy (*CFSE*), which describes the stabilization of a given transition metal ion when it is placed in a crystal field generated by external ligands. For a given geometry, the cation will occupy the sites with the higher *stabilization energy*. Hence, if the trivalent element has higher *CFSE* value in *Oh* site than the divalent cation, a normal spinel is expected. Conversely, an inverse spinel is formed when the divalent cation has higher *CFSE* value in *Oh* cavities than the trivalent one. One of the most common class of materials sharing the spinel structure are ferrites, where the trivalent cation is the iron (Fe^{3+}) and the divalent element can be Fe^{2+}, Co^{2+}, Mn^{2+}, Zn^{2+} , Cu^{2+}, Ni^{2+} and others. The most important member of the family of ferrites is by no doubts magnetite, Fe_3O_4, a naturally occurring black matt mineral with metallic aspect. From a crystallographic point of view, magnetite has an inverse spinel structure, $(Fe^{3+})[Fe^{2+}Fe^{3+}]O_4$, due to the higher *CFSE* value

of Fe^{2+} in *Oh* sites with respect to Fe^{3+} [25]. An example of normal spinel ferrite is the stoichiometric Zn doped ferrite $(Zn^{2+})[Fe_2^{3+}]$. Indeed, the *CFSE* value of zinc for *Oh* site is lower than for the *Td* one leading to the formation of a normal spinel ferrite. [24]. Instead, among partially inverted spinel structure, cobalt doped ferrite is one of the most debated material: since high spin Fe^{3+} ions have lower *CFSE* in *Oh* than Co^{2+}, the model predicts $CoFe_2O_4$ would assume an inverse spinel structure; conversely, several experiments demonstrated that $CoFe_2O_4$ is a partially inverted spinel structure with cobalt atoms predominantly in the *Oh* sites (high degree of inversion). [26] In particular, inversion parameters ranging between i = 0.68 - 0.80 have been reported. [27] [28] Therefore, as reported in the literature, most mixed ferrites, such as cobalt and manganese ferrite, exhibit only partially inverted cation distribution. [27] The inversion degree of a stoichiometric manganese ferrite is i =0.2 and thus is described as $(Mn_{0.8}^{2+}Fe_{0.2}^{3+})[Mn_{0.2}^{2+}Fe_{1.8}^{3+}]O_4$. Considering the higher affinity of zinc for tetrahedral sites, a manganese, zinc doped ferrite, normally assumes *partially inverted spinel* structure and can be written as $(Zn_x^{2+}Mn_y^{2+}Fe_{1-x-y}^{3+})[Mn_{1-x-y}^{2+}Fe_{1+x+y}^{3+}]O_4$. [24] These cases show how octahedral and tetrahedral sites of ferrites can be filled by different transition metal ions with very different atomic radius (e.g., Mn^{2+} 0.83 Å, Fe^{2+} 0.78 Å, Co^{2+} 0.75 Å, Zn^{2+} 0.74 Å, Ni^{2+} 0.69 Å). [29] The fitting of so many different guest ions into the structure is allowed by the flexibility of the oxygen framework, which can expand or contract to accommodate cations with different sizes. Cation substitution is accompanied by changes in unit cell edge length. [30] Since the physical properties of ferrites are strictly related to the distribution of cations between *Oh* and *Td* sites in the spinel structure, the control of cation distribution provides a mean to tailor their physical properties, and particularly the magnetic ones. From the magnetic point of view, ferrites are ferrimagnetic (FiM). In fact, as schematized in Scheme 3.1, the magnetic moment of the cations are parallel (ferromagnetic coupling) to those placed in sites with same

geometry (e.g., *Oh-Oh and Td-Td*) and antiparallel (antiferromagnetic coupling) to those of cations in cavities with different geometry (e.g., *Oh-Td*).

Scheme 3.1 : Scheme of the spin coupling in different spinel structures. The spin-only magnetic moment for Fe^{3+}, Fe^{2+}, Mn^{2+} and Zn^{2+} are 5, 4, 5 and 0 Bohr magneton (μB), respectively.

Normal Spinel Structure

$(Zn^{2+})[Fe^{3+}Fe^{3+}]O_4$

0 ↓ ↑ 0

Inverse Spinel Structure

$(Fe^{3+})[Fe^{2+}Fe^{3+}]O_4$

↓ ↑ ↑ 0

Partially Inverted Spinel Structure

$(Zn_x^{2+}Mn_y^{2+}Fe_{1-x-y}^{3+})[Mn_{1-x-y}^{2+}Fe_{1+x+y}^{3+}]O_4$

0 ↓ ↓ ↑ ↑ 0

Such orientation originates two sublattices of parallel magnetic moments, for *Td* and *Oh* sites respectively, which are antiferromagnetically coupled. However, in most of the cases, the magnetic moments of *Td* and *Oh* sublattices are not completely compensated and this leads to a non-zero net magnetic moment of the material. Thus, even if sharing the same crystallographic and magnetic structures, the magnetic properties of spinel ferrites are strictly related to the nature of the divalent ions and to their distribution among the different crystallographic sites. This means that their magnetic properties can

be drastically modified by simply replacing, either completely or partially, the metal ions or by modifying the inversion degree without affecting the crystal structure, a characteristic which makes this class of material extremely appealing for a large number of applications.

3.4 Synthesis of doped iron oxide ferrite nanoparticles

The target of this work was to synthesize high crystalline Manganese Zinc doped ferrite nanoparticles, with a reaction facile, cheap and easily scalable to the industrial production. As described in Section 3.2, considering the expensive costs of high boiling solvents and metal-organic precursors, the low yield of microemulsion synthesis and the long reaction time of hydrothermal one, we decided to focus on the co-precipitation method, trying to optimize the technique with the aim to obtain high crystallinity nanomaterials. Moreover, the optimization of this method was also aimed at obtaining a large amount of Mn, Zn doped ferrite nanoparticles with the desired properties. Basically, the reaction consists in the precipitation of transition metal hydroxides after the addition of ammonium hydroxide and the following dehydration as shown in Scheme 3.2:

Scheme 3.2 : Precipitation reaction of transition metal ions in basic media.

$$Fe^{3+}_{(aq)} + 3OH^{-}_{(aq)} \longrightarrow Fe(OH)_{3\,(S)}$$

$$Fe^{2+}_{(aq)} + 2OH^{-}_{(aq)} \longrightarrow Fe(OH)_{2\,(S)}$$

$$Mn^{2+}_{(aq)} + 2OH^{-}_{(aq)} \longrightarrow Mn(OH)_{2\,(S)}$$

$$Zn^{2+}_{(aq)} + 2OH^{-}_{(aq)} \longrightarrow Zn(OH)_{2\,(S)}$$

$$(1\text{-}x)Mn(OH)_2 + xZn(OH)_2 + 2Fe(OH)_3 \longrightarrow Mn_{1-x}Zn_x(OH)_{8-2n}O_n + nH_2O \longrightarrow$$
$$\longrightarrow Mn_{1-x}Zn_xFe_2O_4 + 4H_2O$$

The last process is driven by the increase of temperature and consists in a transformation of the hydroxides first in mixed oxo-hydroxides and, then, after losing four molecules of water, in the desired cubic spinel structure.

It should be noted that precipitation of the metal cations into the solid hydroxides form is mainly driven by the pH values of the solution. Indeed, this process occurs at different pH as function of the transition metal, as shown in Table 3.1. [31][32][33]

Table 3.1 : pH values for the precipitation of metal transition hydroxides.

Transition metal Ion	Oxidation state	Starting precipitation pH	Complete precipitation pH
Iron	3+	5.0	13.0
Iron	2+	11.5	12.5
Manganese	2+	11.5	12.5
Zinc	2+	8.5	11.5

A detailed discussion of this synthetic methodology is provided in the following section.

3.4.1 Experimental procedure

Manganese Zinc doped ferrite nanoparticles were synthesized through a co-precipitation method. This chemical approach provides a good control on crystallinity and composition of the as-synthesized product. Moreover, in view of a possible application of the material, this process can be easily scaled up to the industrial production level, starting materials and the reaction costs are sustainable and yields are quasi-quantitative. Despite of the large amount of scientific report in the literature concerning co-precipitation, most of them produce nanoparticles with a low crystallinity degree and, to obtain good

performance material, annealing process at high temperature is often necessary to improve the crystal quality. However, the heating treatment needed for annealing process implies also the growth of the grain, leading to the loss of the nanostructure and consequently of the associated physical properties. One of the goals of this Thesis is the improvement of the co-precipitation technique in order to produce high crystallinity nanoparticles in a single step, avoiding any annealing process. In our case we selected as reactants the metal chlorides. This choice was made considering the low cost of transition metal salts, the easily storage of the reactants and the formation, in the residual waste, of ammonium chloride salt that is not-hazardous and cheap for disposal. On the other hand, the use of sulfates as reagents, which is an alternative route that can be found in the literature, [34] was discarded since they are a little more expensive than chlorides and may be dangerous because of the generation of SO_x gases at high temperature.

In a typical synthesis, molar ratio of starting metal transition chlorides was quantitatively adjusted according to the final desired stoichiometry. In a first step, a solution of Fe^{3+} was prepared dissolving 2 equivalent (eq.) of $FeCl_3$ in demineralized water. The pH was adjusted to 8 using a solution of NH_4OH 33% in weight, in order to obtain the complete precipitation of ferric hydroxide as a brown slurry. The precipitated was collected through filtration on Buchner funnel and washed several times with demineralized water. Meanwhile, Mn^{2+} as $MnCl_2$ and Zn^{2+} as $ZnCl_2$ were solubilized in N_2 purged demineralized water; to this solution the $Fe(OH)_3$ was quantitatively added and the pH was adjusted to 12 by using the NH_4OH solution at 33%. The resulting dark brown reaction mixture, composed by transition metal hydroxides was heated to reflux, under N_2 flow and magnetic stirring, and the color turned black after ten minutes. In order to complete the reaction, increase the crystallinity and avoid the formation of satellite phases, reaction mixture was kept at reflux for 2 hours.

Then, the black suspension was cooled to room temperature and the black precipitate was collected using a permanent magnet. The magnetic nanoparticles were washed several times with water, ethanol and acetone and dried overnight at 80 °C.

The three key points of this synthesis are the precipitation of the 3 metal hydroxides, i.e. ferric hydroxide, manganese hydroxide and zinc hydroxide, which will be discussed in detail in the further sections.

3.4.1.1 Precipitation of the ferric hydroxide

Ferric hydroxide precipitation starts at pH = 5, as reported in Table 3.1, and becomes quantitative at higher pH. When ferric chloride is dissolved in water, as other transition metal ions, a large variety of H_2O and OH^- complexes can be formed: in water ferric ions form aquo-complexes with six water coordinated molecules. The electrostatic field of the tri-positive metal ion enhances the acidic nature of the coordinated H_2O molecules:

$$Fe(H_2O)_6^{3+} \rightleftharpoons Fe(H_2O)_5(OH)^{2+} + H^+$$

This is the first of a series of similar reactions, each one having a successively smaller equilibrium constant:

$$Fe(H_2O)_5(OH)^{2+} \rightleftharpoons Fe(H_2O)_4(OH)_2^+ \rightleftharpoons Fe(H_2O)_3(OH)_3^o \rightleftharpoons Fe(H_2O)_2(OH)_4^-$$

This acidic n-hydroxy-n-aquo species are responsible of the low pH value of ferric solutions (approximately pH = 2). When a basic solution is added a large variety of hydroxo-complexes, of which the insoluble $Fe(OH)_3$ can be

considered a member, forms, each one characterized by its stability constant. (Table 3.2):

Table 3.2 : Ferric-hydroxo-complexes and their stability constants. (*for the insoluble ferric hydroxide it is reported the inverse of the solubility constant)

Ferric ion complexes	Stability constant
$Fe^{3+} + 3\ OH^{-} \rightarrow Fe(OH)_3(s)$	$1/K_s$ *= 10^{38}
$Fe^{3+} + H_2O \rightarrow FeOH^{2+} + H^{+}$	$K = 10^{-2.2}$
$Fe^{3+} + 2H_2O \rightarrow Fe(OH)_2^{+} + 2H^{+}$	$K = 10^{-6.7}$
$Fe^{3+} + 4H_2O \rightarrow Fe(OH)_4^{-} + 4H^{+}$	$K = 10^{-23}$
$2Fe^{3+} + 2H_2O \rightarrow Fe_2(OH)_2^{4+} + 2H^{+}$	$K = 10^{-2.8}$

Since the hydroxo-complex formation involves five equilibria, a complete description of this system requires the simultaneous solution of five equations. However, with some approximations, it is possible to construct a log-concentration vs. pH plot diagram, as shown in Figure 3.2.

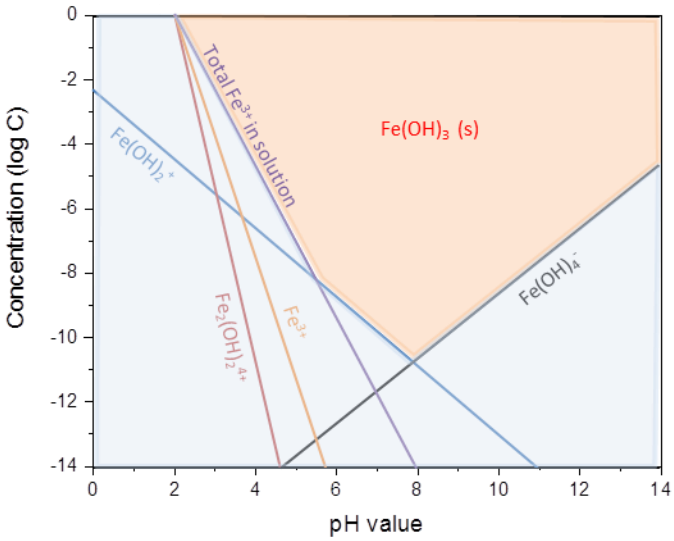

Figure 3.2 : Iron hydroxide complexes concentration as a function of pH.

At any given pH, the equilibrium with solid $Fe(OH)_3$ is controlled by the ionic species having the highest concentration. The corresponding lines in the plot therefore delineate the region, indicated in orange, at which the solid exists; conversely, the light blue region indicates the water soluble region. Thus, it is possible to appreciate how the quasi-complete precipitation of iron hydroxide occurs at pH value close to 8. At lower pH the formation of the highly soluble $Fe(OH)_2^+$ and $Fe_2(OH)_2^{4+}$ complexes occurs, while at higher pH values the formation of the water soluble complex $Fe(OH)_4^-$ results. [35] On this basis, in order to quantitatively precipitate the $Fe(OH)_3$, it is appropriate to work with a pH value close to 8. Thus, ammonium hydroxide solution was chosen for the precipitation step.

3.4.1.2 Precipitation of the manganese hydroxide

As described before, in order to obtain a stoichiometric Mn, Zn ferrite and promote the ferrite crystallization, the precipitation of Fe^{3+} was carried out separately. Indeed, as observed by Rath et al. [33], when the three metals are precipitated simultaneously, an incomplete precipitation of manganese and zinc may occurs. This phenomenon can be attributed to the partial solubilization of $Mn(OH)_2$ driven by the presence of high amount of ammonium and chloride ions in solution:

$$Mn(OH)_{2(s)} + 4NH_4^+{}_{(Aq)} + 2Cl^-{}_{(Aq)} \rightleftharpoons [Mn(NH_3)_4(Cl)_2]_{(Aq)} + 2H_2O$$

Therefore, in order to prevent the solubilization of $Mn(OH)_2$ and facilitate the formation of a stoichiometric ferrite, it is essential to decrease the chloride content in the reaction system. The correctness of this approach was verified by one attempt performed simultaneously precipitating the manganese and iron hydroxides. The XRD pattern of the resulting powder is shown in Figure 3.3. Although in the pattern all the peaks corresponding to the cubic structure of spinel ferrite can be observed, they are very broad indicating a very low crystallinity degree. This result can be ascribed to the oxidation of Mn^{2+} which strongly decreases the divalent ions amount in solution. Indeed, as described in Section 3.3, the presence of divalent metal cations is a fundamental requirement for the crystallization of the cubic spinel structure.

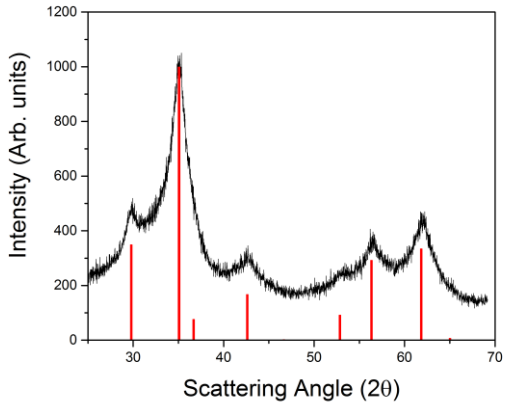

Figure 3.3 : XRD pattern of a Manganese doped ferrite obtained by simultaneous precipitation of Mn and Fe hydroxides. The red lines correspond to the reference pattern for a cubic spinel structure Fd-3m.

Moreover, as is the case of iron hydroxide, the presence of different manganese hydroxo-complexes must be taken into account, as schematically shown in Figure 3.4.

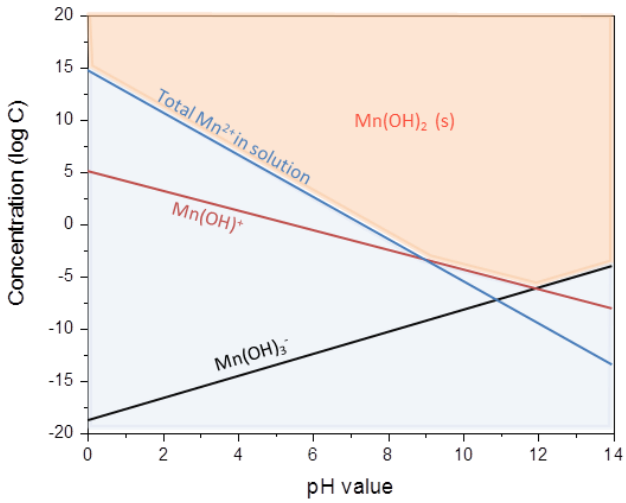

Figure 3.4 : Manganese hydroxide complexes concentration as a function of pH.

In order to completely precipitate manganese hydroxide, it is necessary to reach a pH value close to 12. Moreover, manganese ions have a higher instability towards oxidation in water than the iron and zinc ones. In order to avoid the oxidation of Mn^{2+} to Mn^{4+} ($E^0_{Mn(II)/MnO2}$= - 1,23 eV)

$$2Mn^{2+} + O_2 + 2H_2O \longrightarrow 2MnO_2 + 4H^+$$

driven by the oxygen dissolved in water ($E^0_{O2/H2O}$= 1,23 eV), it is necessary to use N_2 purged demineralized water. Indeed, once the reaction is carried out without purged water, different phases from the cubic spinel structure form, as shown in Figure 3.5 where the XRD pattern of the powder obtained operating in this way is shown. The analysis on the powder XRD allows us to identify the phases as Goethite (FeOOH, orthorhombic *Pbnm, ICCP database PDF 01-0401*), Manganite ($Mn_2O_3 \bullet H_2O$, orthorhombic *Pnnm, ICCP database PDF 08-0016*) and HydroHeterolite ($Zn_2Mn_4O_8 \bullet H_2O$, tetragonal *I41/amd, ICCP database PDF 09-0459*).

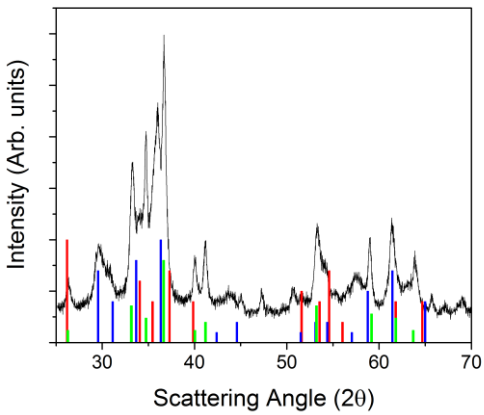

Figure 3.5 : Powder XRD pattern of not water degassed synthesis. The bars correspond to the reference patterns of manganite (red), hydroheterolite (blue) and goethite (green).

3.4.1.3 Precipitation of the zinc hydroxide

After quantitative precipitation of iron hydroxide is obtained, the product is filtrated on a Buchner. As described above, this is a fundamental step because, as for the case of Manganese, the large amount of chloride at high pH in the reaction mixture could determine the formation, of zinc hydroxyl-chloride complexes:

$Zn(OH)_3Cl^{2-}$ $Zn(OH)_2Cl_2^{2-}$ $Zn(OH)Cl_3^{2-}$

The formation of these sub-products can decrease the zinc hydroxides availability for the further dehydration and crystallization steps, leading to a low quality crystalline product, as shown, for the case of Manganese, in Figure 3.4. Zinc hydroxide is also in equilibrium with mono-, tri- and tetra- hydroxide complexes, as shown in Figure 3.6.

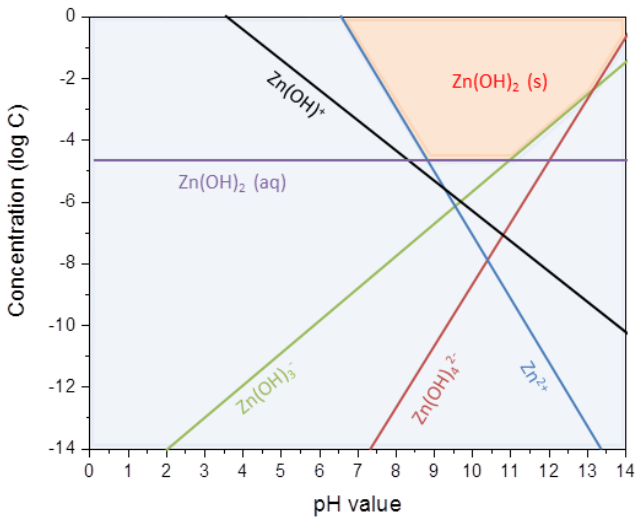

Figure 3.6 : Zinc hydroxide complexes concentration as a function of pH.

Moreover, in ammonium basic media, zinc availability can be decreased by the formation of di-, tri-, or tetra- amino complexes, depending on the pH value, as described in Figure 3.7. [36]

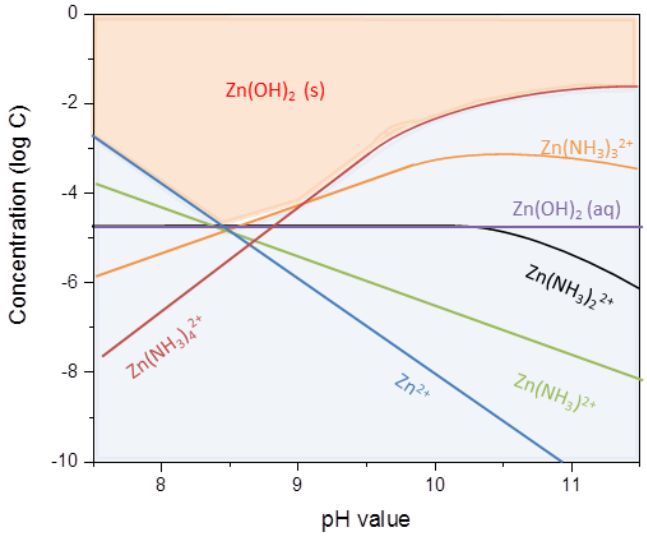

Figure 3.7 : Zinc ammonium complexes concentration as a function of pH.

From the above diagram it appears that in order to quantitatively precipitate zinc hydroxide, it is necessary to work with a pH value between 8.5 and 9.5. However, since the precipitation of manganese and zinc is carried on simultaneously, the pH value of 12 is selected to precipitate quantitatively the manganese. Indeed, although at this pH zinc is in the form of amino-complexes, on increasing temperature over 90 °C, these complexes become instable releasing ammonia in the reaction mixture:

$$Zn(NH_3)_x^{2+} \xrightarrow{\Delta} Zn(OH)_2 + xNH_3 \uparrow$$

The evaporation of ammonia decreases the pH value, leading to the formation of zinc hydroxide which immediately reacts with iron and manganese

hydroxides, forming the magnetic nanoparticles. The reaction mixture is then kept to reflux for two hours, in order to increase the product crystallinity. The synthetic strategy explained above allows us to produce magnetic nanoparticles with a quasi-quantitative yield. Moreover, attempts of carrying out the reaction in a 100 L reactor, currently under way, demonstrate the possibility of scaling-up the synthesis to industrial production without modifying neither the chemical nor the structural or physical properties of the final powder. Another important advantage provided by this synthesis is the high reproducibility. Indeed, the reaction was repeated more than 60 times, leading almost to the same product. This is shown in Figure 3.8 where a statistical analysis of two parameters extracted from the XRD powder, i.e. the lattice parameter and crystallite size, obtained over 60 different nanopowders, is shown.

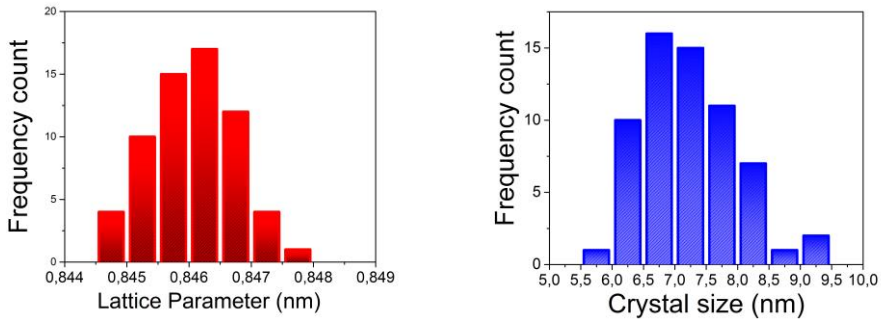

Figure 3.8 : Statistical analyses of lattice parameter (left) and crystallite size (right) for 60 samples obtained repeating the same synthesis.

The lattice parameter which can be taken as an indicator of the product stoichiometry, presents a main value of 0.8461 nm with a standard deviation value of $8x10^{-4}$ nm, while the crystallite size main value is 7.1 nm with polydispersity lower than 10 %, indicating the formation of almost the same

crystalline product in all the synthesis. In the following paragraph, it is reported the chemical, structural and magnetic characterization of one of the product, as representative of all the synthesized nanomaterials.

3.4.2 Characterization of the chemical, structural and physical properties

In order to verify the formation of crystalline Manganese, Zinc doped ferrite nanoparticles, powder X-Ray Diffraction (XRD) patterns were recorded (see Figure 3.9). The diffraction pattern shows the formation of a single crystallographic phase, and the peaks can be indexed as belonging to the cubic structure of spinel oxides (*JCPDS PDF #221086*). Crystal size, estimated by Sherrer's Equation as describe in the Chapter 6, was 7.6(5) nm. The lattice parameter, descriptive of divalent cation occupancy and of the ferrite stoichiometry, was estimated by Rietveld refinement (Chapter 6) and was 0.8467(2) nm. This value is in good agreement with that reported in the literature for $Mn_{0,6}Zn_{0,4}Fe_2O_4$ (0.8465 nm). [37] The composition of the nanoparticles was further confirmed by X-Ray fluorescence analysis which provided a Mn:Zn:Fe molar ratio equal to 1,5:1:5.

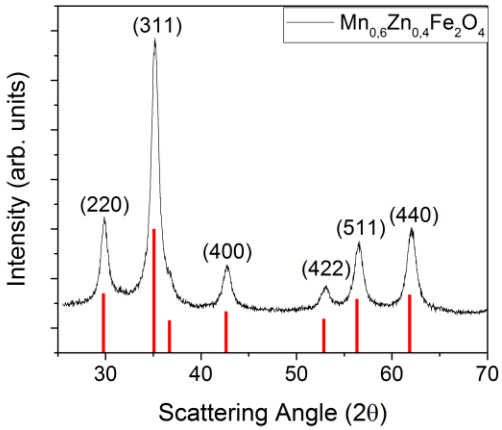

Figure 3.9 : XRD pattern of the $Mn_{0,6}Zn_{0,4}Fe_2O_4$ powder displaying the typical iron oxide cubic spinel structure Red lines refer to the reference pattern of a cubic spinel structure (PDF 74-2400); the corresponding *hkl* indexes are also reported .

The Transmission Electron Microscopy (TEM) images (Figure 3.10) were acquired in order to obtain information on morphology, size and size distribution of the nanoparticles. In particular, the mean particle diameter ($\bar{d}$) and standard deviation (σ) were obtained by calculating the number average by manually measuring the diameter length of >100 particles from TEM micrographs. Considering the high aggregation degree of the nanoparticles and the difficulty to perform a correct statistic on the images, mean particle diameter was estimated by measuring only the nanoparticles located at the aggregate edge. The main particles diameter, obtained with the synthetic approach described above, is 8(2) nm.

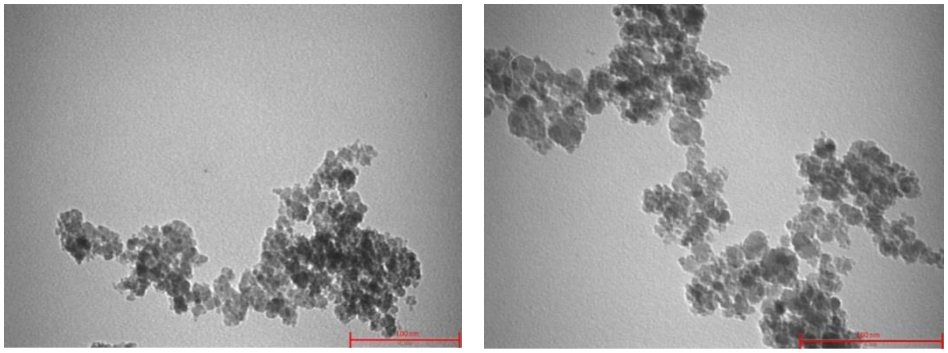

Figure 3.10 : TEM images of manganese zinc ferrite nanoparticles. The scale bar is 100 nm.

The static magnetic properties of the sample were investigated by standard magnetometric techniques, as discussed in Chapter 6. In particular, magnetic properties of the nanoparticles were measured on tightly randomly packed powder samples using a vibrating sample magnetometer (VSM). At first, the temperature dependence of the magnetization was investigated after zero field cooling (*ZFC*) and field cooling (*FC*) procedures (Chapter 6) in the presence of a 50 Oe of applied field (Figure 3.11).

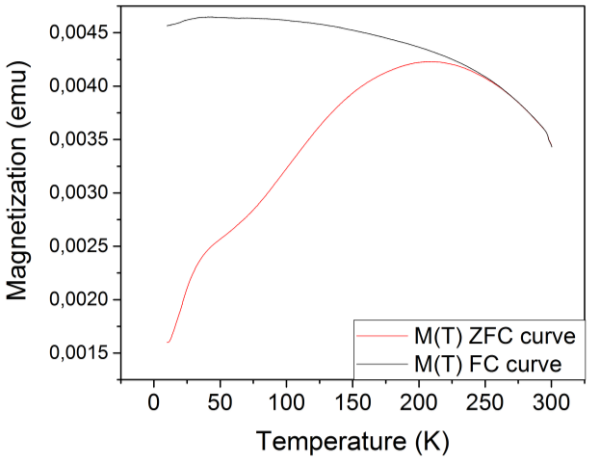

Figure 3.11 : Temperature dependence of the ZFC and FC magnetization curves recorded at 50 Oe. The red and blue continuous lines correspond to ZFC and FC, respectively

In particular, ZFC curves of Manganese, Zinc doped ferrite nanoparticles presented a maximum at a given temperature, T_{max}, close to 200 K. As a first approximation, T_{max} can be identified with the *blocking temperature*, T_B, of the system. This is a value higher than the 100 K commonly reported in the literature for weakly interacting Manganese, Zinc doped ferrite nanoparticles. [38] The shift to higher temperature can be ascribed to the high interaction existing between nanoparticles, enhanced by the absence of an organic surfactant on the particle surface.

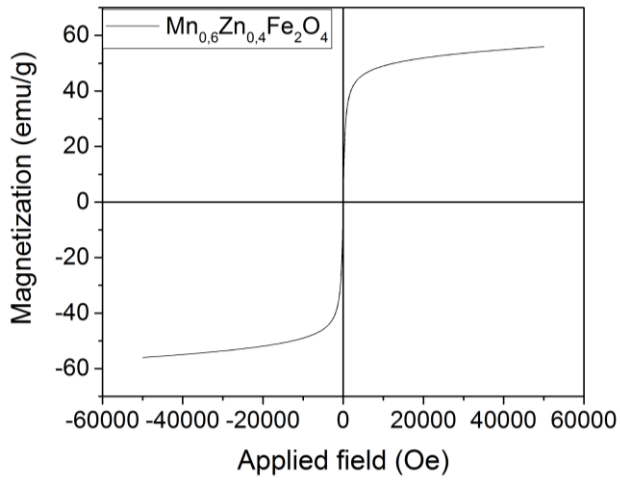

Figure 3.12 : Hysteresis loop of Manganese Zinc Ferrite recorded at 300 K.

The hysteresis loop, shown in Figure 3.12, was recorded at 300 K, applying an external field between -50000 and +50000 Oe on the pressed powder pellet. The saturation magnetization value, obtained by fitting the curve with a Langevin function, was 56 emu/g, comparable with the M_S value reported in the literature for nanoparticles of same composition, obtained by a similar synthetic strategy. [37] At room temperature no magnetic irreversibility was observed, at least within the resolution limit of the instrument (ca. 50 Oe, due to a spurious remnant field). Therefore, as indeed suggested by ZFC-FC curves too, the synthesized nanoparticles are in the superparamagnetic regime at

room temperature, a property which may determine the reduction of losses associated to the hysteretic behaviour. Once it was found the appropriate synthetic parameters to prepare high crystalline magnetic nanoparticles with controlled composition, the same approach was extended to the production of doped ferrite nanoparticles with a composition different from the $Mn_{0.6}Zn_{0.4}Fe_2O_4$ with the aim of exploring if at the nanoscale other compositions could have better magnetic properties for the desired application. In particular, it was investigated the role of zinc content by preparing a series of Manganese, Zinc doped ferrite nanoparticles of formula $Mn_{1-x}Zn_xFe_2O_4$, with different Mn : Zn metal ratio (x ranging from 0 to 0.5) and we tested the effect of introducing a small percentage of Ni^{2+} in the ferrite lattice. In the latter case, the Mn content was kept constant and equal to 0.6 while the relative amount of Zn and Ni were varied ($Mn_{0.6}Zn_{0.4-x}Ni_x$, $0.1 \leq x \leq 0.3$). The main chemical, crystallographic and magnetic properties of the as prepared nanomaterials are reported in Table 3.3.

Table 3.3 : Chemical, structural and magnetic parameters of the spinel ferrite nanoparticles prepared by co-precipitation: Composition determined by XRF (a); lattice parameter (b) and crystal size (c) derived from XRD pattern and saturation magnetization (d).

Composition[a]	**Lattice Parameter (nm)[b]**	**Crystal size (nm)[c]**	**Ms (emu/g)[d]**
$Mn_{0.5}Zn_{0.5}Fe_2O_4$	0.8452(2)	7.6(5)	41
$Mn_{0.6}Zn_{0.4}Fe_2O_4$	0.8467(2)	7.3(6)	56
$Mn_{0.7}Zn_{0.3}Fe_2O_4$	0.8498(2)	8.7(4)	70
$MnFe_2O_4$	0.8505(2)	8.2(3)	43
$Mn_{0.6}Zn_{0.3}Ni_{0.1}Fe_2O_4$	0.8451(2)	8.0(2)	62
$Mn_{0.6}Zn_{0.2}Ni_{0.2}Fe_2O_4$	0.8454(2)	9.0(5)	58
$Mn_{0.6}Zn_{0.1}Ni_{0.3}Fe_2O_4$	0.8449(2)	8.5(3)	55

Interestingly, all the samples depict a very similar final crystal size, a zero coercive field and remnant magnetization at room temperature. Indeed, from the magnetic point of view it can be considered that all the samples are in the superparamagnetic regime at the working temperature (i.e., RT). Concerning the $Mn_{1-x}Zn_xFe_2O_4$ particles, the lattice parameter is found to increase with the manganese content, in agreement with the different ionic radius of Manganese and Zinc (Mn^{2+} 0.83 Å; Zn^{2+} 0.74 Å). On the other hand, in the case of the Nickel doped Mn, Zn ferrite, this trend is less appreciable due to the substitution of a cation with a high affinity for tetrahedral (*Td*) cavities as zinc, with one which preferentially occupies the octahedral (*Oh*) ones, as nickel, with the subsequent change of the unit cell edge. From the point of view of magnetic properties, for $Mn_{1-x}Zn_xFe_2O_4$ it was observed that M_S increases from x = 0 to x = 0.3 and then it decreases. For bulk Mn, Zn ferrite a similar trend of M_S on Zn content occurs, although in this case the maximum is reached for x = 0.4. This behaviour is the result of two opposite effects. On one hand, replacing Fe^{3+} ions in *Td* cavities, with diamagnetic Zn^{2+} ions actually increase the uncompensated magnetic moment arising from the *Td* - *Oh* antiferromagnetic coupling. On the other hand, Zn makes the *Td* - *Oh* magnetic coupling weaker, and, above x = 0.4 the antiferromagnetic coupling between Fe^{3+} ions in Oh sites becomes dominant, thus the net magnetic moment diminishes. [16] The shift of the maximum to a lower x value, observed for our samples is due to their nanometric size. In fact, weakening the *Td* - *Oh* magnetic coupling, the introduction of Zn ions in the ferrite lattice decreases the ordering temperature, T_C. This effect becomes particularly relevant for nanostructures where size and surface effects amplify the T_C reduction, (see Section 2.5.3) making the spin disorder larger with increasing the Zn content. This behaviour is in agreement with data reported by Gopalan. [37]

On the other hand, concerning nickel doped Mn, Zn ferrite, it was observed a decrease of the saturation magnetization with increasing the Ni doping. Once again this behaviour can be explained on the basis of the distribution of metal ions within the oxygen lattice cavities. Indeed, supposing zinc occupies exclusively the *Td* sites and manganese and nickel the *Oh* sites, it is possible to estimate the trend of magnetization as function of Nickel content (x) according to the scheme reported in Table 3.4. Here, the magnetization is evaluated by considering the spin-only magnetic moment of each atom (Bohr magneton, μ_B) in every crystallographic sites, assuming ferromagnetic coupling between ions in the same sites and antiferromagnetic coupling for ions laying in different sites, leading to the linear dependence described by Eq. 3.1 and reported in Figure 3.13.

Table 3.4 : Schematic representation of metal cations in *Td* and *Oh* sites and their magnetic moment at 0 K.

Tetrahedral sites		**Octahedral sites**		
Zn^{2+}	Fe^{3+}	Fe^{3+}	Mn^{2+}	Ni^{2+}
$\mu_B = 0$	$\mu_B = 5$	$\mu_B = 5$	$\mu_B = 5$	$\mu_B = 3$
0.4-x	0.6+x	1.4-x	0.6	x

$$[(1.4 - x) * 5 + (0.6 * 5) + x * 3] - [(0.6 + x) * 5] \qquad 3.1$$

This trend is coherent with experimental data, with Ms changing from 62 to 55 emu/g on increasing the Ni content (Figure 3.13). It should be noted that the M_S value of $Mn_{0.6}Zn_{0.4}Fe_2O_4$, which formally can be considered as the first

member of this series deviates from this trend. Such discrepancy can be related to surface effects due to the smaller size of this nanoparticles.

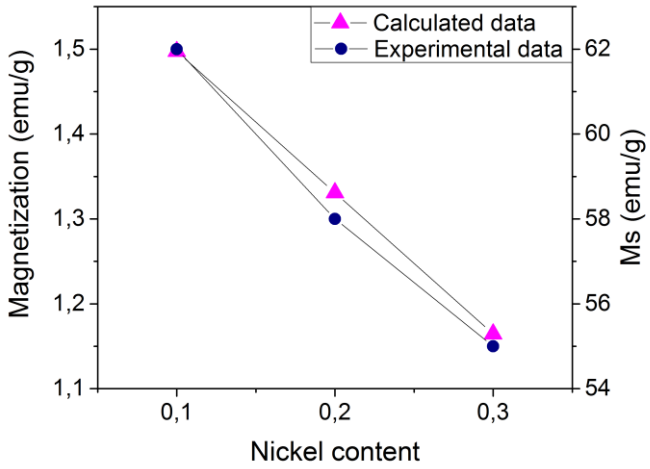

Figure 3.13 : Calculated (left scale) and experimental (right scale) magnetizations as a function of the nickel content.

3.5 Evaluation of the soft behaviour of the doped ferrite nanoparticles.

The results presented above show how the synthetic strategy optimized during this PhD thesis, allowed the production of large amount of nanostructured magnetic materials, with easily tuneable composition, size and magnetic properties. Moreover, taking into account the nature and costs of metal transition precursors and of the solvents used, the synthetic approach can be consider cheap and eco-friendly, and thus of potential interest for industrial production of single domain, crystalline magnetic nanoparticles suitable for the preparation of soft magnetic devices. In order to evaluate if these nanopowders are suitable for the envisaged applications, a deep characterization of the magnetic properties, as described in Chapter 2, is required, particularly as concern the magnetic permeability and core loss. Here, we present the set-up used to perform these measurements.

3.5.1 Evaluation of magnetic permeability.

As described in Chapter 2, the evaluation of the magnetic permeability requires the measurements of the inductance of a toroidal shaped sample. This geometry was chosen to generate a uniform magnetic flux *B* within the whole product, and nullify the demagnetizing filed, which conversely cannot be neglected for different shapes. We also demonstrated that as-synthesized nanoparticles cannot be easily compacted, providing fragile toroids which are difficult to handle. Therefore, in collaboration with Mr. Carlo Bartoli from

ICCOM -CNR, Florence (Italy), it was designed a diamagnetic TEFLON shell, shown in Figure 3.14, to compact the nanopowders in a toroidal shape.

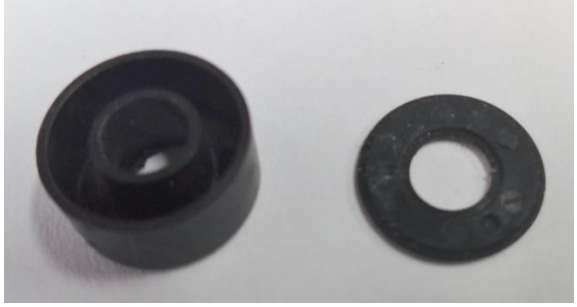

Figure 3.14 : The shell with toroidal shape used for permeability measures.

The cavity had a 14 mm outer diameter (d_{out}), 8 mm inner diameter (d_{in}) and 5 mm height (h). The evaluation of the material permeability (μ) was performed measuring the inductance (L), using a Ronde & Schwarz ZNB8 Vector Network Analyser 9 kHz … 8 GHz, calibrated with a Rosenberg RPC 3.5 mm calibration kit. Measurements were carried out in collaboration with Mr. Marco De Pas, from the Electronic laboratory of European Laboratory for Non-linear Spectroscopy (LENS), Florence (Italy).

The inductance value obtained from the measurement can be used to calculate the relative permeability (μ_r) of the material for a fixed dimensions of the toroid using Eq. 3.2, which correlates μ_r with L, the geometry of the considered system (the outer diameter, d_{out}, the inner diameter, d_{in} and the height, h) with the number of wire turns (N) used for induce the field B:

$$\mu_r = \frac{2\pi L}{\mu_0 h N^2 \ln\left(\frac{d_{out}}{d_{in}}\right)} \qquad 3.2$$

The relative permeability measures were carried out in the frequency range from 100 kHz to 10 MHz. The toroidal shell was completely filled with the as-synthesized magnetic nanoparticles and was wound up with 20 turns of 0.2 mm wire (Figure 3.15). The amount of nanomaterial used for the measure was weighted, in order to relate the permeability value to the density of the as prepared product.

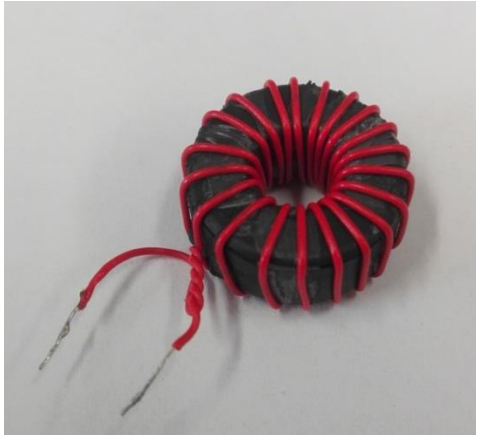

Figure 3.15 : Toroidal shell wound with 20 turns of wire.

The manganese, zinc doped ferrite nanoparticles with different stoichiometric composition discussed in the previous chapter, were then characterized using the setup described above. In order to obtain comparable results, all the samples were measured using a similar amount of magnetic materials and wounded with the same number of turns (20) of copper wire with the same diameter. In Table 3.5 are reported the obtained permeability values.

Table 3.5 : Amount of powder, density (relative to the bulk value) relative permeability and saturation magnetization of nanopowders of ferrites with different composition

Sample	Powder amount (g)	Relative Density (%)	Relative permeability (μ_r)	M_S (emu/g)
$Mn_{0.5}Zn_{0.5}Fe_2O_4$	0.515	19.8(1)	10	41
$Mn_{0.6}Zn_{0.4}Fe_2O_4$	0.499	19.2(1)	9	56
$Mn_{0.7}Zn_{0.3}Fe_2O_4$	0.523	19.9(1)	11	70
$MnFe_2O_4$	0.508	19.6(1)	9	43
$Mn_{0.6}Zn_{0.3}Ni_{0.1}Fe_2O_4$	0.498	19.2(1)	8	62
$Mn_{0.6}Zn_{0.2}Ni_{0.2}Fe_2O_4$	0.505	19.4(1)	8	58
$Mn_{0.6}Zn_{0.1}Ni_{0.3}Fe_2O_4$	0.503	19.4(1)	8	55

The different magnetic nanomaterials inserted in the toroid shell reached a relative density almost constant, 19.5(4) % with respect to the bulk density (5.07 g/cm^3). The resulting relative permeability was close to 10 for all the investigated samples and, considering the little differences in terms of relative density, can be considered practically constant.

This result was quite unexpected due to the large differences in the saturation magnetization of the samples. However, it should be noted that the density of the measured sample is extremely low to consider the product as a single entity since roughly the 80 % is air (μ_r = 1), but it should be rather considered as a mixed system where the magnetic material is largely diluted into a diamagnetic matrix. Moreover, this mixed system is not homogeneous but likely will comprises large aggregates of nanoparticles separated by air gaps which, at the end, play the main contribution in the determination of the final

permeability value. Therefore measurements were repeated increasing the amount of magnetic material into the TEFLON shell so as to increase the relative density of the toroid. This process was performed using a uniaxial pressure system (under patent), which allows a higher compaction of the nanopowders. Interestingly, following this procedure it was possible to increase the amount of material till 0.77-0.78 g reaching a relative density of roughly 30 % (ca. 10 % higher than for not pressed powders.

Table 3.6 : Amount of powder (a), density relative to the bulk value, (b) density increase with respect to the not-pressed nanopowders, (c) relative permeability of not pressed (d) and pressed (e) nanopowders and saturation magnetization (f) of ferrites with different composition.

Nanopowder Samples	**Powder amount (g)[a]**	**Density (%)[b]**	**Density Increase (%) [c]**	**μ_r [d]**	**μ_r [e]**	**M_S (emu/g)[f]**
$Mn_{0.5}Zn_{0.5}Fe_2O_4$	0.772	29.4(1)	+9.8	10	10	41
$Mn_{0.6}Zn_{0.4}Fe_2O_4$	0.784	30.2(1)	+11.0	9	14	56
$Mn_{0.7}Zn_{0.3}Fe_2O_4$	0.792	30.5(1)	+10.6	11	14	70
$MnFe_2O_4$	0.760	29.3(1)	+9.7	9	11	43
$Mn_{0.6}Zn_{0.3}Ni_{0.1}Fe_2O_4$	0.793	30.2(1)	+11.0	8	9	62
$Mn_{0.6}Zn_{0.2}Ni_{0.2}Fe_2O_4$	0.752	29.4(1)	+10.0	8	9	58
$Mn_{0.6}Zn_{0.1}Ni_{0.3}Fe_2O_4$	0.797	30.7(1)	+11.3	8	9	55

Table 3.6 reports the relative permeability of the pressed nanopowders: it appears that the density increase is responsible for an enhancement of μ_r with respect to the not pressed samples. Although the fact that the relative permeability measurements are strongly dependent on the sample

preparation and on the amount of nanomaterial introduced in the toroidal shell make difficult to individuate a marked trend, the increase in density allows the appearance of subtle differences between the various nanomaterials. For example, if the Mn, Zn series is considered it appears that the two samples with lower saturation magnetization ($Mn_{0.5}Zn_{0.5}Fe_2O_4$ and $MnFe_2O_4$,) also have lower relative permeability.

On the other hand, the doping of Mn, Zn ferrite with nickel did not lead to an increase in the relative permeability, even in the presence of higher saturation magnetization, this is probably due to the formation of an increased number of aggregates which in turns increase the dimension of the air gaps, affecting the permeability, as discussed above. These results clearly show how the final densities and the homogeneity of the prepared products affect the magnetic properties of the toroid. Thus, the realization of a compact material with a quasi-bulk density is a mandatory step to investigate and improve the properties of our nanostructured products.

3.6 The set-up for core loss determination

The set-up used to carry out the evaluation of core loss was realized with the support of Mr. Marco De Pas, in the electronic laboratory of European Laboratory for Non-linear Spectroscopy (LENS) of Florence, Italy. The system is composed by five different elements, as schematized in Figure 3.16. The core of the measuring system (blue component) cannot be described in details since it is under patent.

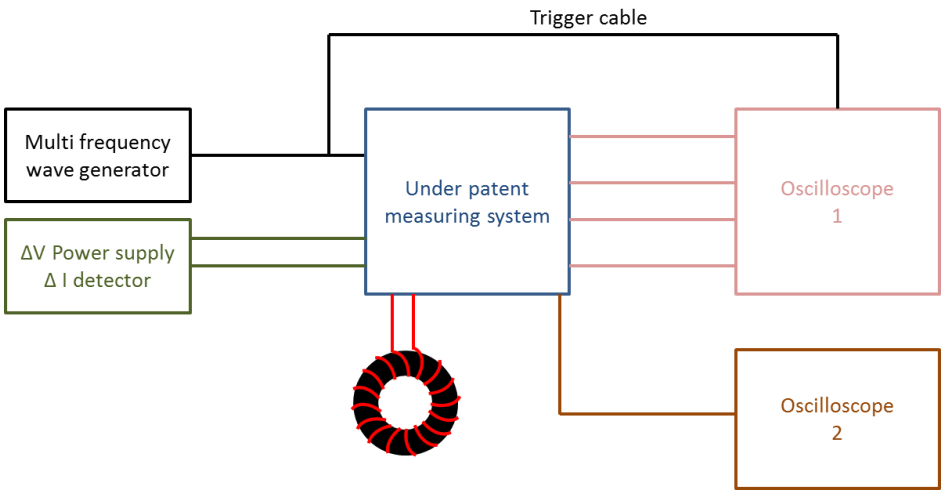

Figure 3.16 : Schematization of core loss set-up with the five different components.

The multi frequency wave generator (black component) generates an electromagnetic square wave in the sample (Black toroid with red wires), with frequency in the range 1 – 2 MHz with a tuneable duty cycle, i.e. the percentage ratio in which a signal is active with respect to the inactive period. The tune of duty cycle allows to temporize the square wave as a function of frequency, so as to have a primary circuit, i.e. the circuit which produces the

electric field which induces the magnetic flux *B* in the toroid, with the correct temporization, controlled with the oscilloscope 1 (Pink component). The shape of the resultant square wave is controlled in the oscilloscope 2 (Brown component).

Then a tension (*V*) is applied on the sample by the power supply and the current flowing in the coil (*I*) is measured by the power supply itself. The total core losses are then due to the product between the tension difference and the currents (*P = V x I*). To obtain a more precise result, the power losses due to the circuits and to the measuring system (Blue components), evaluated by the oscilloscope 1, are subtracted from the total losses.

Operatively, considering the number of wire turns (*N*), the dimension of the toroidal sample, from which we can estimate the area crossed by the *B* flux (A_e, expressed in cm^2), and the frequency used, from which the activation time of tension difference is calculated ($T_{on} = ½\ \omega$, expressed in seconds), it is possible to adjust the voltage to produce a certain *B* in the sample, using the following Eq. 3.3:

$$V_{in} = \frac{2B\ A_e N}{T_{on}} \qquad 3.3$$

Then, for a selected *B,* measures were carried out applying the corresponding voltage. In Table 3.6 are reported the core loss for different nanopowders inserted in the toroidal shell. Measures were performed at 1 and 2 MHz inducing a 500 Gauss flux. The results are reported in mW/cm^3, rescaling the core loss to the volume of the sample. The measuring system provides results with a 10% of accuracy.

Table 3.7 : Core loss at 1MHz and 2MHz, inducing a 500 Gauss of *B* flux, for different nanomaterials pressed in the toroidal shell.

Sample	Powder amount (g)	Density (%)	μ_r on pressed nano-material	Core loss 1MHz (mW/cm^3)	Core loss 2MHz (mW/cm^3)
$Mn_{0.5}Zn_{0.5}Fe_2O_4$	0.772	29.4(1)	10	8830	19540
$Mn_{0.6}Zn_{0.4}Fe_2O_4$	0.784	30.2(1)	14	8201	18200
$Mn_{0.7}Zn_{0.3}Fe_2O_4$	0.792	30.5(1)	14	8198	18230
$MnFe_2O_4$	0.760	29.3(1)	11	8530	18990
$Mn_{0.6}Zn_{0.3}Ni_{0.1}Fe_2O_4$	0.793	30.2(1)	9	9200	20530
$Mn_{0.6}Zn_{0.2}Ni_{0.2}Fe_2O_4$	0.752	29.4(1)	9	9251	20680
$Mn_{0.6}Zn_{0.1}Ni_{0.3}Fe_2O_4$	0.797	30.7(1)	9	9230	21402

Considering that products currently employed in electronic devices have at the same field and 2 MHz core loss below 1000 mW/cm^3 and relative permeability over 1000, these results clearly show how the low density and the large air gap occurring in our samples strongly decrease permeability, affecting at the same time the core losses, which result very large.

References

[1] K. J. Klabunde, *Nanoscale Materials in Chemistry*, vol. 3. New York, USA: John Wiley & Sons, Inc., 2001.

[2] a. L. Rogach, D. V. Talapin, E. V. Shevchenko, a. Kornowski, M. Haase, and H. Weller, "Organization of Matter on Different Size Scales: Monodisperse Nanocrystals and Their Superstructures," *Adv. Funct. Mater.*, vol. 12, no. 10, pp. 653–664, Oct. 2002.

[3] T. Hyeon, "Chemical synthesis of magnetic nanoparticles," *Chem. Commun.*, no. 8, pp. 927–934, 2003.

[4] G. Schmid, *Nanoparticles*. Weinheim, FRG: Wiley-VCH Verlag GmbH & Co. KGaA, 2003.

[5] J. H. Fendler and Y. Tian, *Nanoparticles and Nanostructured Films*. Weinheim, Germany: Wiley-VCH Verlag GmbH, 1998.

[6] J. A. Lopez Perez, M. A. Lopez Quintela, J. Mira, J. Rivas, and S. W. Charles, "Advances in the preparation of magnetic nanoparticles by the microemulsion method," *J. Phys. Chem. B*, vol. 101, no. 41, pp. 8045–8047, 1997.

[7] P. A. Dresco, V. S. Zaitsev, R. J. Gambino, and B. Chu, "Preparation and peoperties of magnetite and polymer magnetite nanoparticle," *Langmuir*, vol. 15, no. 12, pp. 1945–1951, 1999.

[8] J. Dobson, W. Tan, S. Santra, R. Tapec, N. Theodoropoulou, and J. Dobson, "Synthesis and Characterization of Silica-Coated Iron Oxide Nanoparticles in Microemulsion : The Effect of Nonionic Surfactants Synthesis and Characterization of Silica-Coated Iron Oxide Nanoparticles in Microemulsion : The Effect of Nonionic," no. MAY 2001, pp. 2900–2906, 2015.

[9] J. Wang, J. Sun, Q. Sun, and Q. Chen, “One-step hydrothermal process to prepare highly crystalline Fe3O4 nanoparticles with improved magnetic properties,” *Mater. Res. Bull.*, vol. 38, no. 7, pp. 1113–1118, Jun. 2003.

[10] F. Gözüak, Y. Köseoğlu, A. Baykal, and H. Kavas, “Synthesis and characterization of CoxZn1−xFe2O4 magnetic nanoparticles via a PEG-assisted route,” *J. Magn. Magn. Mater.*, vol. 321, no. 14, pp. 2170–2177, Jul. 2009.

[11] J. Wang, F. Ren, R. Yi, A. Yan, G. Qiu, and X. Liu, “Solvothermal synthesis and magnetic properties of size-controlled nickel ferrite nanoparticles,” *J. Alloys Compd.*, vol. 479, no. 1–2, pp. 791–796, Jun. 2009.

[12] D. Jézéquel, J. Guenot, N. Jouini, and F. Fiévet, “Submicrometer zinc oxide particles: Elaboration in polyol medium and morphological characteristics,” *J. Mater. Res.*, vol. 10, no. 1, pp. 77–83, 1995.

[13] F. Fievet, J. Lagier, B. Blin, B. Beaudoin, and M. Figlarz, “Homogeneous and heterogeneous nucleations in the polyol process for the preparation of micron and submicron size metal particles,” *Solid State Ionics*, vol. 32–33, pp. 198–205, Feb. 1989.

[14] S. Lefebure, E. Dubois, V. Cabuil, S. Neveu, and R. Massart, “Monodisperse magnetic nanoparticles: Preparation and dispersion in water and oils,” *J. Mater. Res.*, vol. 13, no. 10, pp. 2975–2981, Jan. 2011.

[15] A.-H. Lu, E. L. Salabas, and F. Schüth, “Magnetic nanoparticles: synthesis, protection, functionalization, and application.,” *Angew. Chem. Int. Ed. Engl.*, vol. 46, no. 8, pp. 1222–44, Jan. 2007.

[16] S. Basak, D.-R. Chen, and P. Biswas, “Electrospray of ionic precursor solutions to synthesize iron oxide nanoparticles: Modified scaling law,”

Chem. Eng. Sci., vol. 62, no. 4, pp. 1263–1268, Feb. 2007.

[17] R. Massart, E. Dubois, V. Cabuil, and E. Hasmonay, "Preparation and properties of monodisperse magnetic fluids," *J. Magn. Magn. Mater.*, vol. 149, no. 1–2, pp. 1–5, Aug. 1995.

[18] H. Iida, K. Takayanagi, T. Nakanishi, and T. Osaka, "Synthesis of Fe3O4 nanoparticles with various sizes and magnetic properties by controlled hydrolysis.," *J. Colloid Interface Sci.*, vol. 314, no. 1, pp. 274–80, Oct. 2007.

[19] S. Laurent, D. Forge, M. Port, A. Roch, C. Robic, L. Vander Elst, and R. N. Muller, "Magnetic iron oxide nanoparticles: synthesis, stabilization, vectorization, physicochemical characterizations, and biological applications.," *Chem. Rev.*, vol. 108, no. 6, pp. 2064–110, Jun. 2008.

[20] C. Hu, Z. Gao, and X. Yang, "Fabrication and magnetic properties of Fe3O4 octahedra," *Chem. Phys. Lett.*, vol. 429, no. 4–6, pp. 513–517, Oct. 2006.

[21] R. F. Ziolo, E. P. Giannelis, B. A. Weinstein, M. P. O'Horo, B. N. Ganguly, V. Mehrotra, M. W. Russell, and D. R. Huffman, "Matrix-Mediated Synthesis of Nanocrystalline ggr-Fe2O3: A New Optically Transparent Magnetic Material," *Science (80-.).*, vol. 257, no. 5067, pp. 219–223, Jul. 1992.

[22] L. Shen, P. E. Laibinis, T. A. Hatton, L. Shen, P. E. Laibinis, and T. A. Hatton, "Bilayer Surfactant Stabilized Magnetic Fluids : Synthesis and Interactions at Interfaces Bilayer Surfactant Stabilized Magnetic Fluids : Synthesis and Interactions at Interfaces," no. 11, pp. 447–453, 1999.

[23] X.-P. Qiu, "Synthesis and characterization of magnetic nano particles," *Chinese J. Chem.*, vol. 18, no. 6, pp. 834–837, Aug. 2010.

[24] D. S. Mathew and R.-S. Juang, “An overview of the structure and magnetism of spinel ferrite nanoparticles and their synthesis in microemulsions,” *Chem. Eng. J.*, vol. 129, no. 1–3, pp. 51–65, May 2007.

[25] D. S. McClure, “The distribution of transition metal cations in spinels,” *J. Phys. Chem. Solids*, vol. 3, no. 3–4, pp. 311–317, Jan. 1957.

[26] A. S. Vaingankar, B. V Khasbardar, and R. N. Patil, “X-ray spectroscopic study of cobalt ferrite,” *J. Phys. F Met. Phys.*, vol. 10, no. 7, pp. 1615–1619, Jul. 1980.

[27] D. Carta, M. F. Casula, A. Falqui, D. Loche, G. Mountjoy, C. Sangregorio, and A. Corrias, “A Structural and Magnetic Investigation of the Inversion Degree in Ferrite Nanocrystals MFe 2 O 4 (M = Mn, Co, Ni),” *J. Phys. Chem. C*, vol. 113, no. 20, pp. 8606–8615, May 2009.

[28] D. Carta, G. Mountjoy, G. Navarra, M. F. Casula, D. Loche, S. Marras, and A. Corrias, “X-ray Absorption Investigation of the Formation of Cobalt Ferrite Nanoparticles in an Aerogel Silica Matrix,” *J. Phys. Chem. C*, vol. 111, no. 17, pp. 6308–6317, May 2007.

[29] J. M. D. Coey, *Magnetism and Magnetic Materials*. 2010.

[30] H. S. C. O’Neill and A. Navrotsky, “Cation Distributions and Thermodynamic Properties of Binary Spinel Solid Solutions.,” *Am. Mineral.*, vol. 69, no. 6–8, pp. 733–753, 1984.

[31] A. P. Sincero, *Physical-Chemical Treatment of Water and Wastewater*. 2002.

[32] R. a. Reichle, K. G. McCurdy, and L. G. Hepler, “Zinc Hydroxide: Solubility Product and Hydroxy-complex Stability Constants from 12.5–75 °C,” *Can. J. Chem.*, vol. 53, no. 24, pp. 3841–3845, Dec. 1975.

[33] C. Rath, K. . Sahu, S. Anand, S. . Date, N. . Mishra, and R. . Das,

"Preparation and characterization of nanosize Mn–Zn ferrite," *J. Magn. Magn. Mater.*, vol. 202, no. 1, pp. 77–84, Jun. 1999.

[34] Y. Xuan, Q. Li, and G. Yang, "Synthesis and magnetic properties of Mn–Zn ferrite nanoparticles," *J. Magn. Magn. Mater.*, vol. 312, no. 2, pp. 464–469, May 2007.

[35] S. Lower, "http://chem.libretexts.org/Textbook_Maps/General_Chemistry_Textbook_Maps/Map%3A_Chem1_(Lower)/08%3A_Solution_Chemistry/8.6%3A_Solubility_of_Salts%2F%2FSolubility_Equilibria," *Chem 1 Virtual Textbook*. .

[36] K. Miura, K. Hirao, and Y. Shimotsum, "Nanowire formation under femtosecond laser radiation in liquid," in *Nanowires - Fundamental Research*, InTech, 2011.

[37] E. Veena Gopalan, I. A. Al-Omari, K. A. Malini, P. A. Joy, D. Sakthi Kumar, Y. Yoshida, and M. R. Anantharaman, "Impact of zinc substitution on the structural and magnetic properties of chemically derived nanosized manganese zinc mixed ferrites," *J. Magn. Magn. Mater.*, vol. 321, no. 8, pp. 1092–1099, Apr. 2009.

[38] R. Arulmurugan, G. Vaidyanathan, S. Sendhilnathan, and B. Jeyadevan, "Mn–Zn ferrite nanoparticles for ferrofluid preparation: Study on thermal–magnetic properties," *J. Magn. Magn. Mater.*, vol. 298, no. 2, pp. 83–94, Mar. 2006.

Chapter 4

From nanopowders to a high density product.

As described before, in order to measure the performance of the soft magnetic products prepared in this thesis, the production of toroid with bulk-like density is a mandatory requirement. In this Chapter we will discuss all the attempts made to transform the as-synthesized nanopowders in a hard resistant material. First, the powder was compacted with a hydraulic press in a home-made die and then the toroid structure underwent a heating treatment, in order to increase the final density of the material. The realization of this goal required the design of a specific toroid die and the optimization of the heating treatment. Then, the powder were sintered using two techniques, the classic sintering approach and high pressure field assisted sintering method. In this Chapter the detailed characterization of the structural and physical properties of the obtained samples is presented together with a discussion on the actual perspectives for the application of these materials for the realization of soft magnetic cores for high frequency electronic inductors and transformers.

4.1 Toroid die fabrication.

A prototype of a toroid die made of diamagnetic 316 austenic stainless steel was realized and then optimized during this PhD thesis. It should be noted that although the realization of a classic toroidal shape die is not a problem when micrometric powders are used, a different approach for the compaction must be used when the material size is decreased to the nanometric scale. Indeed, the nanometric size makes easier the permeation of grains in the different die components. Therefore, it was necessary to focus attention into the die design to enable the production of compacted nanopowder *green specie*s (i.e. pressed sample before being exposed to a heating treatment). The scheme of the first die (prototype α) realized in the mechanic laboratory of the Consiglio Nazionale delle Ricerche (CNR), in collaboration with Mr. Carlo Bartoli, is described in Figure 4.1, where the element sizes are expressed in millimetre (mm). The die is composed by four different elements described in the following scheme:

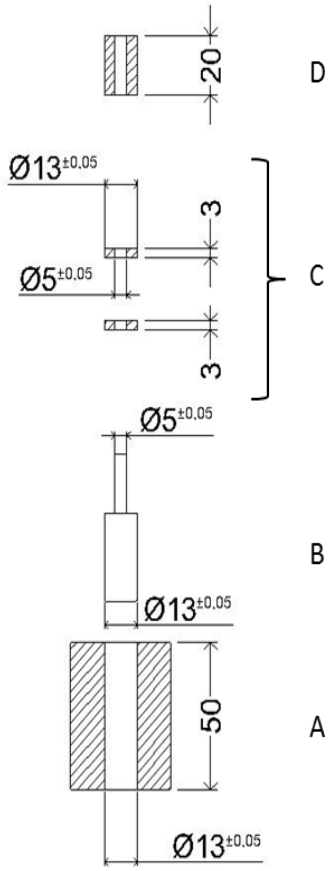

Figure 4.1 : Description of the main components of the prototype α.

A: A cylindrical external matrix with internal and external diameters of 13 and 40 mm, respectively, and height of 50 mm.

B: A bottom piston which is introduced in the matrix A; it has an external diameter of 13 mm, with a tolerance value of +/- 0.05 mm (H7 tolerance). The diameter of the central piston in the upper part, adapted to produce the "hole" of the toroid, is 5 mm (H7) diameter.

C: A sample holder made of two rings with 3 mm thickness, which perfectly fit in the piston B and in the matrix A (internal and external diameter are 5 and 13 mm (H7), respectively).

D: Upper piston for pressing the nanopowders; it has the same internal and external diameter of C and 20 mm thickness.

Operatively, piston **B** was inserted in matrix **A** and one of the rings **C** was housed over **B**, defining a cavity which was filled by the nanopowder and closed by the second ring **C**; finally, the upper piston **D** was accommodated and pressure was applied. Unfortunately the prototype α did not provided satisfactory results. Indeed, due to the nanometric nature of the powders, the die was very often seized up, making impossible to separate the components

of the die (i.e., pistons **B** and **D** and rings **C** from the matrix **A)** after pressure was applied. In order to overcome this drawback the tolerance between the different parts of the mold was increased. This avoided the die blockage although a portion of the nanopowders extruded from the die.

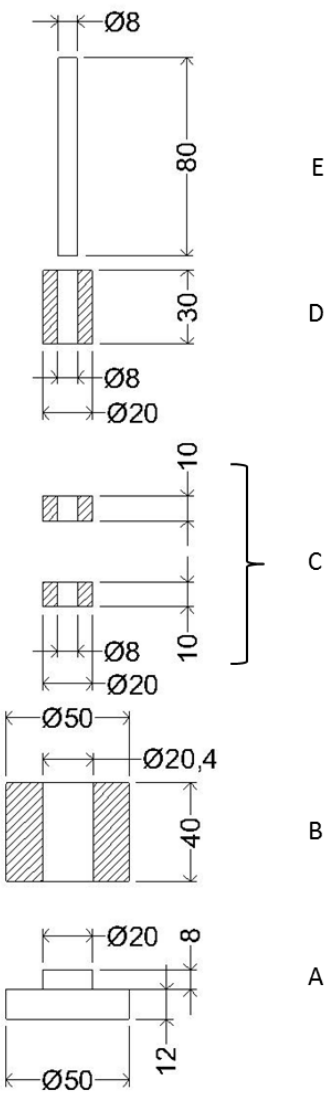

Figure 4.2 : Description of the main components of the first improved die (prototype β).

A second die (prototype β) with the five elements A-E was thus realized, as shown in Figure 4.2 on the left. In order to improve the resistance of the object the main modification introduced is the increase of the size of the sample host, the inner and outer diameters becoming 8 and 20 mm, respectively.

Furthermore, the tolerance between the parts C and D (20 mm external Ø) and the matrix B (20.4 mm matrix internal Ø) is increased to avoid seizing up. Moreover, the piston B of the previous system (Figure 4.1) is now divided in the cylinder E and the bottom piston A.

Thanks to this new design it was possible to avoid the die's blockage and to recover the pressed sample.

However, the high friction between cylinder **E** and extruded nanopowders stick on the wall of the central hole often caused the break of the toroid. In order to avoid this problem, the **E** piece was modified as shown in Figure 4.3:

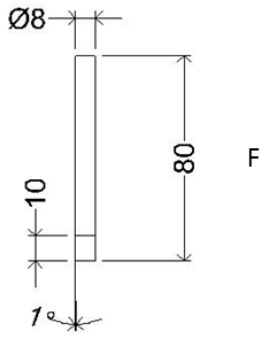

Figure 4.3 : Representation of the improved central cylinder **F**.

The new F part of the die is very similar to the previous one although, in this case one of the terminals was milled to obtain a conic shape of 10 mm of height and tilted by 1° angle with respect to the vertical.

Thanks to all these improvements we managed to obtain toroids of compacted nanopowders with good mechanical resistance and manageability (Figure 4.4), available for the further heating treatments.

Figure 4.4 : Image of green toroid sample.

4.2 Optimization of the heating treatment

In order to densify the as obtained green toroids, a series of heating treatments were performed on the nanopowders. Due to the fact that, as described in Chapter 3, Mn^{2+} ions are instable towards oxidation to form Mn^{3+} or Mn^{4+} species, heating process to produce Mn ferrites powder, reported in the literature, are normally carried on under air atmosphere.

Nevertheless, in our case, when a compacted green toroid was subjected to a heat treatment under air atmosphere we observed a structural transformation of the product. The green toroid was thermally treated under air at 1000 ºC with a rate of 5 °C/min and kept at that temperature for 6 hours (Heating ramp 1, HR1) as schematized in Figure 4.5.

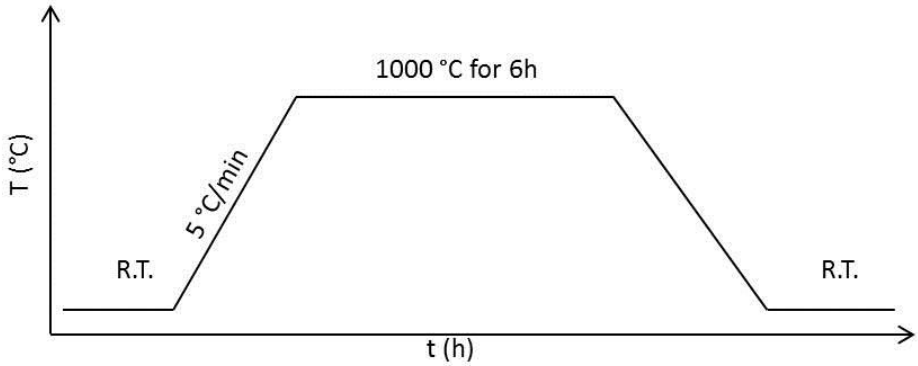

Figure 4.5 : Heating ramp, HR1, for toroidal nanopowder sintering.

The product was then investigated by X-ray powder diffraction technique. The XRD pattern was measured on the powder obtained from the grinded toroid and it is shown in Figure 4.6.

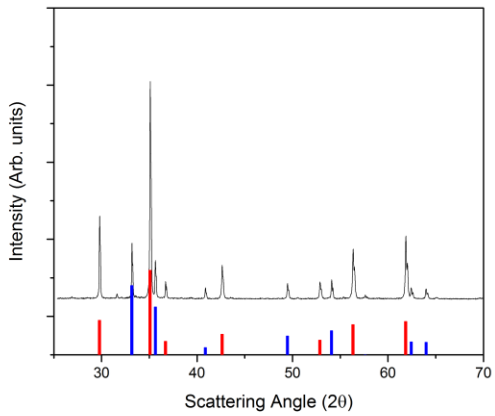

Figure 4.6 : Diffraction pattern recorded on grinded sample sintered in air. Red and blue lines refer to reference patterns for Mn, Zn ferrite and hematite (α-Fe_2O_3), respectively

Two different crystallographic structures can be identified in the analysed powder: one that can be indexed to a Mn, Zn ferrite with cubic spinel structure (*ICCP database PDF 74-2400*) and a second one corresponding to hematite (α-Fe_2O_3), the most stable iron oxide structure, which crystallizes in the rhombohedral lattice system $R\overline{3}c$ (*ICCP database PDF 86-2368*). The relative weight amount was calculated by Rietveld refinement and revealed a presence of ca. 30 % of hematite in the sintered powder. The formation of this secondary phase can be associated to the oxidation of Mn^{2+} ions. Indeed, although in the diffraction pattern no crystalline phases containing Mn^{3+} and/or Mn^{4+} could be identified the decrease of the lattice parameter of the spinel, from 0.8465 to 0.8445 nm, is an indication that part of the Mn^{2+} ions left the ferrite structure inducing a rearrangement of the cations. Considering that X-ray fluorescence indicates that the total composition of the powder did not change, it can be argued that Mn^{3+} and Mn^{4+} probably formed amorphous species not detectable by XRD.

Therefore, in order to avoid this problem, all the heating treatments were performed under inert conditions using a tubular oven with a constant N_2 flow after properly purging the system. The oven is equipped with a Mullite ($Al_{4+2x}Si_{2-2x}O_{10-x}$) working tube of 60 mm and 50 mm outer and inner diameters, respectively.

4.2.1 Improvement of the oven.

The tubular furnace was thus modified to work under an inert gas flow to avoid the formation of satellite phases and preserve the correct stoichiometry of the spinel ferrite, by adding two flanges to the working tube, as shown in Figure 4.7.

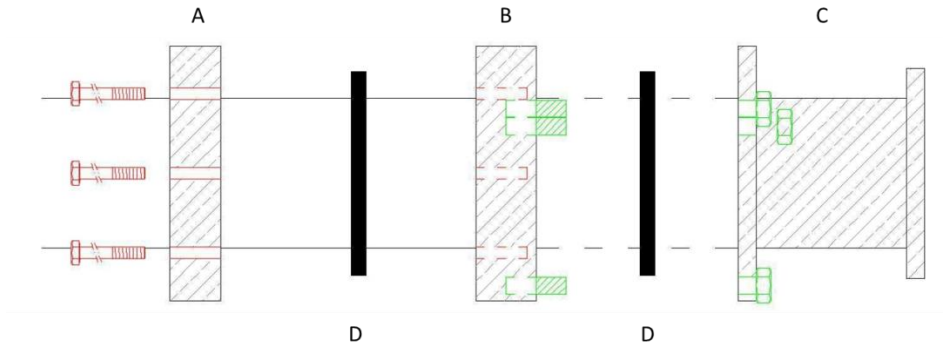

Figure 4.7 : Tubular furnace flanges for inert atmosphere operating.

The two flanges, optimized from commercial ones, were mechanically milled from original diamagnetic 316 austenic stainless steel rod. They were composed of three different elements (**A-C**): two Viton (elastomeric fluorocarbon, resistant up to 200 °C) O-rings (**D**) to couple each steel part and seal the tubular system. On the other hand, part **A** (65 mm inner Ø), shown in detail in Figure 4.8, fits around the working Mullite tube of the tubular furnace with six holes adapted to screw it to the piece **B**.

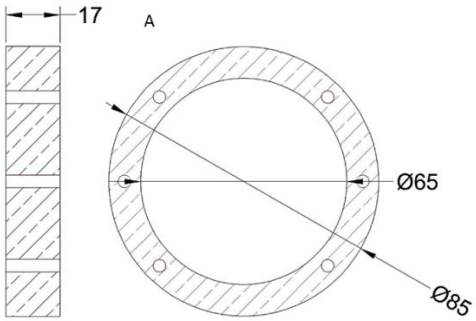

Figure 4.8 : Part A of the flange for operating under inert atmosphere.

The part **B**, as shown in Figure 4.9, presents:

- A side opposite to **A,** with the six threads for screw the M4 bolts, a conical incision for accommodate the O-ring and a spline to be fitted in the working tube (red ring in the central section image).
- A side opposite to **C**, with three M6 studs for fasten to **C** and the spline for accommodate the O-ring.

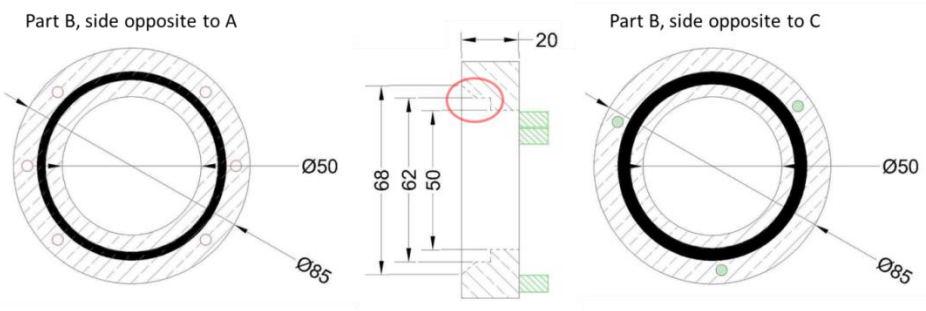

Figure 4.9 : Part **B** of the flange operating under controlled atmosphere.

The part **C** (see Figure 4.10) has three holes for connection to **B** by three nuts and a DN50 vacuum connector to plug it to the needle valve, which controls the inert gas flow.

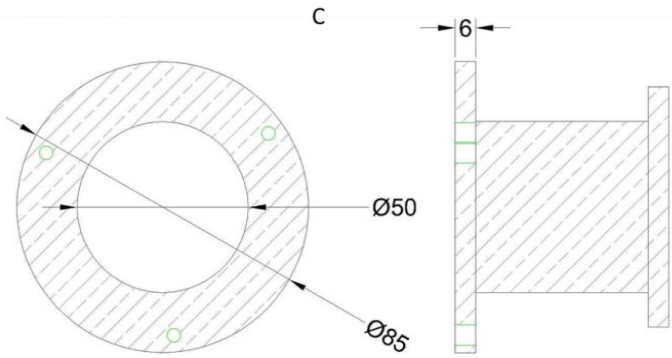

Figure 4.10 : Part **C** of the flange for operation under inert atmosphere.

Working under a nitrogen flow, we found no chemical transformation of the as-synthesized material occurred. In fact, as can be seen in Figure 4.11 the XRD pattern of a green toroid subjected to the heating ramp HR1 (see above) shows the presence of the expected ferrite phase alone, with a lattice parameter coherent with that of Mn, Zn ferrite (i.e. 0.8464 nm).

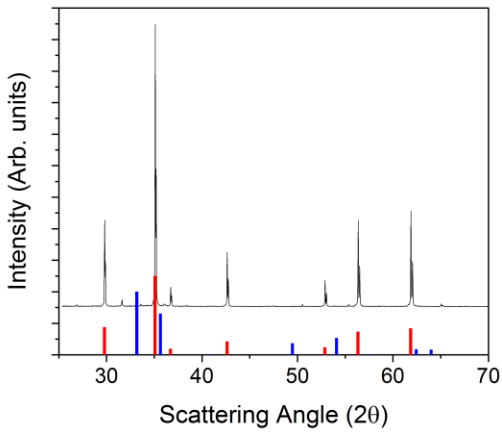

Figure 4.11 : XRD pattern of a grinded sample sintered in inert atmosphere. Red and blue lines refer to the reference patterns for Mn, Zn ferrite and iron oxide hematite, respectively.

4.2.2 Optimization of the heating procedures.

As demonstrated in Chapter 3, one of the most crucial aspects for the preparation of sintered product with high magnetic permeability and low core losses is the final density obtained after the heating treatment. Indeed, the final density of the system must be as close as possible to the bulk one (i.e., 5.07 g/cm^3 for Mn, Zn ferrite). In order to optimize the sintering strategy, several tests with different target temperature were performed, maintaining the dwell time (6 h) and the heating rate (10 °C/min) constant. However, with respect to HR1, an additional step at 120 ºC for 2 hours was added to the heating treatment (HR2, Figure 4.12) to completely eliminate volatile solvent molecules remained from the synthetic procedure. In this way, the low temperature elimination of solvents such as water, acetone and/or ethanol, allows for the formation a solid structure which can be more easily sintered.

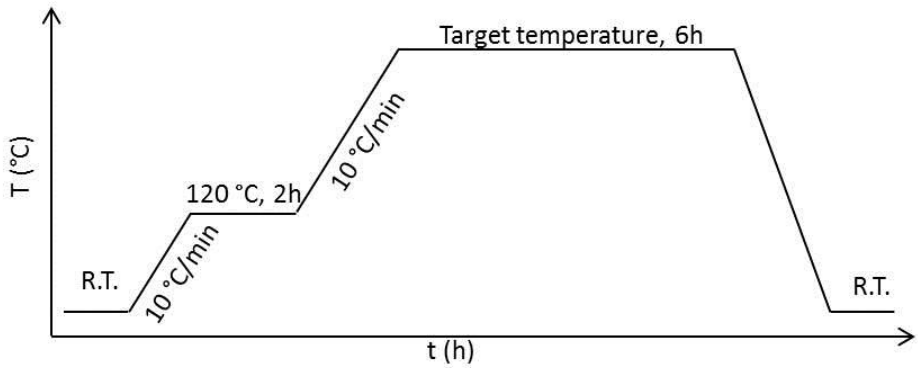

Figure 4.12 : Heating ramp (HR2) for the toroidal sample sintering.

Figure 4.13 depicts the relative density (i.e., density percentage with respect to the bulk one, 5.07 g/cm^3) of sintered toroids as a function of the sintering

temperature. Two different approaches were used to measure the final density of the sintered structures: the classic Archimedean method, based on weighting the sample in water and in air with a microbalance; measuring the weight and the volume with a high precision calibre (geometric method).

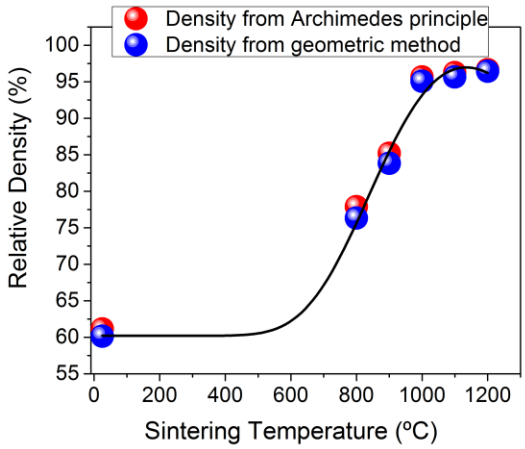

Figure 4.13 : Relative density increase as a function of the sintering temperature. Black line is a guide for the eyes.

It can be observed that the final relative density increases with the increase of the sintering temperature. Before sintering, green structures have a maximum relative density of 60 % (i.e., 3.04 g/cm^3). However, for enough high temperatures (≥ 1000) the density is close to the expected bulk value (5,07 g/cm^3), being ca. 95(5) %, indicating the achievement of a very dense system. Small differences observed between densities evaluated by the two methods are due to the presence of closed porosity, i.e. the porosity not accessible to water, (Archimedes principle) and to the large error in the measure of toroid dimensions (geometric method). More accurate information was obtained from a dilatometric analysis, presented in Figure 4.14, carried out in collaboration with Prof. Vincenzo Sglavo and Dott. Matteo Frasnelli from University of Trento. Three different Ø 13 mm pellet sample was measured at

increasing temperatures from RT to 1600 °C, at 10 °C/min heating rate under Argon flow.

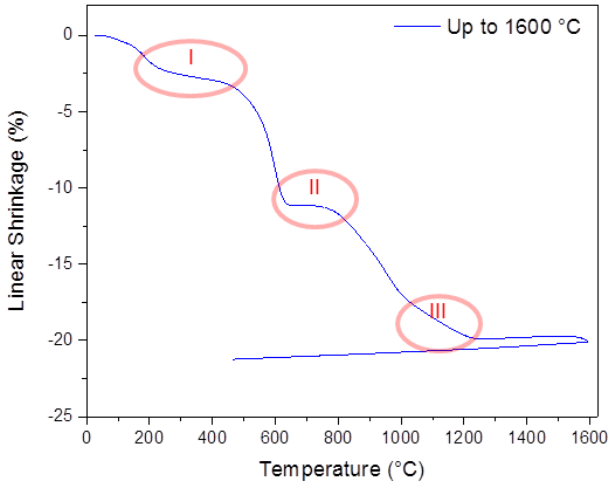

Figure 4.14 : Relative shrinkage as a function of the sintering temperature.

In Figure 4.14 is reported the linear shrinkage related to the initial dimension of the pellet at variable temperature between room temperature and 1600 °C. It is possible to distinguish different zones related to three *plateaux* in the densification process: the first, plateaux is associated to the loss of humidity and degassing of the compacted pellet; the second one is related to the crystallization of a residual amorphous impurity, while the third corresponds to the ending of the densification process. These data are in good agreement with those obtained by density measurements. In order to investigate the evolution of the microscopic features with temperature, two other samples, sintered at 700 °C and 1200 °C respectively, were prepared. The three products were analysed by SEM to obtain information on grains size and on the presence of pores. SEM images were acquired at a fracture surface produced by breaking the sample. SEM images (Figure 4.15) of a pellet sintered at 700 ºC shows a highly porous structure, while the grain maintains a nanoscale, although larger, dimensions (ca. 100 nm). On the other hand,

sample treated at 1200 °C shows a higher densified structure with the presence of regions with pores of distinct size (< 1 μm and around 5-10 μm). Moreover, it can be observed that at this temperature the initial nanometric size of green toroid was lost forming a rather continuous structure of polyhedral grains with sizes in the range of 2-3 μm. Finally, when the sintering temperature reach 1600 ºC the grain size increases drastically forming particles of 60-70 μm. In addition, the porosity at the grain boundaries is reduced and a regular and almost monodisperse bubble-like structures of 5 – 7 μm dimension are formed, possibly due to the elimination of ZnO.

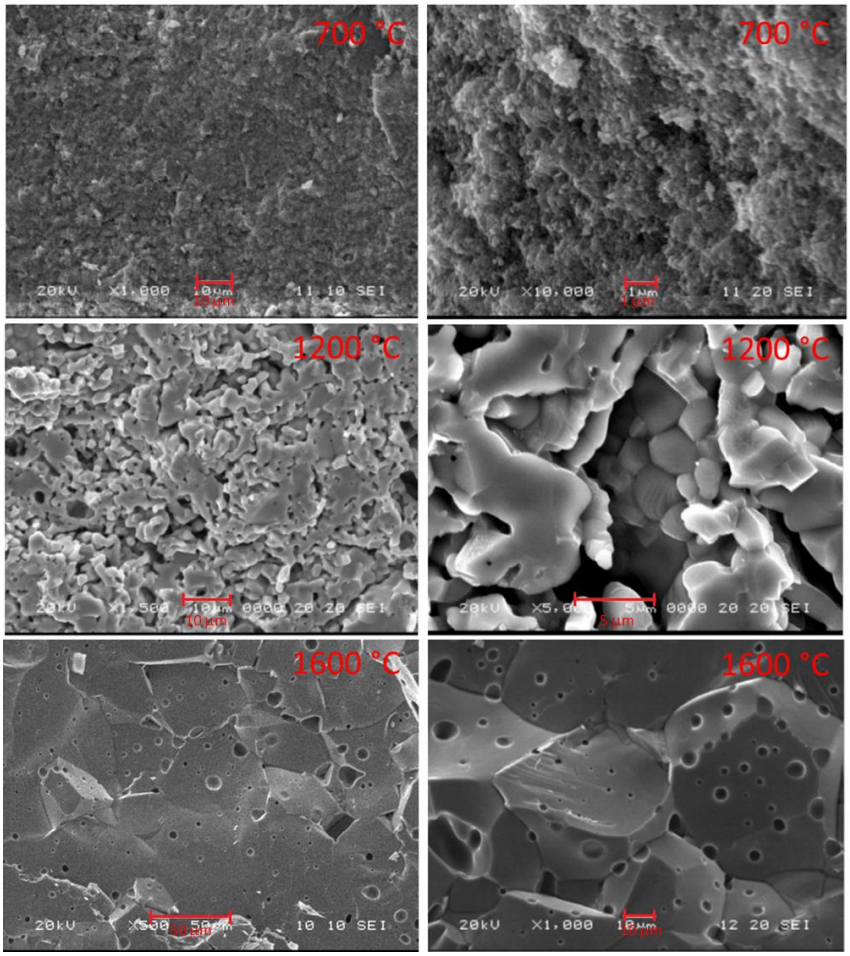

Figure 4.15 : Representative SEM images of pellets sintered at 700 °C, 1200 °C and 1600 °C.

Therefore, on the basis of these results we can conclude that the optimal heating treatments for the sintering of the compacted nanopowders involves temperature comprised in the 1000 °C - 1200 °C range. Above 1200 °C a too large increase of grain size, in the range of tens of micrometres, occurs.

4.2.3 The sintering process.

As we have seen in the previous chapter, core losses are strictly related to the final density. Therefore, once optimized the toroidal die and found the correct sintering atmosphere, the main efforts were devoted to find a suitable heating treatment. In particular two different approaches were explored:

- Classic Sintering Process: In this case the green toroids were exposed to heat treatments in a tubular furnace at variable sintering temperature. Using this technique micrometric-structured final products were obtained.

- High Pressure Field Assisted Sintering Technique (HP-FAST): green toroids were sintered by exploiting the heat produced by Joule effect, applying a DC current to a non-conductive die comprising the powder and simultaneously applying an uniaxial pressure. Variable sintering temperature and applied pressure were explored, to obtain nanometric structured products.

In the next paragraphs we will discuss in detail the results obtained using these two approaches, enlightening the advantages of each method towards the

realization of high compact, ferrite based materials with high permeability and low power losses to be used in the envisaged electronic applications.

4.2.3.1 The classical sintering approach.

As described above, the optimization of the toroid compaction, oven equipment and the thermal treatment procedure allowed us the production of bulk-like products with controlled micrometric grain size and fixed chemical composition. At this point, a series of samples treated at different sintering temperatures were produced to study their final magnetic and electronic properties. The series of annealed samples were treated at temperatures starting from 1000 ºC where it was demonstrated the density of the compacted powder reach values close to the bulk material (i.e., 95(5) % of relative density). The classic heating treatments used for sintering the toroidal samples is shown in Figure 4.16. The treatment, HR3, is slightly modified with respect to HR2 and involves a degassing step at 120 °C for 2 hours, a 5 °C/min heating ramp, 6 hours dwell time for densification process and a controlled cooling process until 700 °C at 5 °C/min, in order to reduce cooling stress to the working tube and to the toroids.

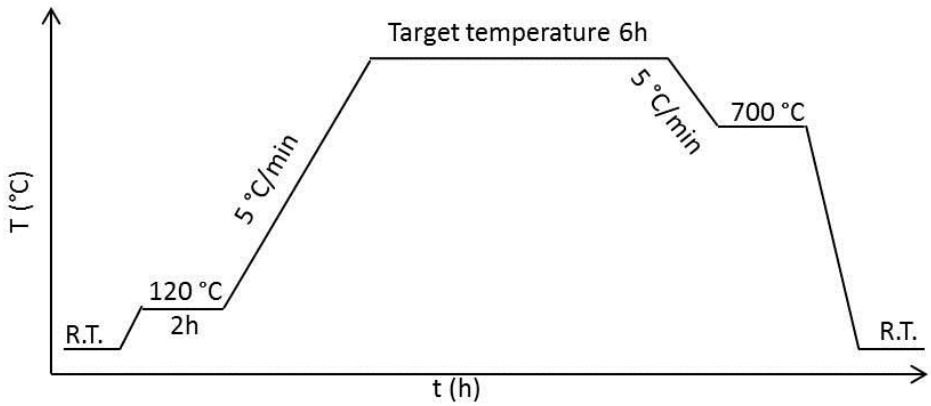

Figure 4.16 : Heating ramp for toroidal sample sintering.

A series of four samples sintered at different temperatures were obtained and their morphological, structural and magnetic properties are reported in Table 4.1.

Table 4.1 : Crystallographic and magnetic data of sintered toroidal samples.

Sintering temperature (ºC)	Lattice Parameter (nm)	Grain size (μm)	Relative Density (%)	Ms (emu/g)
1000 °C	0.8462(2)	1.0(3)	93.1(3)	89
1050 °C	0.8466(2)	3.0(7)	95.2(2)	88
1100 °C	0.8465(2)	5(1.5)	96.4(1)	87
1200 °C	0.8468(2)	10(2)	98.1(1)	90

All toroidal samples showed crystallographic patterns with a well-defined unique crystallographic phase corresponding to the cubic spinel structure $Fd\overline{3m}$, as shown in Figure 5.11. The calculated lattice parameters were all in the same range, with values of roughly 0.8465(5) nm, confirming the preservation of the initial $Mn_{0.6}Zn_{0.4}Fe_2O_4$ composition. In these cases, the evaluation of crystal size from Scherrer equation was not indicative, because the intrinsic line broadening is lower or comparable to the one originate by the instrument (Figure 4.17). Therefore, SEM analysis resulted necessary to estimate grains dimension.

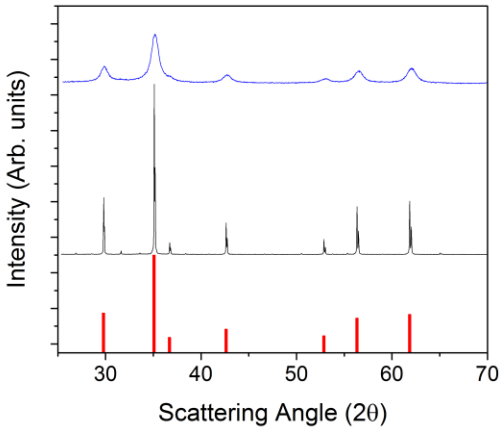

Figure 4.17 : XRD pattern of a grinded sintered sample (black). Blue line is the pattern of the as-synthesized nanopowders; red lines correspond to the reference pattern for Mn, Zn ferrite.

In Figure 4.19 are shown the SEM images of samples sintered at different temperature, obtained by inspecting a fracture surface of the toroids, as previously described. For each sample are reported two images at different magnification, in order to appreciate the densification process, the presence of porosity and the grains size.

From these images it is possible to notice the increase in grain dimension as a function of the sintering temperature. The sample sintered at 1000 °C shown a diffused porosity and inhomogeneous grains growth, with large zones of submicron structure and smaller areas where process has forced the complete sintering of the powder, with grains diameter about 1 µm. Interestingly, as the sintering temperature is increased up to 1050 °C the porosity decreased and the sub-micrometre zones are reduced, with the corresponding enlarging of areas of sintered system. At this temperature the grain size were ca. 4 µm and some clear grain boundaries appeared. On further increasing the sintering

temperature up to 1100 °C the grains size reaches value of 6 µm and the sub-micrometric grains areas disappeared. However, the system keeps on having a high degree of inhomogeneity although the porosity was significantly decreased. Finally, for the sample treated at the highest temperature, i.e., 1200 °C, the fracture surface presented well-defined grain boundaries with reduced and extremely localized porosity. In this case, the grain dimensions present a clear polydispersity ranging from 5 – 15 µm. Finally, it should be noted that the grain size growth depicts a linear increase with the sintering temperature revealing the strong correlation between both parameters (Figure 4.18).

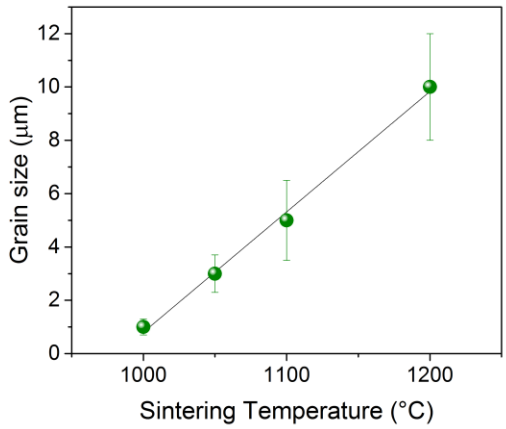

Figure 4.18 : Grain size dependence on the residence temperature during the sintering process. The black straight line is a guide for the eyes.

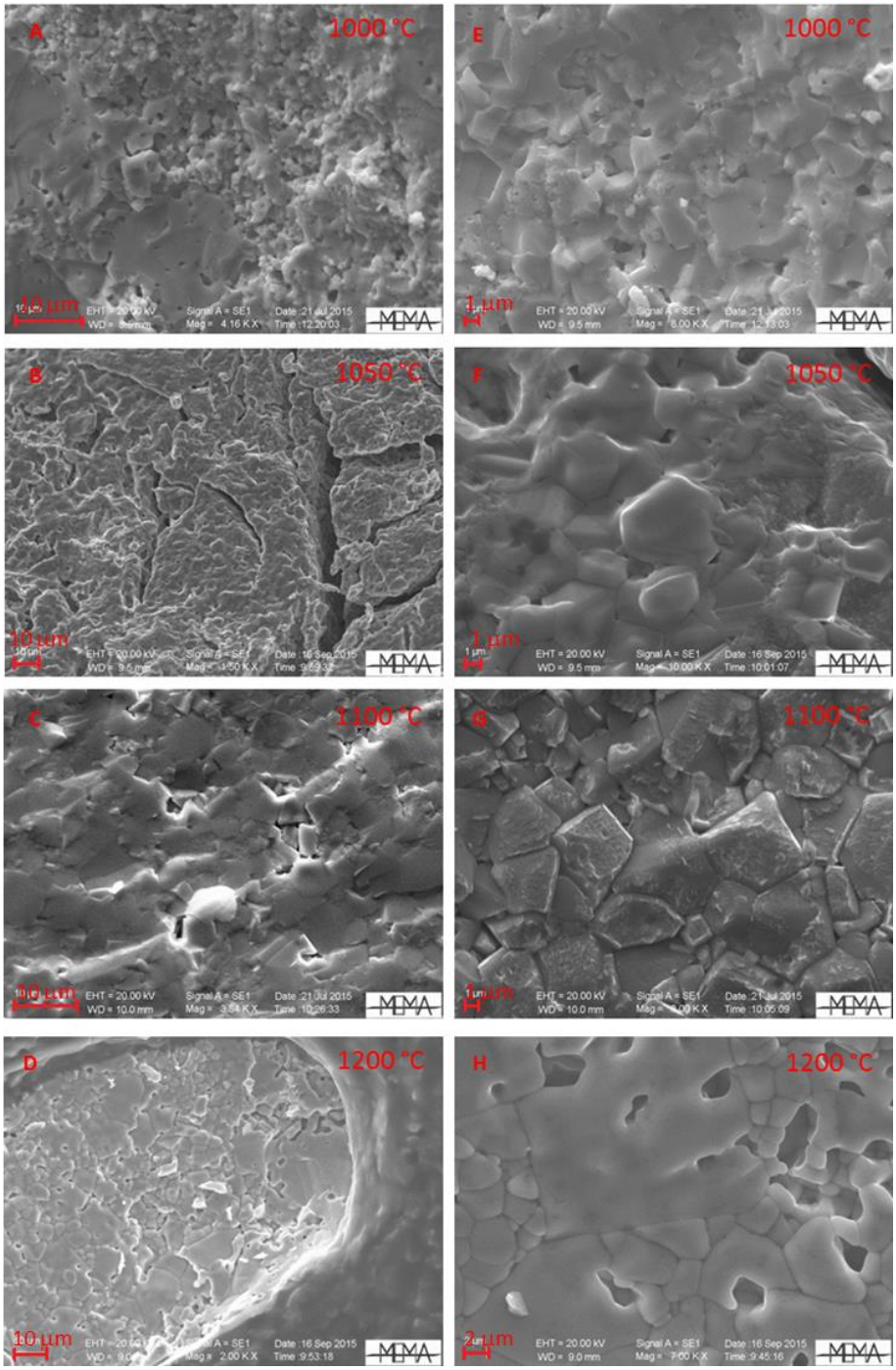

Figure 4.19 : SEM images of surface at the fractures of sintered toroidal samples (**A-D** scale bar = 10 μm; **E – G** = 1 μm, **H** = 2 μm).

Concerning the magnetic properties, as reported in Table 4.1, the saturation magnetization (M_S) of all the sintered samples increased after the heating treatments from 56 emu/g for the as-prepared nanopowders to an almost constant value of roughly 90 emu/g, close to that expected for the bulk Mn, Zn dopes spinel ferrite. The enhancement of M_S values can be ascribed to the increase in crystallization degree and to an increase in the magnetic order. [1] Furthermore, the coercive fields (*Hc*) is almost zero (below the instrumental sensibility), proving the preservation of soft magnetic behaviours. The normalized hysteresis loops of the as-synthesized nanopowder and of the sample sintered at 1200 °C, both recorded at 300K, are shown in Figure 4.20. It is possible to distinguish two clear different approaches to saturation; exhibiting the sintered samples a softer behaviour. These differences can be related to the different effects of the surface of particles and of the grains which, being the surface to core atoms ratio in the nanopowder much larger than in the micrometre powders produced with sintering, it is expected to be less relevant in the latter.

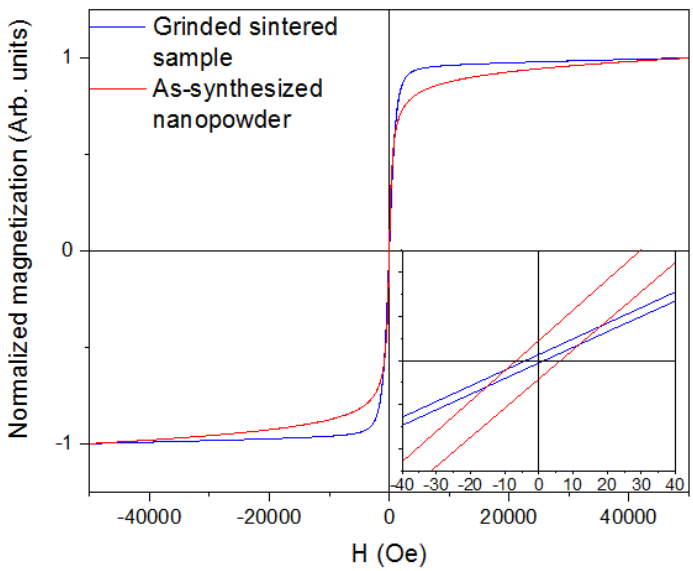

Figure 4.20 : Normalized hysteresis loops for grinded sintered sample (1200 °C) and as-synthesized nanopowder.

In order to evaluate the characteristic of these materials related to the applications envisaged, in this work the relative permeability (μ_r) and core losses at 1, 1.5 and 2 MHz, inducing a magnetic flux *B* of 25 mT were measured. As described in Chapter 3, relative permeability was measured using a Network Analyser in the frequency range between 100 kHz and 10 MHz. The toroidal samples were wound up with 20 turns of 0.2 mm wire and the inductance values were recorded. Then, taking into account the geometry of samples and the number of turns, the relative permeability was evaluated from the inductance values, using Equation 3.2. From the data reported in Table 4.2 a clear trend as the sintering temperature is increased from 1000 ºC to 1200 ºC is observed. In fact, the permeability steadily increases with the sintering temperatures, and, at the same time a marked decreases of the core losses is observed (see Figure 4.21). This behaviour can be ascribed to two different and correlated effects. On one side, the increase in the relative density, which passes from 93% for 1000 °C sample to 98% for the 1200 °C, permits the formation of more compacted structures with lower airgaps which are responsible for the deterioration of the permeability of the system. On the other side, as displayed by SEM images, the presence of more extended and detailed boundaries grains in the sample heated at the highest temperature, associated with a low and localized porosity, favours the increase in the material response to the applied alternating current field, with the corresponding increase in the relative permeability value. Furthermore, the increase on the grain size creates a concomitant reduction of the grain boundaries on the bulk structure decreasing the resistance of the material and therefore the core losses ascribed to the AC current. It is worth to stress that the variation of permeability and core losses with the sintering temperature does not follow a linear trend as it could be argued on the basis of the linear relationship between grain size and temperature. (see Figures 4.19 and 4.21). This result suggests that the trend observed for the two parameters is also

controlled by other physical phenomena. Therefore, it can be concluded that the optimization of the toroidal structures by the classical sintering approach can be accomplished using high sintering temperatures. This effect can be explained in terms of enhancement of the material density and increase of the grain size.

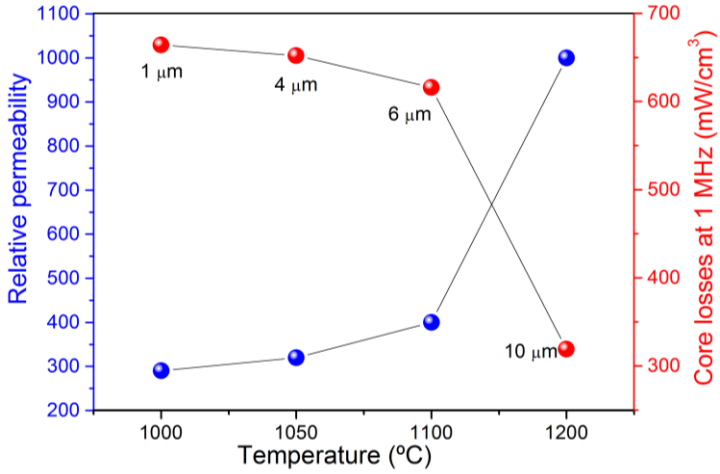

Figure 4.21 : Relative permeability and core losses at 1 MHz as a function of the sintering temperature and grain size.

Table 4.2 : Relative permeability and core loss data of sintered toroidal samples.

Sample	Relative Permeability (μ_r)	Core Loss at 1MHz (mW/cm^3)	Core Loss at 1.5MHz (mW/cm^3)	Core Loss at 2MHz (mW/cm^3)
1000 °C	290	664	1148	1488
1050 °C	320	652	1053	1408
1100 °C	400	616	854	1207
1200 °C	1000	319	603	825

For what concerns core losses measurements, they were performed using the home-made setup described in Chapter 3. In order to measure the toroid samples, the number of wire turns were changed so that the inductance assumed a value close to 7 μH, but not greater, in order to prevent problems with the measuring setup. As expected, the core losses measured at different frequencies decrease as a function of the increased sintering temperature, due to the increase in the relative permeability values.

Overall, the investigation of the properties of samples prepared by the classical sintering approach allowed to confirm the relationship between final density, relative permeability and core losses. Nevertheless, the final properties of the samples are not as satisfying as expected, when compared to commercial products. This result suggests that the simple approach of sintering, using as starting material high crystalline very small nanopowders, it is not a competitive route for the production of cores.
However, there exist still several options to improve the magnetic properties of these materials, some of them actually under investigation. For example by mixing at the nanoscale the initial powder with other components, such a CuO and TiO_2 and/or doping the ferrite with small amounts of high anisotropy divalent ions, can lead to a reduction of the sintering temperature, of eddy currents and hysteresis losses.

4.2.3.2 High Pressure Field Assisted Sintering Technique (HP-FAST)

As an alternative strategy we focused our attention at High Pressure Field Assisted Sintering Technique. Indeed, this approach is able to produce, if properly controlled, high density system, preserving the nanometric structure limiting the growth of the grains below 100 nm. In fact, as described in Chapter

2, one hundred nanometers is the critical size to retain a single domain magnetic structure for most of the ferrite nanoparticles. As it will be more extensively detailed in the Chapter 6, High Pressure Field Assisted Sintering Technique (HP-FAST), is a particular type of Spark Plasma Sintering which involves the use of DC currents to charge the gap between powder particles and allows the sintering of samples at lower temperatures and for much shorter periods. The heating process is generated by Joule effect and, using high intensity currents, it is possible to increase the temperature up to 200 °C/min. At the same time, the application of a high pressure through hydraulic pistons provides high density products preserving the nanometric structure. Therefore, considering that the main goal of this PhD thesis is the fabrication of soft nanostructured magnetic products, HP-FAST seems to be an interesting alternative approach. In order to obtain a toroidal shaped sample, the as-synthesized nanopowders were pressed using a graphite die with 10 mm outer and 4 mm inner diameters. The inner hole was filled with rounded graphite sheet, in order to preserve it after the HP-FAST treatment. Thus the toroids were inserted into a graphite die with 15 mm outer diameter and exposed to the sintering process. Different attempts by varying sintering temperature and pressure as key parameters were performed. Table 4.3 reports the HP-FAST parameters used for some selected experiments as well as the relative density with respect to the bulk one (5.07 g/cm^3), and structural data. During the heating process the heating rate (100 °C/min) and dwell time at sintering temperature (5 min) were kept constants. Sample names refer to the temperature used during the sintering process.

Table 4.3 : Relative density and structural data as function of HP-FAST operative conditions.

Sample	Sintering Pressure (MPa)	Relative density (%)	Lattice Parameter (nm)	Crystal size (nm)
500	77	69.0(2)	0.8467(2)	40(1)
600	68	77.1(3)	0.8464(2)	62(2)
700	71	99.1(1)	0.8466(2)	65(2)
800	74	97.4(1)	0.8468(2)	100(5)
900	92	94.5(1)	0.8470(2)	350(10)
1000	86	96.3(1)	0.8469(2)	1000(50)

We point out that in order to get compact toroids with densities comparable to the bulk, a pressure larger than at least 70 MPa should be applied. In fact, experiments performed using lower pressure (not shown) lead to the formation of fragile toroids. Interestingly, it can be observed from Table 4.3 that as the sintering temperature increases the density of the final product increases, reaching bulk-like values for temperatures since 700 ºC. Therefore in this case bulk-like densities were already obtained operating at sintering temperature of 300 ºC lower than for the classical sintering process, confirming the validity of this approach. Moreover, sintering times were strongly shortened, passing from 6 hours for classical treatment to 5 minutes. As a consequence, the particles sizes increase with sintering temperature is significantly reduced. Indeed, as it can be observed from the XRD data, sintered samples preserve a crystal size in the nanometric range even for temperatures above 800 ºC (Figure 4.22 and Table 4.3)

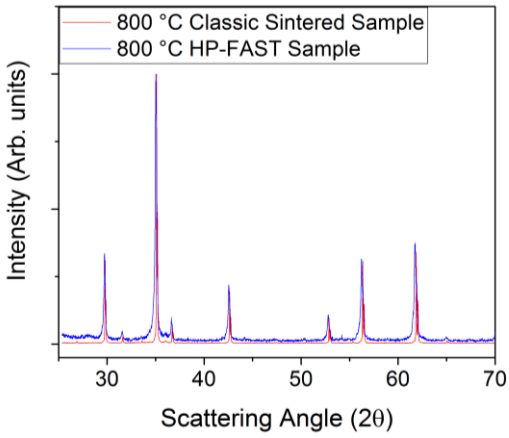

Figure 4.22 : XRD patterns of samples sintered at 800 °C by HP-FAST (Blue) and classic sintering (Red).

The dependence of the particle size calculated from the line broadening of the peaks in the XRD data as a function of the sintering temperature is shown in Figure 4.23. A relatively small size increase is observed for sintering temperature up to 800 °C (ca. 10 times the initial size of as-synthesize nanoparticles). However as the temperature rises an exponential increase of the particle size can be observed, reaching micrometric dimensions at 1000 ºC. From a crystallographic point of view, the cubic spinel structure was always preserved and the lattice parameter value, indicative of the composition was almost equal to the starting nanoparticles, with a value of 0.8467(3) nm. Furthermore, the preservation of the desired composition of the ferrite was confirmed by X-Ray Fluorescence analysis.

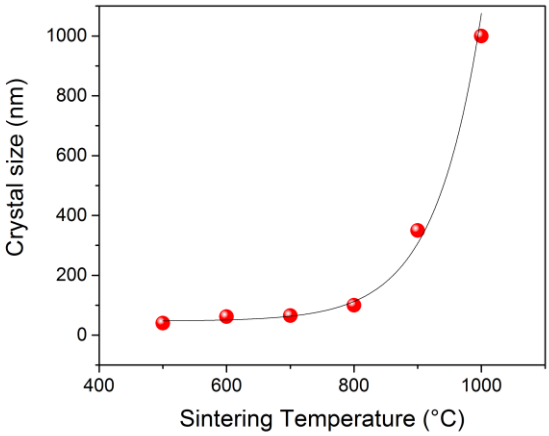

Figure 4.23 : Crystal size increase as a function of the sintering temperature. The black line is a guide for the eyes.

In Table 4.4 are reported the magnetic properties of the HP-FAST sintered samples. The samples sintered at 500 °C and 600 °C present a very low permeability (μ_r <30) due to their very low density. However, samples sintered at temperature above 800 °C also present a very low permeability (μ_r <30); probably, the stress derived from the fast increase in temperature during the HP-FAST process, caused the formation of micro-fractures (air gaps). Moreover, the crystal sizes of these two samples are larger than 100 nm, reaching a value in the micrometer range for 1000 °C sample. Thus, these four samples were not further investigated in core loss test. For samples sintered at 700 °C and 800°C, the relative permeability was 120, lower than that obtained for samples produced by classic sintering. Interestingly, despite of a small difference in saturation magnetization, the two samples exhibited similar core losses at 1, 1.5 and 2 MHz within the error of the measuring instrument (+/- 50 mW/cm^3).

Table 4.4 : Magnetometric and electronic data of interesting HP-FAST sintered samples.

Sample	Ms (emu/g)	Relative Permeability (μ_r)	Core Loss at 1MHz (mW/cm^3)	Core Loss at 1.5MHz (mW/cm^3)	Core Loss at 2MHz (mW/cm^3)
500	69	<30	/	/	/
600	77	<30	/	/	/
700	80	120	1112	1303	1723
800	86	120	1091	1485	1741
900	85	<30	/	/	/
1000	87	<30	/	/	/

In Figures 4.24.a and .b, are compared the permeability and the core loss of two samples obtained by HP-FAST approach with the values of a sample prepared by classic sintering at 1200 °C, which is the one that presented the best performances in term of relative permeability (ca. 1000) and core loss (lower than 1000 mW/cm^3 at 2 MHz). The HP-FAST samples have relative permeability of ca. 120 and core loss larger than 1500 mW/cm^3 at 2MHz. The comparison clearly shows that the classic sintering technique, which provides micro-structured materials, leads to a quasi-bulk dense product with improved performances with respect to the nano-structured ones.

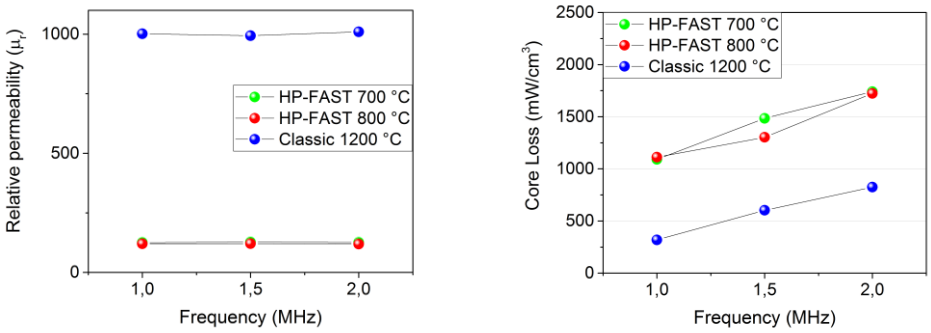

a **b**

Figure 4.24 : **a**) Relative permeability and **b**) core loss as a function of frequency for HP-FAST samples and 1200 °C classic sintered sample.

However, since as described before, a strong instrumental correlation between core loss and relative permeability occurs, in order to properly compare the core loss of micro- and nano-structured materials, two samples with almost the same relative permeability must be selected. In Figure 4.25.a the core loss of a sample classically sintered at 1000 °C, (μ_r=115) are compared to HP-FAST 700 and HP-FAST 800 (μ_r=120). A difference between the two classes of samples emerges with increasing frequency: while at 1 MHz the core losses are almost the same for all the samples, at 1.5 MHz and 2 MHz the classically sintered samples shown core loss increased by 30(9) % and 40(2) %, respectively. A possible explanation could be the extra contribution to core loss arising from classical eddy currents and anomalous losses which, as shown in Figure 4.25.b, largely increase with increasing frequency. Since these contributions scales with the square power of particle diameter, we could expect that they become much more relevant for micro-structured samples. [2]

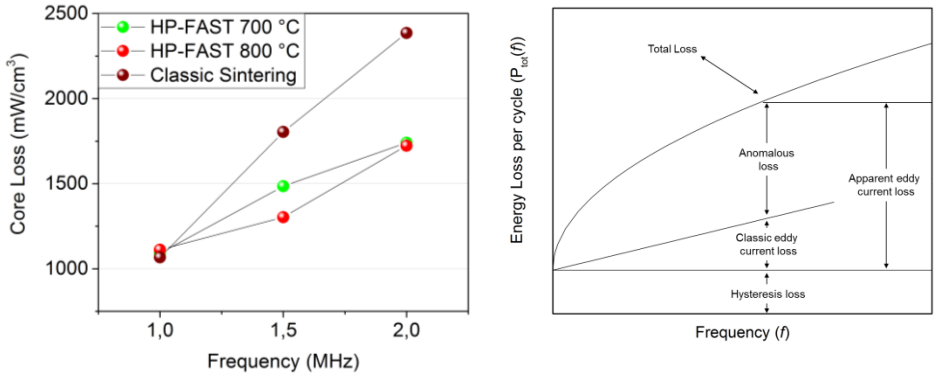

a **b**

Figure 4.25 : **a**) Core loss as function of frequency for HP-FAST samples and a classically sintered sample (T_{sint} = 1000 °C, μ_r=115); **b**) Theoretical dependence on frequency of the different contributions to power losses (Source Ref. [2]).

Although the difficulties in obtaining compacted samples with a toroid geometry limited the use of High Pressure Field Assisted Sintering Technique to few attempts, overall the obtained results suggest this is a very promising technique for the preparation of soft magnetic, highly compacted nanostructured materials but much work is needed to optimize the operative conditions and overcome the observed weak points.

4.3 Moving towards industrial applications

In this PhD thesis, besides the optimization of a synthetic strategy to produce in large scale nanoparticles with soft magnetic behaviour, strong efforts were devoted to face the problems related to obtaining high density toroidal shape products. However, we remind that the choice of a toroidal geometry is imposed by the fact that this is the only shape which allows for the proper evaluation of core losses. However, for many applications this is not a mandatory requirement. Indeed, commercial inductors and transformers present a large variety of shapes, as schematically shown in Figure 4.26.

Figure 4.26 : Some commercial inductors and transformers (Source: http://jestineyong.com/transformer-or-inductor/).

Thus, considering that the properties measured for some of the produced magnetic materials were interesting, we decided to test them on final inductors circuits. Inductor circuits are electronic devices made by magnetic core wound with wires and have the capability to store energy in the form of magnetic energy. Inductors have different shape and size and since the last decades, also different geometry [3] have been developed, always with the aim of reducing core losses associated to the increase of operating frequency.

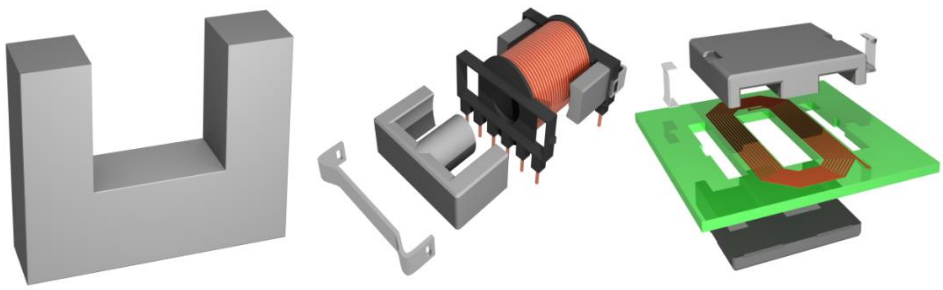

a **b** **c**

Figure 4.27 : Differently shaped magnetic cores for inductor circuits: **a**) U core; **b**) inductor made by two E cores; **c**) inductor made by planar E cores.

If U cores are taken in consideration, an inductor can be assembled by coupling two cores, with the formation of an UU magnetic core, which can then be wound with electric wires. This UU inductor can be schematized as two parallel plates connected by two legs (Figure 4.28), with wire turns over the plates.

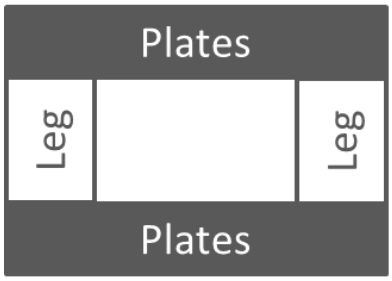

Figure 4.28 : Scheme of a UU core.

Since these results are at present under patent, only a rough description will be provided in the following. In brief, an inductor was prepared using two parallel plates of a commercial ferrite and different legs were tested: one couple made by commercial ferrites and two couples prepared using two different magnetic sintered pieces prepared in this thesis. The assembled system was exposed to an increased pressure, comparable to the one applied in the fabrication process. The results for conventional legs and our products, in terms of percentage shift of inductance and core loss, are shown in Figure 4.29.a and .b.

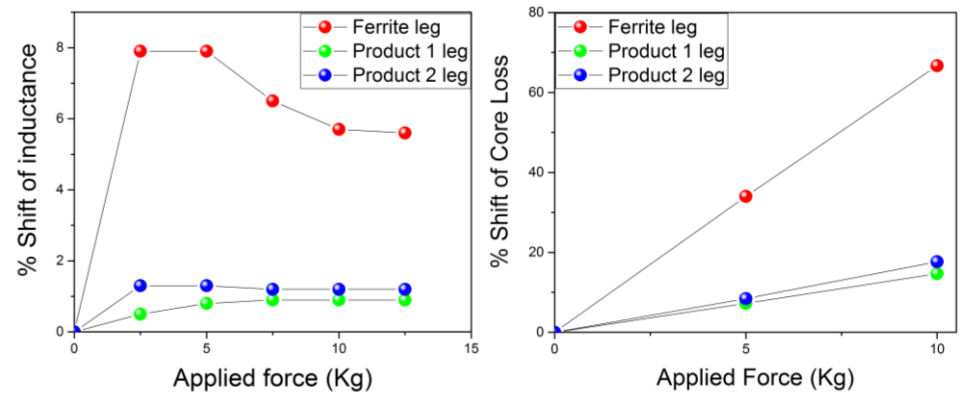

a **b**

Figure 4.29 : **a**) Percentage shift of inductance and **b**) Percentage shift of the core loss as a function of the applied force.

These results show that as the applied force increases, commercial ferrite legs present an increase of the inductance value of 8% and a simultaneously increase of core loss up to +70% for 10 Kg applied. Conversely, both our product legs present a very small increase of inductance (ca. 1%) and of core loss (+15%). Most importantly the core losses of the powder samples at the highest applied force are smaller than those of the commercial legs. These results are very interesting both in terms of inductance and core loss. In fact, considering the design of new inductors, a small variation of inductance with

pressure, and core losses as much lower as possible are two fundamental requirements. Thus, on the basis of these results we can conclude that our magnetic pieces are extremely promising for this kind of applications.

References

[1] K. Praveena, K. Sadhana, and H. S. Virk, “Structural and Magnetic Properties of Mn-Zn Ferrites Synthesized by Microwave-Hydrothermal Process ,” *Solid State Phenom.*, vol. 232, pp. 45–64, Jun. 2015.

[2] B. D. Cullity and C. D. Graham, *Introduction to Magnetic Materials*, Second Ed. Wiley-IEEE Press, 2011.

[3] “https://en.wikipedia.org/wiki/Magnetic_core.” .

Chapter 5

Conclusions and perspectives

The experimental work presented in this PhD thesis is focused on the synthesis of doped spinel ferrite-based, nanostructured materials with soft magnetic behaviour and on the translation of the nanostructure properties upon processing of the powders to high density final products. Micrometric materials with soft magnetic behaviour found extensive use in the industry for the fabrication of electronic devices, such as inductors and transformers. These types of devices are composed by soft magnetic cores inserted in electric circuits, working both in direct current and alternating current. The effective use of these electronic devices is strongly related to the efficiency in the process of conversion from electric to magnetic energy and in the control of these phenomena, reducing the dissipation of energy as heat and, in this way, the power losses associated to the conversion process itself. The present work moves within this contest, as it explores the design and development of nanostructured materials for high frequency soft electronic device applications, with the aim to reduce power losses at increased frequency respect to those currently used.

This challenge has been tackled operating both on the intrinsic soft magnetic properties of the materials, improved thanks to the size reduction at the nanoscale, and on the propagation of eddy-currents, proportional to the

square radius of the grains. Indeed, initial efforts were focused on the optimization of a synthetic strategy able to produce highly crystalline nanopowders, with controlled sizes (ranging from 7-10 nm) and compositions (manganese, zinc, nickel doped iron oxide), through a cheap, eco-friendly and facile methodology, suitable for an easier hypothetical industrial scale-up. Thus, co-precipitation method was chosen and improved as the synthetic strategy. Starting from aqueous solutions of transition metal chlorides, through a precipitation in basic media, highly crystalline nanoparticles with tuneable composition were produced. Structural and chemical (X-ray diffraction and X-ray fluorescence), morphological (transmission and scanning electron microscopies) and physical (magnetometric measurements) characterizations were carried out and the soft magnetic behaviour was confirmed.

The determination of relative permeability and core losses on nanopowders with different composition –and thus different magnetic behaviours, required the development of a specific methodology and of the relative instrumentation. To this aim, the nanopowders were compressed into macroscopic toroidal shapes and characterized. The obtained results, i.e. low relative permeability and high core losses, showed how these magnetic properties are strictly related to the low density reached during the preparation of samples, compared to the bulk one.

Based on these results, considerable efforts were focused on increasing the relative density of the final products. Since for relative permeability and core losses measurements, the sample must have a toroidal shape, an improved die for the compaction of nanopowders in the suitable shape was designed and fabricated. This process turned out to be problematic, due to the nanometric nature of the powder; in fact, a classical approach with very low tolerance between die components is not possible because permeation of nanopowders

in the die is always present. Once obtained the green toroids, i.e. not exposed to sintering, in order to enhance the final density,, two strategies were explored: a classical heat treatment in a tubular furnace and a sintering technique driven by Joule effect (High Pressure Field Assisted Sintering Technique, HP-FAST) The first method, starting from pressed green toroid, allowed the attainment of micrometric structured toroids with a quasi-bulk density; the second one yielded nanostructured toroids with similar quasi-bulk density (ca. 95(5) %).

In the classical sintering process, large efforts were devoted to the optimization of the sintering parameters, focusing on the temperatures which allowed the complete densification of the samples. The investigation of the magnetic properties of samples prepared by the classical sintering approach allowed confirming the relationship between final density, relative permeability and core losses. Nevertheless, the final properties of the samples were not satisfactory, when compared to commercial products. This result suggests that the simple approach of sintering, using as starting material highly crystalline nanopowders, is not a competitive route for the production of cores. Notwithstanding these results were not fully positive, a significant improvement of the properties of materials obtained by this route, can still be envisaged. Indeed, there are still several options, some of them currently under investigation, which in principle can lead to an enhancement of the characteristic of the materials. For instance, mixing at the nanoscale the initial powder with other components, such a CuO and TiO_2 and/or doping the ferrite with small amounts of high anisotropy divalent ions, can lead to a reduction of the sintering temperature, of eddy currents and hysteresis losses.

As mentioned above, the second method to prepare the nanostructured toroids, High Pressure Field Assisted Sintering Technique, was investigated. Green toroids were sintered by exploiting the heat produced by Joule effect,

applying a high intensity DC current to a non-conductive die containing the powders and simultaneously applying a uniaxial pressure. Variable sintering temperature and applied pressure were explored, to obtain nanometric structured products. The as-obtained toroids presented lower relative permeability compared to classical sintered ones and, thus, higher core losses. However, comparing the nanostructured products with classically sintered ones with the same relative permeability, low frequency core losses were found to be very similar and, at higher frequency, core losses were even lower, suggesting a reduction of the extra loss contribution arising from classical eddy currents and anomalous losses. Indeed, since these contributions scale with the square power of particle diameter, we could expect that they become much more relevant for micro-structured samples. Unfortunately, difficulties in obtaining samples with toroidal geometry limited the investigation of High Pressure Field Assisted Sintering Technique to few attempts. However, the obtained results suggest that this is a very promising technique for the preparation of soft magnetic, highly compacted nanostructured materials, even if much work is still needed to optimize the operative conditions and overcome the observed weak points.

The choice of a toroidal shape is strictly related to the measuring technique but, for many applications, this is not a mandatory requirement, as evidenced by the fact that commercial inductors and transformers present a large variety of shapes. Considering that the intrinsic magnetic properties of some of the magnetic materials prepared in this work were interesting, we decided to test them as a constituent of an inductor prototype and compared to commercial products. Since during the assembling of the inductor in the industrial process, the material undergoes a high pressure due to the shrinkage of assembling procedure, core losses were measured by applying a similar external pressure. The obtained results showed that, on increasing the applied pressure, the products prepared in this Thesis present a less marked variation of inductance

and core losses and, most importantly, their power losses at high pressure are lower than those of commercial products. Although still preliminary, these results demonstrate that the proposed approach is extremely promising to prepare a novel class of materials with higher efficiency compared to commercial products, when used to build up electronic devices working at high frequency (above 2 MHz). Indeed, the application of one compound prepared in this Thesis in an electronic device, will be patented soon, while the scale up of its laboratory synthesis to the industrial scale production is currently in progress, and hopefully the product will enter the market on a short time scale.

Chapter 6

Experimental Techniques

6.1 Electron Microscopy Techniques.

Microscopy electron based techniques are one of the most useful and powerful methods to investigate the nanoscale. They operate on the same basic principles as the light microscope but use electrons instead of light. Wavelength of light is the limitation for optical microscope; using electrons as "light source" with a much lower wavelength, make it possible to get a resolution a thousand times better than with a light microscope, in the order of few nanometers. Electron microscope is composed by three essential systems:

- an electron gun, which produces the electron beam, fitted with a Tungsten (W) or Lanthanum hexaboride (LaB_6) filament cathode. Tungsten is normally used in thermionic electron guns because it has the higher melting point and lowest vapor pressure, compared with other metals, and because of its low cost.
- an electron column under high vacuum, where are hold the condenser lens which allow the electron beam focus on samples.

- an image record system or an electron detector, depending on the microscope type.

Electron microscope can be discriminate by the sample interaction with the electron beam. Indeed, the beam can be transmitted or reflected by the specimen. Evidently, for different beam interaction with sample, it is needed a different structure of the column.

On this base is possible to differentiate between:

- *Transmission Electron Microscope (TEM)*
- *Scanning Electron Microscope (SEM)*

6.1.1. Transmission Electron Microscope (TEM).

In TEM, electrons are emitted from the electron gun, the beam is driven by different magnetic lens crossing the sample and, finally, the image is viewed on a screen or CCD camera (Figure 6.1). [1]

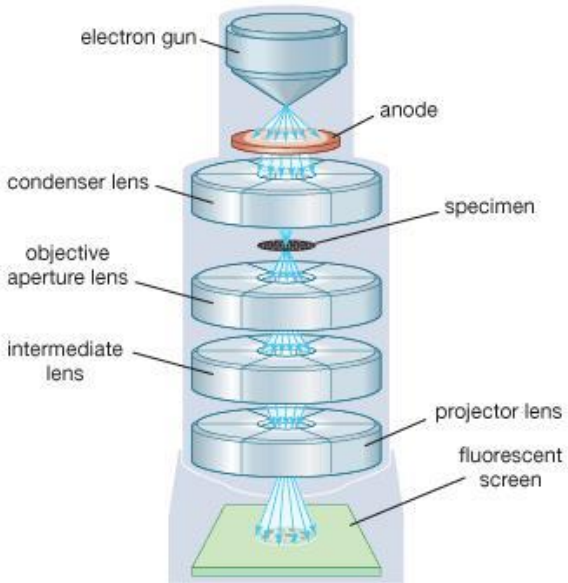

Figure 6.1 : TEM operating structure

Below the electron gun there are two or more condenser lenses. These lenses demagnify the beam emitted by the gun and control its diameter as it hits the specimen. An aperture is present between the condenser lenses (the condenser aperture) which can be used to control the convergence angle of the beam. In a simple view, the condenser controls can be thought as brightness controls, although, in fact, they permit a wide range of control over the region of the specimen. Below the condenser lies the specimen chamber. After this chamber are placed the objective lenses, with the role to form the first intermediate image, which is enlarged by subsequent projector lenses and displayed on the viewing screen. Nowadays CCD cameras are used to record images in electron microscopies. Combining the output signal/image with a camera and a computer which has image processing software and controls of the microscope lenses, it is now possible to perform some alignment procedures quickly and automatically. The images obtained by transmission electron microscopy allow characterizing the shape and size of the nanoparticles. For spherical particles the measurement of large number particle diameters gives information about the particle size distribution.

The TEM images were acquired using a CM12 Philips microscope, equipped with a LaB_6 filament operating at 100kV. The Transmission electron microscopy experiments were carried out using the instrument of Centro di Microscopie Elettroniche (CE.M.E.).

6.1.2. Scanning Electron Microscope (SEM).

In SEM, electrons interact with atoms of samples, producing various signals that contain information about the surface topography and composition. The electron beam is generally scanned in a raster scan pattern and the beam's

position is combined with the detected signal to produce an image. SEMs work in scanning mode and it is possible to analyze few micrometer of a bulk samples surface with very high resolution. Furthermore, in SEM it is possible to detect back scattered electrons that allow to have information about samples composition.

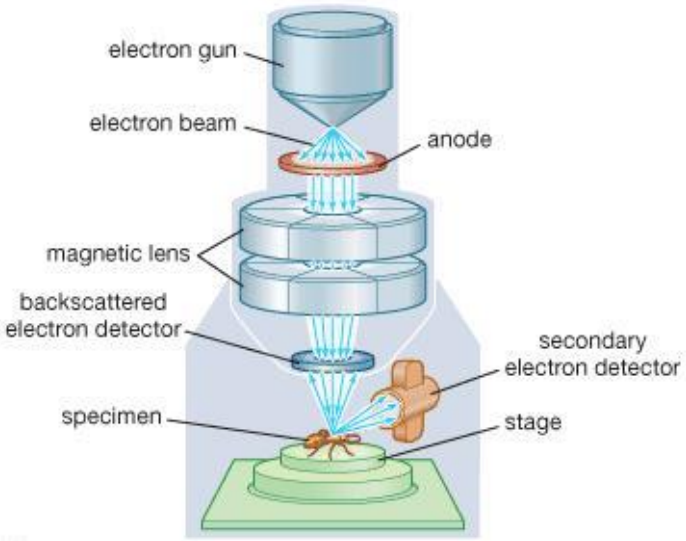

Figure 6.2 : SEM operating structure

In a typical SEM (Figure 6.2), [2] the electron beam, whit an energy ranging from 0.2 keV to 40 keV, is focused by two condenser lenses to a spot with a diameter between 0.4 nm to 5 nm. The beam passes through pairs of deflector plates in the electron column, then to the final lens which deflect the beam in the *x* and *y* axes, allowing a raster scan over a rectangular area of the sample surface with a magnification from 10 to 500k times. When primary electron beam interacts with the sample, the electrons lose energy by scattering and absorption within a volume of the specimen (interaction volume). Interaction volume extends from less than 100 nm to 5 µm into the surface, depending on electron's landing energy, sample’s atomic number and specimen's density.

The energy exchanged between electron beam and sample determines:

- reflection of high-energy (>50 keV) electrons by elastic scattering,
- emission of secondary electrons (low energy, <50 keV) by inelastic scattering.

The signals, amplified by different electronic amplifiers, are displayed as variations in brightness on a computer monitor.

The most common imaging mode collects secondary electrons that are ejected from the K-shell of the specimen atoms by inelastic scattering interactions with beam electrons. Due to their low energy, these electrons originate within a few nanometers from the sample surface and are detected by an Everhart-Thornley detector, a type of scintillator-photomultiplier system. Backscattered electrons (BSE) consist of high-energy electrons originating in the electron beam, which are reflected out of the specimen interaction volume by elastic scattering interactions with specimen atoms. Since heavy elements (high atomic number) backscatter electrons more strongly than light elements (low atomic number), BSE are used to detect contrast between areas with different chemical compositions. Dedicated backscattered electron detectors, usually either of scintillator or of semiconductor types, are positioned above the sample. When all parts of the detector are used to collect electrons symmetrically about the beam, atomic number contrast is produced.

To the scanning electron microscope it is possible the coupling to an X-ray spectroscope that allows the surface ions mapping. The characteristic X-rays produced by the interaction of electrons with the sample may be detected in a SEM equipped with an energy-dispersive or wavelength dispersive X-ray spectroscope. Analyzing the X-ray signals it is possible to map the distribution and estimate the abundance of different elements in the sample.

The SEM images were acquired on fracture surface of sintered samples, using a Zeiss EVO MA15 microscope, equipped with an Oxford INCA 250 for microanalysis. The Scanning electron microscopy experiments were carried out using the instrument of Centro di Servizi di Microscopia Elettronica e Microanalisi (MEMA).

6.2 X-Ray based techniques.

X-radiation, composed by X-rays, is an electromagnetic radiation having a wavelength range from 0.01 to 10 nm, corresponding to energies in the range 0.1 to 100 keV, shorter than those of UV-rays and typically longer than those of gamma rays. X-rays with photon energies above 5–10 keV (below 0.2–0.1 nm wavelength) are called hard X-rays, while those with lower energy are called soft X-rays. Since the wavelengths of hard X-rays are similar to the size of atoms they are useful for determining crystal structures by X-ray crystallography. This type of radiation can be scattered or absorbed by the matter and, on this two phenomena, it possible to discriminate two different techniques:

- *X-ray diffraction*
- *X-ray fluorescence*

6.2.1. X-ray diffraction (XRD).

In classical physics, the diffraction phenomena is described as the apparent bending of waves around small obstacles and the spreading out of waves past small openings. Diffraction occurs with all waves, including sound waves, water waves, and electromagnetic waves such as visible light, X-rays and radio waves. As physical objects, at the atomic level, have wave-like properties. Diffraction also occurs with matter and can be studied according to the principles of quantum mechanics. Considering that diffraction occurs when propagating waves find small objects, its effects are generally most pronounced for waves whit a wavelength roughly similar to the dimensions of the diffracting objects. If the obstructing object provides multiple, closely

spaced openings, a complex pattern of varying intensity can result. This is due to the superposition, or interference, of different parts of a wave that traveled to the observer by different paths. XRD is a versatile, non-destructive technique that reveal detailed information about the chemical composition, physical properties and crystallographic structure of matter.

6.2.1.1. Bragg's law.

Diffraction phenomenon is described by the Bragg's law, which gives the angles for coherent and incoherent scattering from a crystal lattice exposed to an X-ray beam. Assuming that an incident wave beam is perfectly collimated and monochromatic (with a single wavelength λ) and makes an incident angle θ with respect to the reticular planes of the crystal, it can be demonstrated that the following condition is fulfilled:

$$n\lambda = 2d_{(hkl)}\sin(\theta) \qquad 6.1$$

if n, the reflection order, is a integer number (beam is completely in phase and give constructive interferences), and $d_{(hkl)}$ is the inter-planar distance of one family of (hkl) crystallographic planes. This condition is schematically represented in Figure 6.3 and it can be used to determine the angular positions of the diffraction peaks diffracted by each family of planes.

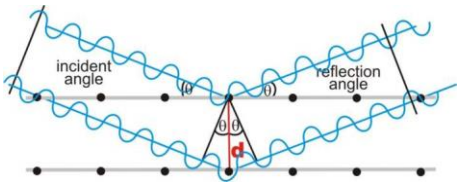

Figure 6.3 : Representation of Bragg's law.

Also, $d_{(hkl)}$ can be understood as a geometric function of size and shape of a unit cell for a diffracted crystallographic structure. As can be seen in Bragg equation (Eq. 6.1) for a simple cubic crystallographic structure $d_{(hkl)}$ for a specific (hkl) planes can be related to the cell parameter a. [3], [4]

$$d(hkl) = \frac{a}{\sqrt[2]{h^2 + k^2 + l^2}} \qquad 6.2$$

XRD is based on the observation of the scattered intensity of an X-ray beam hitting a sample as a function of incident and scattered angle, polarization, and wavelength (energy). When an X-ray beam encounters an atom, each electron in it scatters part of the radiation. Coherent scattering is due only to the electrons because the interaction with the nucleus is weak, due to the extremely large mass of nucleus compared to the electrons ones. Therefore, the wave scattered by an atom is the simply sum of the waves scattered by its electrons in the forward direction (2θ = 0). This is not true for other directions of scattering. Since the electrons of an atom are situated at different points in space, differences in phase between the waves scattered by different electrons are generated.

6.2.1.2. Diffraction peaks intensity.

The measured diffraction pattern includes information about peak positions and intensity. The position of diffraction peaks and the corresponding $d_{(hkl)}$ provide information about the location of lattice planes, the crystal structure and the symmetry of contributing phase. Each peak measures a d-spacing that represents a family of lattice planes $d_{(hkl)}$. Moreover, each peak also has a fixed intensity related with the most intense one, which differs from other peaks in the pattern and reflects the relative strength of the diffraction. An accurate measure of intensity relationships in a pattern is obtained by measuring the area (subtracted background) under the peaks. Peak intensities have been

calculated theoretically for most crystal structures and comparing the experimental peak intensity to the theoretical one allows determining the diffracting material phase.

6.2.1.3. Peak shape function.

Bragg's law assumes that the crystal is ideal (without structural defects) and the incident beam is perfectly monochromatic and collimated but, experimentally, these conditions are never fulfilled completely. Moreover, usually, the particles are found to be composed by several crystallites with different orientation and with certain amount of defects. The size of these crystallites and the microstrains present in them can also be obtained from the diffraction pattern, [3] since both effects contribute to the width of the diffraction peaks. The peak shape function, $H(\Delta 2\theta)$, of conventional materials can usually be fit by a simple Gaussian function (*Gf*). However, when crystallite size drops less than 100 nm or large strains are present, a deviation of the shape occurs from pure Gaussian to a mixture of Gaussian and Lorentzian function (*Lf*), also referred to as a pseudo-Voigt function (*Vf*), that allows the separation of the *Gf* and *Lf* contributions to the peak shape function.

$$H(\Delta 2\theta) = Vf = \eta\, Lf(\Delta 2\theta, X, Y) + (1 - \eta)\, Gf(\Delta 2\theta, U, V, W, P) \qquad (0 \leq \eta \leq 1) \qquad 6.3$$

where η is the variable proportion between *Gf* and *Lf* functions, X and Y are the variables of the *Lf* function and U, V, W and P are the variables of the *Gf* function.

The full width at half maximum (FWHM) contributions for the Gaussian and Lorentzian functions is instrumental and specimen broadening, respectively. The dependence of the specimen broadening on θ usually exhibits a $X*(1/\cos\theta) + Y*(\tan\theta)$ dependence, where the coefficients X and Y can be

directly associated with the crystallite size and microstrain, respectively. Then using this formalism, the crystallite size *d* can be easily estimated from the Lorentzian contribution to the FWHM of each diffraction peak, as given by the Scherrer equation:

$$d = \frac{K_\alpha \lambda}{(FWHM)_i cos\theta_i} \qquad 6.4$$

where K_α is a constant dependent on the crystallite shape and λ is the incident wavelength. [3] Gaussian contribution (G*f*) that is associated with the instrumental broadening, can be calculated measuring standard samples, e.g., LaB_6, which present sufficiently large crystallite sizes and negligible stress values to avoid the presence of the *Lf* function in peak shape refinement.

6.2.1.4. Rietveld refinement.

The Rietveld method is used to fit the experimental diffraction patterns by considering the instrumental contribution, assuming a certain crystal structure and adjusting different structural parameters, such as atomic displacements, anisotropy and microstrain. The chosen parameters are adjusted in an iterative process until convergence is reached between the values of the experimental intensities and the theoretical model. Different programs which use Rietveld method, such as Topas [5] and MAUD [6], are available. The function minimized in the refinement of the diffracted pattern by the Rietveld method is the residue, S_I , which is defined as:

$$S_I = \sum_i \omega_i (I_i - I_{calc})^2 \qquad 6.5$$

In this equation, $\omega_i = 1/I_i$, I_i is the experimental intensity for the *i* step and I_{calc} is the calculated intensity for the same *i* step and takes count of different samples and measuring characteristic, such as scale factor, peak shape function, absorption factor and preferred orientation factor

6.2.1.5. Powder X-ray diffraction, PWXRD.

X-ray powder diffraction (PWXRD) is a rapid analytical technique used for phase identification of a crystalline material and can provide extrapolated information on lattice parameter and crystal size. For example, the analysis of the peak position and their intensity provide the types of phases present in the samples and their relative amounts. Another important piece of information, obtained from the analysis of the peak width and shape, is the crystallite size and the microstrains. In certain cases, the relative intensity of different peaks of the same phase also supplies further information about the atomic relative percentage, i.e. vacancies.

The X-ray diffractograms were obtained on loosely-packed powdered samples using a Bruker Advantage D8 diffractometers equipped with Cu Kα radiation using a Bragg-Brentano geometry. The measurements were carried out in the 25-70 º 2θ range with a step size of 0.02 º and collection time of 0.5 s. In all diffraction patterns, Rietveld refinement and peak shape analysis were carried out using the Topas and MAUD programs.
The powder XRD experiments were carried out using the diffractometer of Centro di Cristallografia Strutturale (Crist) of the Dipartimento di Chimica “Ugo Schiff” of Università degli Studi di Firenze.

6.2.2. X-ray fluorescence (XRF).

X-ray fluorescence is a non-destructive technique, used for elemental and chemical analysis, in the investigation of metals, glass and ceramics materials. It is based on the emission of a characteristic secondary (fluorescent) radiation from a material that has been excited by a primary X-ray wave. [7] When an X-

ray is focused on a material, a sufficient photon energy can be absorbed by an electron and the electron can be dislodged from one of the atomic inner shells (K, L or M). This removal makes the atomic electronic structure unstable. The atom fills the vacant shell with an electron from the higher energy shell and, as the electron drops to the lower energy state, excess energy is released in the form of a photon. This energy is equal to the energy difference of the two orbitals involved and it is distinctive for each element of the periodic table (Figure 6.4).

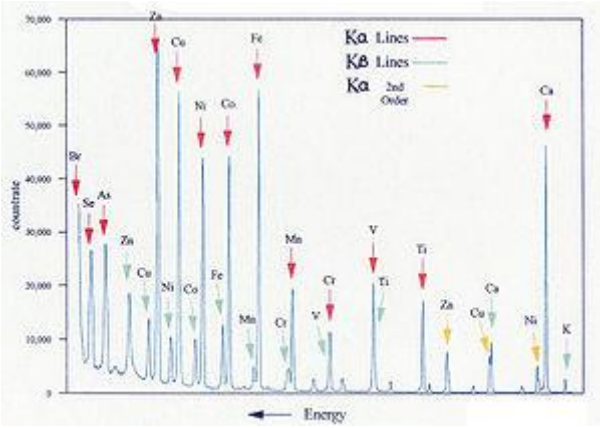

Figure 6.4 : Transition energy of different elements of the periodic table.

Each element has electronic orbitals with a characteristic energy. As described, when an inner electron is expelled by an energetic photon provided by a primary radiation source, an electron from an outer shell drops into its place. There are a limited number of ways in which this can happen and the main transitions are:

- L → K transition called K_α,
- M → K transition called K_β,
- M → L transition called L_α

Each of these transitions yields a fluorescent photon with a characteristic energy equal to the difference in energy between initial and final orbital. The wavelength of this fluorescent radiation can be calculated from the Planck's Law:

$$\lambda = \frac{hc}{E} \qquad 6.6$$

The emitted radiation can be analyzed either by sorting the energies of the photons, energy-dispersive analysis, or by separating the wavelengths of the radiation, wavelength-dispersive analysis.

XRF instrument is mainly composed by an X-ray source close to the sample holder and a revelator (energy or wavelength detector) connected with the signal processor system, which allows converting spectral data to easy analytical results.

6.2.2.1. X-ray source.

Conventional X-ray generator is a source of radiation with a tunable energy sufficient to expel tightly held inner electrons of different atoms. Source is constituted of a filament (cathode), usually Tungsten (W), which is excited by a properly current (mA) and emits electrons. The electrons, hitting a tube (anode), usually Rhodium (Rh), determine emission of photons in the range of 20-60 kV, which, hitting the sample, excite a broad range of atoms. On the Rhodium tube is applied a difference tension (kV), in order to tune the electrons acceleration. Maximum potential, derived from the product between current and tension, is usually lower than 4 kW.

6.2.2.2. Dispersion and detection.

The fluorescent radiation can be selected and detected through two different techniques:

- energy dispersive analysis:
  fluorescent X-rays emitted by the sample are directed into a solid-state detector (PIN diode, Si(Li), Ge(Li), Silicon Drift Detector SDD) which produces a "continuous" distribution of pulses. Voltages of these pulses are proportional to the incoming photon energies. The spectrum is then built up by dividing the energy spectrum into discrete bins and counting the number of pulses registered within each energy bin, obtaining the analytical data.

- wavelength dispersive analysis:
  fluorescent X-rays emitted by the sample are directed into a wave splitter, usually a single crystal. Detector is mounted on a goniometer and varying the goniometer angle is possible to select different X-ray wavelength, in accord with the Bragg Equation. The wave is then focused into a photomultiplier, which allow counting of individual photons by gas ionization.

The XRF analyses were carried out on powders, using a Rigaku Primus II, equipped with a Rh Kα radiation source and a wavelength dispersive detector. XRF experimental data was also confirmed by ICP analyses. The X-ray fluorescence experiments were carried out using the instrument of Centro di Cristallografia Strutturale (Crist) of the Dipartimento di Chimica “Ugo Schiff” of Università degli Studi di Firenze.

6.3 Physical Properties Measuring System (PPMS).

The principle aim of magnetometry is to measure the magnetic response of a material when it is inserted in an external magnetic field. This can be achieved in a large number of ways, using various magnetic phenomena. Magnetometers can be classified as AC types, which measure using fields that vary relatively rapidly in time, and DC types, which measure in quasi-static fields. In this thesis, the magnetometric measures were carried out under DC current, using a physical property measurement system (PPMS) of Quantum Design Inc. [8] This instrument works on the principle of the Faraday law: a closed circuit is traversed by current if subjected to a time-varying magnetic field flow. In order to perform measurement, a sample is moved in a homogeneous magnetic field produced by a superconductive coil. This movement induces a magnetic flux time variation proportional to the magnetic moment of the sample, which can be measured by inducing a current in the detection coil. In a typical magnetometer, sample is introduced in a liquid Helium cryostat. A vacuum gap (10^{-6} bar) around the measuring chamber produces a thermal isolation from the surroundings. The measuring chamber and the He bath are in communication by a thin capillary and the incoming flux is regulated by an external pump. This device, coupled with a heater located near the sample, controls the temperature during the measurement. Moreover, thanks to a pumping system on the sample chamber it is possible to reach temperature lower than the boiling point of He^4 (4.2 K), ranging from 1.9 K to room temperature. The He bath has also the function to keep the magnet and the measuring device in the superconductive regime. Temperature is monitored by two GaAs diode thermometers; the first one is placed close to the sample, near the gradiometer, while the second one is used for software automatic control of temperature and it is placed near the heater, which

produced the desired temperature settings. The sensitivity of those thermometers allows to appreciate temperature variations up to 0.001K.

Measurements were carried out in DC-field, using a Vibrating Sample Motor (VSM), and can be summarized in two main types of studies:

- the temperature dependence of the magnetization, M(T)
- the field dependence of the magnetization, hysteresis loop, M(H).

M(T) measurements were performed using two different approaches:

1. Zero-field cooling (ZFC), where the samples were cooled without any field applied at low temperature (10K) and when the desired T was reached, a small magnetic field (50 Oe) was applied and, then, the temperature was increased (300K) and the magnetization measured continuously;
2. Field cooling (FC), where the sample is cooled in the presence of a small external magnetic field (50 Oe) and the magnetization is measured during stepwise warming in the same applied field.

Usually, both measurements are plotted together as a function of temperature. From this representation we can extract the magnetic transition temperatures such as T_C, T_N or T_B. From the shape of the curves, indirect qualitative information of, for example, inter-particle dipolar interactions or particle size distribution can be obtained.

M(H) measurements were performed cooling the samples to the desirable temperature in a FC or ZFC procedure. Then the sample was magnetically saturated with a positive high field (+ 50 kOe). Then, the magnetization is measured while decreasing the field until the opposite, negative, saturation (-

50 kOe) was reached. Finally, the magnetization was measured increasing field back to positive saturation. This process was performed at room temperature (300 K). However, for more specific analysis some samples were analyzed at different temperatures from 10 to 300 K. The shape and size of the hysteresis loop allowed us to determine magnetic characteristics of the samples, such as coercive field *(Hc)*, remnant magnetization (M_R) and saturation magnetization *(M_S)*.

Experiments were carried out by measuring the magnetic moment of the sample (i.e., emu in cgs units) and scaled to the mass of the sample to obtain the magnetization (i.e., emu/g). The powder sample, in a weight range of 1-10 mg, was tightly packed in a Teflon film and pressed, to avoid its movement due to high magnetic fields.

The DC-magnetic measurements were carried out using the PPMS magnetometer of Laboratory of Molecular Magnetism (LAMM) of the Dipartimento di Chimica “Ugo Schiff” of Università degli Studi di Firenze.

6.4 High Pressure-Field Assisted Sintering Technique (HP-FAST)

High pressure Field Assisted Sintering is a particular type of Spark Plasma Sintering (SPS). [9] SPS is a process which allows the powder sintering at low temperatures and short periods by charging the gap between powder particles with electrical energy and effectively applying high temperature spark plasma generated momentarily. Using self-heating action from inside the powder, due to high intensity current, it is possible to increase the system temperature very fast (over than 200 °C/min), and decrease, in this way, sintering times and limit diffusion process that are responsible for grain growth.

The HP-FAST combines the sintering characteristic of SPS with a particular uniaxial pressure system which allows to reach 1 GPa of pressure and further decrease sintering temperature and grains growth. The pressure system, insert into a vacuum chamber (1 torr), consists in two uniaxial graphite press, one insert between the other one, and it allows to hugely increase the effective pressure on sample. The pressure on the external cylinder is 1/144 of the internal one. This system can reach on a 1 mm diameter sample more than 750 MPa.

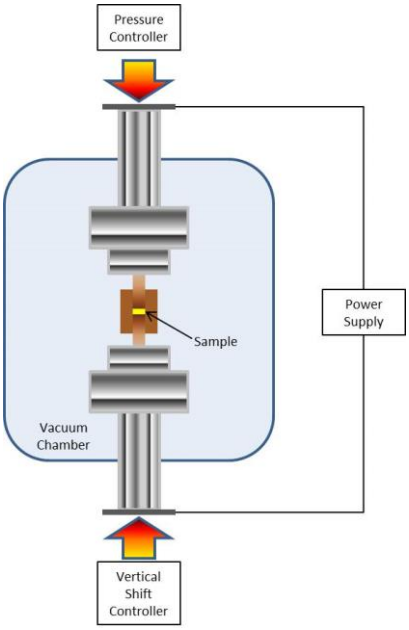

Figure 6.5 : HP-FAST schematic structure.

Sintering process is continuously monitored, in order to fine control temperature, pressure, vertical shift, current voltage and intensity (Figure 6.6).

HP-FAST processes were carried out after preparing a green toroid with low pressure uniaxial press. To prevent the hole occlusion was inserted rolled graphite sheet in the hole. Green toroids were then insert in the graphite mold and exposed to an HP-FAST sintering, using temperature in the range 500-1000 °C and pressure in the range 68 - 92 MPa. After cooling, the graphite sheet was eliminated and returned a toroid like shape.

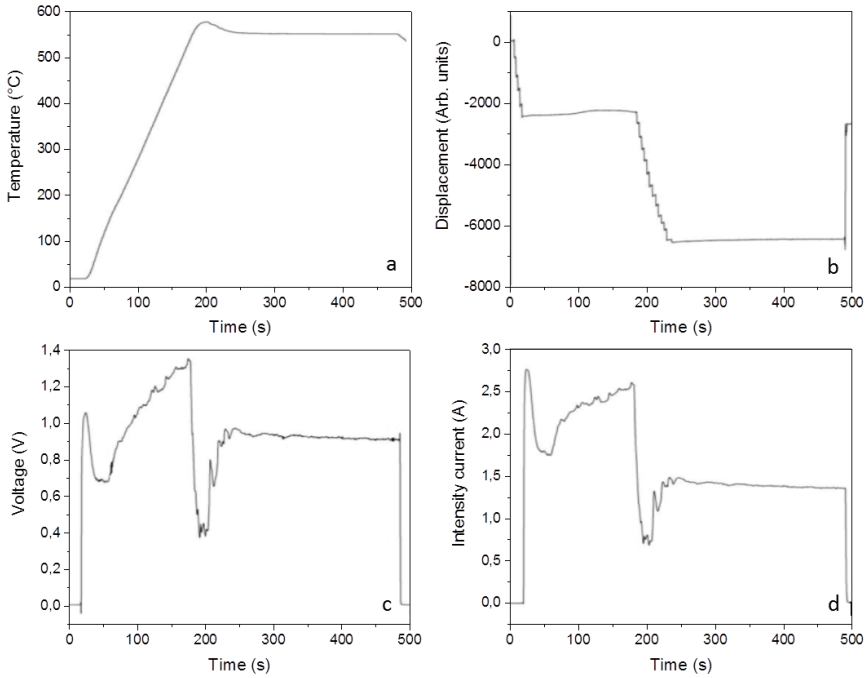

Figure 6.6 : HP-FAST control of temperature (**a**), vertical shift (**b**), current voltage (**c**) and current intensity (**d**).

HP-FAST processes were carried out using the instrument of Prof. Umberto Anselmi Tamburini, from the Dipartimento di Chimica Fisica of Università di Pavia.

6.5 Dilatometer

A dilatometer is a scientific instrument which allows the measurement of volume changes in response of physical or chemical phenomena. The thermal expansion (α) is defined as:

$$\alpha = \frac{1}{V}\left(\frac{dV}{dT}\right) \qquad 6.7$$

where V is the volume of the sample and T is the reached temperature.

Dilatometers are classified on the basis of the measuring technique used to evaluate the difference in the sample dimension:

- *Capacitance dilatometers:* the sample is in contact with a movable plate of a parallel capacitor and the other plate is stationary. When the sample length changes, the moveable plate moves and changes the gap between the plates. The registered capacitance is inversely proportional to the gap.

- *Connecting rod (push rod) dilatometer:* the examined sample is in the furnace and is in contact with a connecting rod which transfers the thermal expansion to a strain gauge, which measures the shift. Since the measuring system, i.e. the connecting rod, is exposed to the same heating treatment of the sample and expands itself, the obtained result must be correct for the expansion of the measuring rod.

- *Optical dilatometer*: is an instrument that allows dimension variations measurements of a specimen heated at temperatures that generally range from 25 to 1400 °C. The optical dilatometer allows the monitoring of materials' expansions and contractions by using an

optical group connected to a digital camera captures the images of the sample as function of the temperature. As the system allows to heat up the material and measures its longitudinal/vertical movements without any contact between instrument and specimen, it is possible to analyze the most ductile materials, such as polymers, as well as the most fragile, such as the incoherent ceramic powders for sintering process.

Considering the use related to material, dilatometers found a large use for the measure of thermal variation, i.e. expansion or shrinkage, when a certain material is exposed to a heating treatment. The heating treatment is often set using a controller that allows the choice final temperature and heating rate. The revelation system is usually a connecting rod method but should be often an optical one.

References

[1] “https://www.britannica.com/technology/transmission-electron-microscope.” .

[2] “https://www.britannica.com/technology/scanning-electron-microscope.” .

[3] B. D. Cullity and S. Stock, *Elements of X-ray diffraction*. Pearson Education, 2001.

[4] G. Will, *Powder diffraction: the Rietveld method and the two-stage method to determine and refine crystal structures from powder diffraction data.* Springer, 2006.

[5] “https://www.bruker.com/products/x-ray-diffraction-and-elemental-analysis/x-ray-diffraction/xrd-software/topas.html.” .

[6] “http://www.ing.unitn.it/ maud/.” .

[7] E. P. Bertin, *Principles and Practice of X-Ray Spectrometric Analysis*. 2012.

[8] “http://www.qdusa.com/.” .

[9] O. Guillon, J. Gonzalez-Julian, B. Dargatz, T. Kessel, G. Schierning, J. Räthel, and M. Herrmann, “Field-Assisted Sintering Technology/Spark Plasma Sintering: Mechanisms, Materials, and Technology Developments,” *Adv. Eng. Mater.*, vol. 16, no. 7, pp. 830–849, Jul. 2014.

Ringraziamenti

Vorrei ringraziare il Prof. Andrea Caneschi per avermi dato la possibilità di intraprendere questo percorso e avermi guidato in questi anni. Con riconoscenza ringrazio anche il Dott. Claudio Sangregorio per aver condiviso con me le sue conoscenze, per la sua costante disponibilità e per la sua infinita pazienza.

Ringrazio inoltre tutti i membri presenti e passati del Laboratorio di Magnetismo Molecolare, partendo dal gruppo "Nanoparticellari" (Claudia, Elvira, Pine, Giulio) fino ad arrivare al gruppo dei "Superficiali" (Matteo M., Irene, Giulia, Beppe), passando per i "Magnetisti Molecolari" (Roberta, Lorenzo S., Eva, Mauro, Matteo A., Pone, Lorenzo T.) che mi hanno supportato e sopportato in questi tre anni di lavoro, senza di loro questa esperienza non sarebbe stata così piacevole. Una menzione particolare va al Dott. Alberto López-Ortega, con cui ho mosso i primi passi lungo la strada del magnetismo e che mi ha guidato con allegria ma soprattutto tanta pazienza. Un grazie anche a Elisabetta, Martin e Andrea con i quali ho condiviso il laboratorio e una bellissima amicizia. Un altro grandissimo ringraziamento va a Samuele, Laura, Donella, Brunetto, Carlo e Marco per aver messo a mia disposizione le loro strumentazioni e competenze.

Ovviamente non posso non ringraziare tutti i membri del "Gruppo Pranzo Smen" per avermi portato a pranzo tutti i giorni e soprattutto per i tantissimi momenti di gioia che mi hanno regalato, con una menzione particolare alla "solita" Sara. Vorrei inoltre ringraziare gli amici fiorentini e quelli di "giù" per la loro vicinanza nei momenti più difficili.

Un ringraziamento speciale va alla mia famiglia, ai miei zii, i miei cugini che mi hanno sempre incoraggiato e supportato in questi anni e soprattutto a mia mamma, una donna davvero straordinaria.

Ringrazio infine la mia compagna di vita Celeste per avermi spronato a migliorare ogni giorno e per la sua costante presenza al mio fianco.